Air-coupled Capacitive Micromachined Ultrasonic Transducers based on Annular Cell Geometry

by

Shuai Na

A thesis
presented to the University of Waterloo
in fulfillment of the
thesis requirement for the degree of
Doctor of Philosophy
in
Systems Design Engineering (Nanotechnology)

Waterloo, Ontario, Canada, 2017

EXAMINING COMMITTEE MEMBERSHIP

The following served on the Examining Committee for this thesis. The decision of the Examining Committee is by majority vote.

External Examiner	Dr. Douglas Buchanan Professor of Electrical and Computer Engineering University of Manitoba
Supervisor	Dr. John T.W. Yeow Professor of Systems Design Engineering
Internal Member	Dr. Eihab Abdel-Rahman Professor of Systems Design Engineering
Internal Member	Dr. Daniel Stashuk Professor of Systems Design Engineering
Internal-external Member	Dr. Bo Cui Professor of Electrical and Computer Engineering

AUTHOR'S DECLARATION

This thesis consists of material all of which I authored or co-authored: see Statement of Contributions included in the thesis. This is a true copy of the thesis, including any required final revisions, as accepted by my examiners.

I understand that my thesis may be made electronically available to the public.

STATEMENT OF CONTRIBUTIONS

This thesis contains five co-authored articles where I was the primary author and responsible for all the modeling, design, fabrication, characterization, and analysis. The co-authors have provided insights and help with equipment training, experimental setup, reviewing, and editing. Below is the list of the articles.

1. <u>Concept and feasibility study of the annular-cell air-coupled CMUTs</u> [27].
   This piece of work is presented in Chapter 4 and published in a referred journal.
   S. Na, A. I.-H. Chen, L. L. P. Wong, Z. Li, M. Macecek, and J. T. W. Yeow, "Capacitive micromachined ultrasonic transducers based on annular cell geometry for air-coupled applications," Ultrasonics, vol. 71, pp. 152–160, Sep. 2016.
2. <u>Analytical modeling of annular air-coupled CMUT cells</u> [28].
   This piece of work is presented in Chapter 5 and published in a referred journal.
   S. Na, L. L. P. Wong, A. I. H. Chen, Z. Li, M. Macecek, and J. T. W. Yeow, "Lumped element modeling of air-coupled capacitive micromachined ultrasonic transducers with annular cell geometry," Ultrasonics, vol. 76, pp. 19–27, Apr. 2017.
3. <u>Optimization and comparison study of circular and annular air-coupled CMUT cells.</u>
   This piece of work is presented in Chapter 6 and under review of a referred journal.
   Na, S., Wong, L. L., Chen, A. I., Li, Z., & Yeow, J. T. (2017). An Optimization and Comparison Study of Air-coupled CMUTs with Circular and Annular Cell Geometries. IEEE Transactions on Ultrasonics, Ferroelectrics, and Frequency Control. (First revision submitted)
4. <u>Developing a single-element concentric annular-cell CMUT array</u> [29].
   Together with publication 5, this work is presented in Chapter 7 and published in a conference proceeding.
   Na, S., Wong, L. L., Chen, A. I., Li, Z., Macecek, M., & Yeow, J. T. (2016,

November). A CMUT Array based on Annular Cell Geometry for Air-coupled Applications. In Ultrasonics Symposium (IUS), 2016 IEEE International (pp. 1-4). IEEE.

5. <u>Developing a 9-element concentric annular-cell air-coupled CMUT array.</u>

   Together with publication 4, this piece of work is presented in Chapter 7 and under review of a referred journal.

   Na, S., Zheng, Z., Chen, A. I., Wong, L. L., Li, Z., & Yeow, J. T. (2017). Design and Fabrication of a High-power Air-coupled Capacitive Micromachined Ultrasonic Transducer Array with Concentric Annular Cells. IEEE Transaction on Electron Devices. (First revision submitted)

Abstract

Air-coupled ultrasound is gaining increasing industry momentum due to the demands and development of non-destructive evaluation (NDE) of aerospace composite materials. Currently, the micromachining technology has advanced such that vacuum cavities sealed by thin plates, known as Capacitive Micromachined Ultrasonic Transducers (CMUTs), can be fabricated through silicon micromachining processes in a low cost manner. Given the thin plates, a CMUT is able to vibrate with a low mechanical impedance and thus a high coupling efficiency with the ambient atmosphere. Nevertheless, air-coupled applications are still highly limited by the transmit power of air-coupled CMUTs. A circle is the routine geometry in most CMUT cell designs. Even though efforts have been put forward to address the limitations of circular design in terms of sensitivity, more investigation about other cell geometries is prudent.

In this work, a novel air-coupled CMUT design with annular cell geometry is proposed. Finite element analysis and experimental studies demonstrated its significant improvement in transmit efficiency over the conventional circular-cell CMUTs. A lumped element model was constructed to facilitate a better understanding and provide an efficient design technique of the annular CMUT. Three optimization schemes were developed to optimize the transmit efficiency and achieve a reasonable comparison between the novel annular and conventional circular CMUT cells. Based on the lumped models, a design optimization flow chart was constructed to facilitate the analytical optimization of the three schemes. To further enhance the transmit power as well as offer depth focusing, a 9-element concentric annular-cell array was designed, fabricated, and characterized. A pillar-free etching process was developed to create the deep large-area cavities. The cross-talk between neighbouring cells and the plate-cracking phenomenon were discussed with suggestions for improvement being provided.

This study provides a systematic framework for designing and studying annular-cell CMUTs and demonstrates their great potential in transmitting high-power ultrasound in air.

Acknowledgement

Foremost, I would like to thank my supervisor Prof. John T.W. Yeow, for offering me the opportunity to work in his Advanced Micro-/Nano- Devices Lab (AMNDL). As a supervisor, Prof. Yeow has not only guided me academically but also trained me to become an efficient time manger. During the past four years, I have spent countless hours in the cleanroom, bought hundreds of wafers, and attended several international conferences. The requests for material purchases, cleanroom user fees, and travel expense were always approved. It is a wonderful feeling to know that my project would always be supported. I also want to thank my committee members - Prof. Cui Bo, Prof. Eihab Abdel-Rahman, and Prof. Daniel Stashuk. Thank to Prof. Eihab Abdel-Rahman for allowing me to use the vibrometer in his lab, to prof. Daniel Stashuk for carefully correcting every single grammar error in my comprehensive report, and to Prof. Cui Bo for discussing with me about my research challenges. In addition, I sincerely thank Prof. Buchanan for agreeing to act as my external committee member and fly over 2000 km to physically attend my defense, given his busy schedule.

This work will not be possible without the financial supports from the CMC Microsystem, Dr. Mirek Macecek from Techno Scientific Inc., Waterloo Institute for Nanotechnology, and the University of Waterloo. I would also like to particularly thank the lab manager of Giga-to-Nanoelectronics Centre (G2N) - Richard Barber. Thanks for his unbelievable efforts in maintaining the lab equipment and making the lab an enjoyable place to work in. In addition, thanks to Edward for the equipment training in Toronto Nano Fabrication Centre and Nathan for the help in thermal oxidation in Quantum NanoFab.

My PhD experience was an enjoyable one because of all the lovely lab mates that I have met. Special thanks to Dr. Albert Chen who brought me into the world of CMUT, spent countless hours working in the cleanroom with me, and helped me edit each single article, to Dr. Zhenhao Li for being so enthusiastic whenever I asked for his assistant. It is you guys that make me feel at home. Thanks to the knowledgeable Dr. Lawrence Wong for always answering my dumb questions and being a great teacher. Thanks to Dr. Ruifeng Yang for being a good buddy who has always been more than happy to share his valuable cleanroom experience. To Zhou Zheng, Chen Chen, Champika and Yaning Cui, thanks for being great helpers whenever I requested. I sincerely apologize to the ones whose names are missed here.

To my parents, thanks for respecting the decisions I made and being so supportive in my study. Your daily encouragement over the phone keeps me optimistic. I cannot be luckier than being your son.

Lastly, and most specially, I would like to thank my beloved – Shuting. Thanks for sharing the most precious time in your life with me and being consistently patient, supportive, and understanding during the past four year. I would not make it this far without what you have given. Also, thanks to my girlfriend’s mother – Mrs. Liao, for taking care of me just like my mother. Thank you!

Table of Contents

List of Figures

List of Tables

Chapter 1 Introduction

1.1 Motivation

Ultrasound is commonly used in medical imaging [1], non-destructive evaluation (NDE) [2], and high intensity focused ultrasound (HIFU) therapy [3][4], which are all conducted in an immersion environment. In comparison, air-coupled ultrasound is less common, yet it holds important roles in vehicle borne radars [5], thickness measuring [6], and flow-meters [7]. Today, the increasing needs and requirements for human-computer interaction (HCI) [8] and air-coupled NDE [7][9] further promote the development of air-coupled ultrasonic transducers.

In general, designing an air-coupled ultrasonic transducer is difficult mainly due to the fact that the atmosphere has a low acoustic impedance, and the attenuation loss of ultrasound propagating in the atmosphere is significant. A large impedance mismatch between the transducer and the ambient atmosphere brings about a high reflection loss which is detrimental to the transducer's efficiency [10]. Also, the attenuation of acoustic waves in air is significant and increases drastically as the frequency goes up [11]. The attenuation limits the air-coupled transducers to operate at a low frequency (normally below 1 MHz) [12]. At a low frequency, a transducer with a limited aperture size usually has a small focal depth, which limits the working distance of the transducer. From the above, generating a high sound pressure level which can compensate the high acoustic attenuation and high reflection loss is essential for air-coupled transducers.

Conventional ultrasonic transducers are inherently resonant devices made from bulk piezoelectric materials. A backing layer is used to modify the transducer's bandwidth, and a front matching layer is required to improve the transducer-medium coupling efficiency [13]. However, the matching layer, which is desired to have a low density, low acoustic propagation speed, and low attenuation loss, is difficult to achieve. As a potential replacement technology of piezo-based transducers, micro-electromechanical systems (MEMS)-based ultrasonic transducers have been extensively studied. At the beginning, they were made from polymer films (with metal electrodes on the top) attached on back plates with cavities [14]. The capacitive force between the back plate and the film excited the film to compress and decompress the medium in order to generate ultrasound. Using micro-fabrication technology, transducers called capacitive micromachined ultrasonic transducers (CMUTs) can be made with thin plates covering tiny vacuum gaps, the depths of which can be precisely controlled [15]. Given the small gaps, CMUTs are able to have a very large electric field strength and thus an electromechanical coupling efficiency exceeding that of piezo-based transducers. On the other hand, since a thin plate has a very low mechanical impedance which matches well with the acoustic impedance of air, CMUTs can operate with a high coupling efficiency in air.

Although with a high coupling efficiency, CMUTs' transmit power is still limited. Different cell configurations have been studied to improve the transmit power, but most of them were focused on immersion CMUTs. For example, rectangular, square, and tent cells were compared to show that a tent cell had the highest transmit efficiency [18]. A piston-shaped plate was reported with a superior transmit efficiency than a conventional circular one [19]. For air-coupled CMUTs, efforts have been primarily concentrated on the circular cell geometry. A CMUT with multiple moving circular plates demonstrated an improved transmit sensitivity due to the decreased effective cavity depth [20], and DC-free actuation methods were used to swing a circular plate in the entire cavity depth for a maximized output power [21][22]. In most cases, improving the transmit power involves high-amplitude input voltages, which set a high requirement on the breakdown voltage of the insulating layer [23]. On the other hand, due to the unavoidable space between circular cells, the fill factor of a circular-cell CMUT array is another limitation factor for a high transmit power.

The motivation behind this work is to improve the transmit efficiency of current CMUT designs by defining a novel cell configuration. Such cell configuration should possess an improved surface output power density. When it is made into an array, the array should promise a high fill factor as well as allow acoustic focusing along the depth direction. The ultimate goal of this study is demonstrating the feasibility of using the proposed CMUTs for generating high-power air-coupled ultrasound and constructing a systematic framework for the design, fabrication, and optimization of such devices.

1.2 Contribution

The major contribution of this work is developing an air-coupled CMUT that can provide a significantly improved transmit efficiency over the conventional circular cell design.

The second contribution is providing a systematic framework for analyzing and designing the proposed CMUTs. This framework consists of an analytical model and a set of analytical optimization schemes, which not only can be used to guide the design of the proposed CMUT for different applications but also provide a methodology for the design of CMUT with arbitrary cell configurations.

The third contribution of this project involves developing a novel process of fabricating the proposed CMUT arrays. It provides a solution to overcoming the formation of silicon pillars during etching deep large-area cavities. Additionally, the method of creating deep narrow trenches with inductively coupled plasma (ICP) etching can be referred by the fabrication of similar structures.

1.3 Thesis Organization

This thesis is organized as follow:

In Chapter 2, the background of ultrasound, basics of piezoelectric ultrasonic transducers, transducer arrays, CMUT fundamentals including operation principles and fabrication methods, and a review of CMUTs for air-coupled applications are presented.

In Chapter 3, the analytical modeling of a conventional circular CMUT cell is presented. The introduced models include a mass-spring-damper model and an equivalent circuit model.

In Chapter 4, the concept of an annular CMUT cell is introduced. The fabrication processes, FEA, and experimental results are presented to illustrate the feasibility of the design.

In Chapter 5, an analytical model of the annular CMUT cell is built in attempt to promote a better understanding and accelerate the design procedure of an annular-cell CMUT. The model was derived from the plate theory and verified with both simulation and experimental methods.

Based on the works in Chapters 3 and 5, Chapter 6 is dedicated to optimizing the design of both conventional circular CMUT cells and annular CMUT cells. An analytical comparison study between the two types of cells is conducted to illustrate the advantages of the annular one.

In Chapter 7, a concentric annular-cell CMUT array was designed, fabricated, and characterized. The fabrications challenges associated with the large device areas and virtual connections in the deep trenches are discussed. The cross-talking and plate cracking phenomenon associated with the fabricated devices are investigated.

A summary of the thesis is included in Chapter 8.

Chapter 2 Background of Ultrasound

2.1 Ultrasound Basics

Ultrasound is typically defined as mechanical waves propagating within a matter medium at frequencies beyond the human audible band, which is approximately 20 kHz. As a type of wave, ultrasound obeys the common wave propagation relation of

$$\lambda = f \cdot c, \tag{2.1}$$

where λ, f, and c are the wavelength, frequency, and speed of sound in the medium. The basis of ultrasound imaging lie in the pulse-echo principle such that the transmitted acoustic signals are detected once they are reflected or backscattered from an interface between two structures or media with inhomogeneous acoustic impedance. Taking the simplest imaging approach, A-scan (Fig. 2.1.1), for example, an echo signal is detected after the transmitted pulse being reflected back or backscattered. Since the speed of sound in a medium is known, the reflector or scatterer can be located by multiplying the time of flight with the speed of sound and a factor of 0.5 as the signal has to travel from the transmitter to the scatterer and then back again: twice the separation distance.

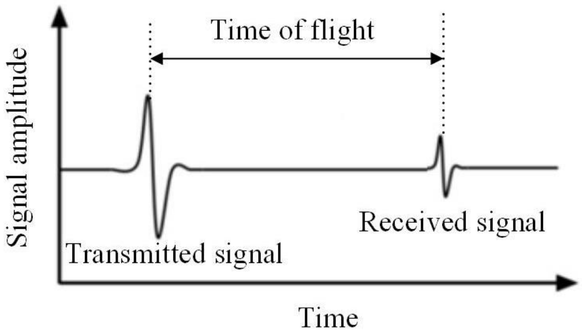

Figure. 2.1.1 A pulse-echo event in the time domain.

The amplitude of the received signal is dependent on three factors, which are the sensor sensitivity, acoustic coupling or acoustic contrast of the two materials at the interface, and the acoustic attenuation in the medium. Figure. 2.1.2 illustrates the acoustic propagation at the interface of two different materials with impedance Z_1 and Z_2, respectively.

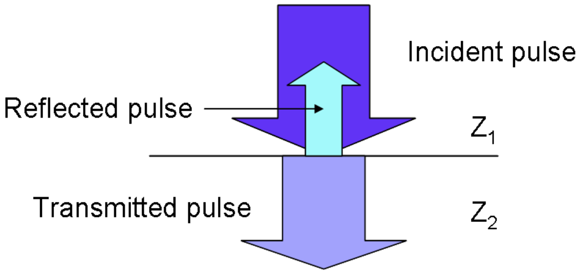

Figure. 2.1.2 Acoustic propagation at the interface of two media.

A parameter governing the amount of sound reflected or transmitted at the interface is the Reflection Coefficient [1]

$$RF = \frac{Z_2 - Z_1}{Z_2 + Z_1}. \tag{2.1.2}$$

Similarly, the Transmission Factor gives the ratio of the amplitude of the transmitted pressure to that of the incident pressure [1]

$$TF = 1 + RF = \frac{2Z_2}{Z_2 + Z_1}. \tag{2.1.3}$$

It should be noted that Eqs (2.1.2) and (2.1.3) assume the acoustic wave as a plane wave. From Eqs (2.1.2) and (2.1.3), if the acoustic impedance of the two materials is the same, *RF* will be equal to 0, which means the waves propagate in the same medium without reflection. In the case of wave propagating into a buffer $(Z_1 \gg Z_2,\ RF = -1,\ TF = 0)$, the acoustic energy will be completely absorbed by the buffer, and the pressure at the interface is equal to zero. When the wave hits a hard boundary $(Z_1 \ll Z_2,\ RF = 1,\ TF = 2)$, all the energy will be reflected back, and the pressure at the interface is double the pressure of the incident wave.

The loss of the waves propagating in a medium is called “attenuation” and can be described by an exponential law with distance. Defining *z* as the propagation distance and *P* as the amplitude of the wave pressure, we can describe the attenuation as [1]

$$P(z, f) = P(0, f)e^{-\alpha(f)z}, \tag{2.1.4}$$

where $\alpha(f)$ is the attenuation loss in Np/m. Np and dB can be converted to each other based on

$$1\ \mathrm{NP}=\ln\left(\frac{x_2}{x_1}\right)=\frac{\log_{10}\left(\frac{x_2}{x_1}\right)}{\log_{10}(\mathrm{e})}=\frac{1}{20\log_{10}(\mathrm{e})}\cdot 20\log_{10}\left(\frac{x_2}{x_1}\right)=0.115\times 1\ \mathrm{dB}, \tag{2.1.5}$$
$$1\ \mathrm{dB}=8.69\ \mathrm{Np}.$$

According to measurement results in [11], the attenuation losses of air and water at 20 °C and 20% humidity are plotted in Fig. 2.1.3.

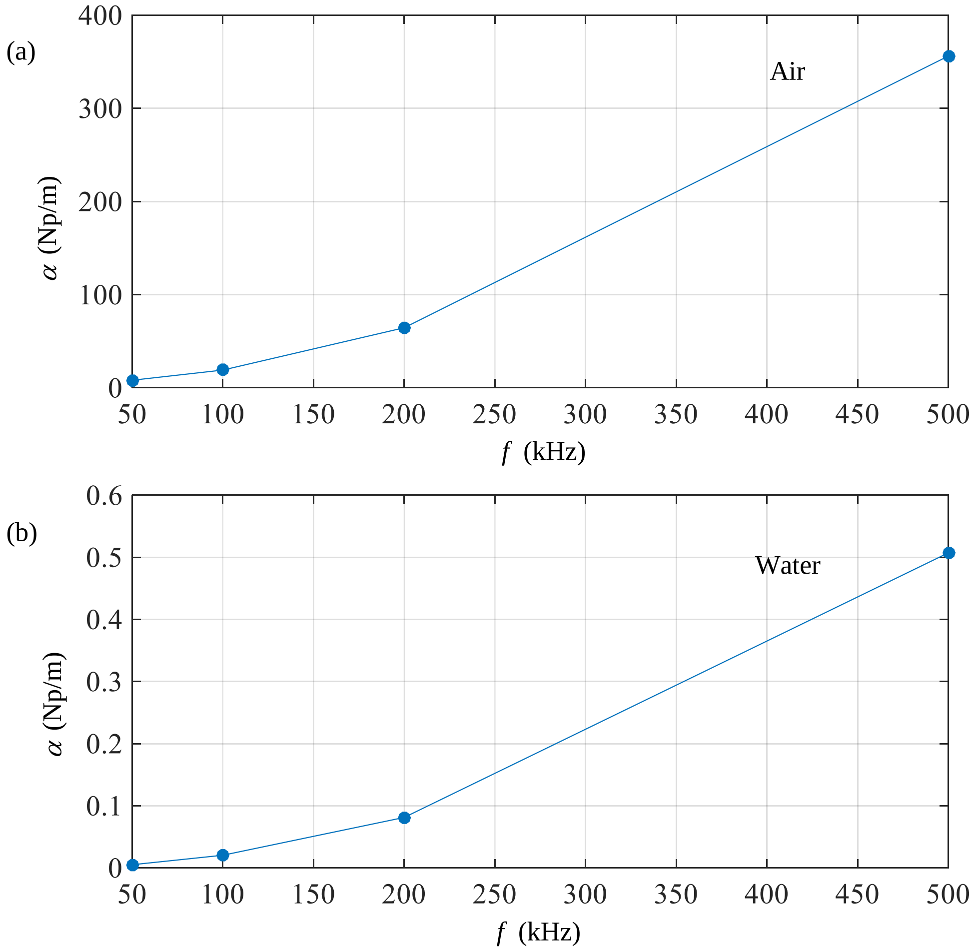

Figure. 2.1.3 Attenuation losses of air (a) and water (b) at 20 °C and 20% humidity at frequencies between 50 and 500 kHz.

Correspondingly, the normalized acoustic pressure of a plane wave at a distance of 1 m is plotted in Fig. 2.1.4. It shows that the acoustic pressure decreases much more dramatically with the increase of frequency in air than it does in water. As a result, air-coupled transducers are normally designed with a low operating frequency (several hundred kHz) in attempt to increase the power-delivery efficiency [30].

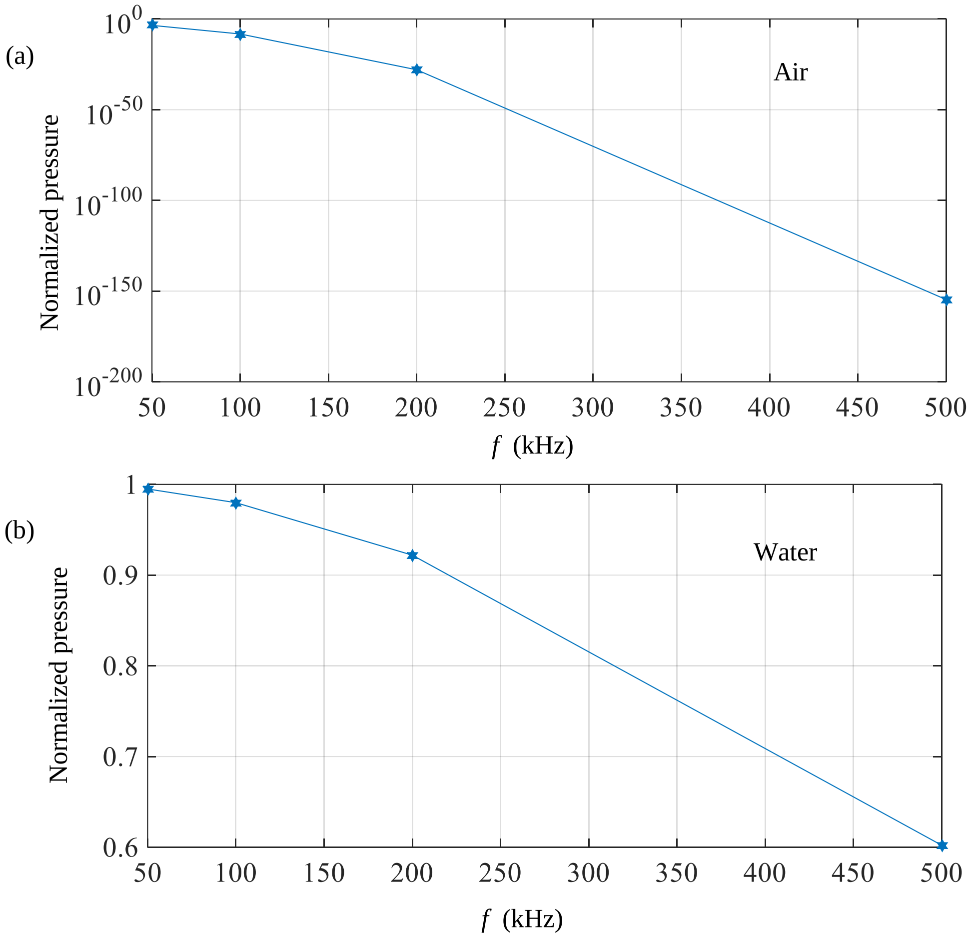

Figure. 2.1.4 Normalized pressure of a plane wave at a distance of 1 m in air (a) and water (b) at 20 °C and 20% humidity at frequencies between 50 and 500 kHz.

Even though the assumption of plane wave was made in the above discussion, the real acoustic field at a transducer is more complicated and has a Sinc function profile due to the interference effect. Figure. 2.1.5 shows the acoustic field profile (isobars) of a circular aperture from a large-scale point of view.

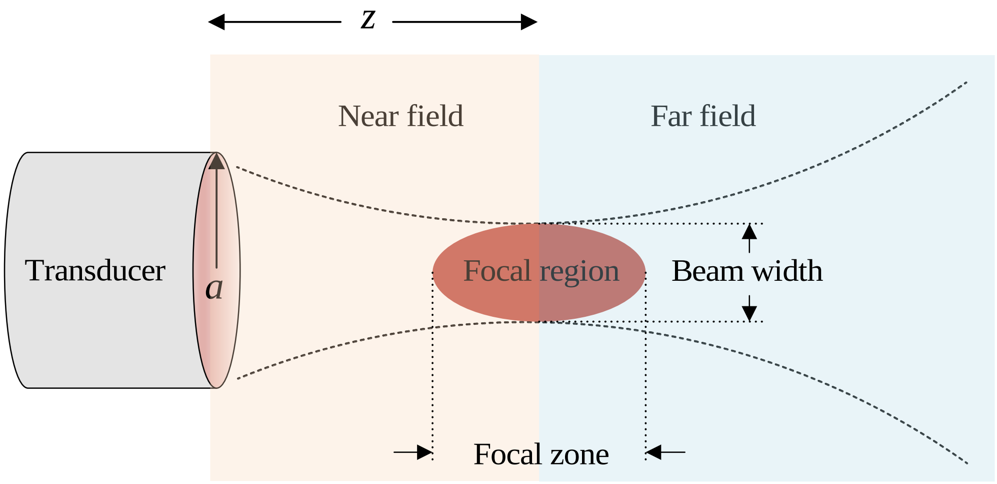

Figure. 2.1.5 Acoustic field of a circular transducer aperture.

The natural focal distance *z* determines the depth of imaging and is a function of the frequency, speed of sound in the medium, and the aperture radius as [1]

$$z = \frac{a^2 f}{c}. \tag{2.1.5}$$

Therefore, a higher frequency and a larger aperture size will help increase the focal depth. This relationship is especially important for air-coupled transducers because a tread off is required between a high frequency (results in a far focal distance) and a low acoustic attenuation (leads to a focal distance closer to the transmitter). The near field is defined as the area between the transducer and the focal spot, whereas the far field is the area beyond the focal distance. Figure. 2.1.5 shows that the acoustic field profile narrows at the focal area. Since a narrow beam width can distinguish finer features, the beam width of a transducer is a critical imaging consideration. The beam width is typically defined as the width of the profile of the -3-dB maximum pressure at the focus. Similarly, the focal zone is defined as the length of the profile of the -3-dB maximum pressure at the focus.

2.2 Piezoelectric Transducers

Conventional ultrasonic transducers make use of the piezoelectric effect, where mechanical force and electric energy can be converted to each other in the piezoelectric materials. Therefore, they can be used as either an actuator or a sensor or both. The most widely used piezoelectric transducers are made of lead zirconate titanate (PZT) since it can offer a high electro-mechanical conversion efficiency. However, only a piece of PZT is not suitable for realistic applications because this it has an acoustic impedance (approximate 30 Mrayl) significantly larger than that of air (approximate 4×10^{-4} Mrayl) [31]. As indicated in Eq (2.1.3), the large impedance mismatch will lead to an extremely low transmit efficiency. As a result, the PZT crystals are usually diced and packaged to form a transducer probe which includes more functional layers to improve the acoustic performance. A structural overview of a standard ultrasound probe is illustrated in Fig. 2.2.1.

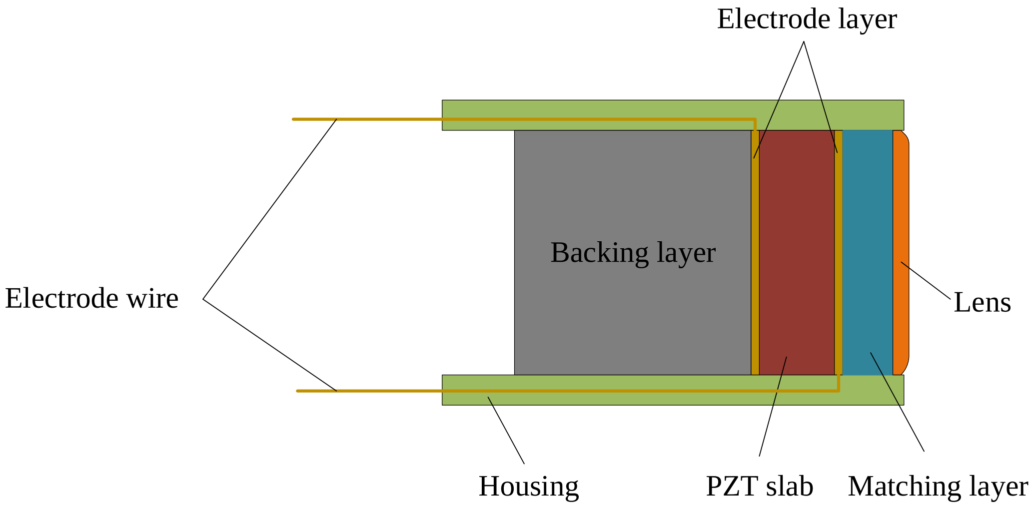

Figure. 2.2.1 Structure of a standard PZT transducer probe.

The probe is comprised of a PZT layer, a matching layer, a backing layer, and an acoustic lens in front of the matching layer. The matching layer functions as a coupling agent between the PZT slab and the acoustic lens material which normally has a good coupling with the ambient environment. Ideally, a matching layer and an acoustic lens are required to have low densities, low acoustic propagation speeds, and low attenuation losses. Yet, such materials are difficult to realize [31]. The backing layer is used to absorb the mechanical energy of the PZT slab to suspense the residual vibration. Normally, it has a similar impedance with that of the PZT material such that the energy can be transferred into it. The backing layer is normally required for immersion applications, such as medical imaging, because without this layer, the impulse response of the PZT will be several-period long and the axial resolution will decrease. However, for air-coupled applications, which require the transducer to generate a high power, the back layer will not be present as it will dissipate a great portion of the acoustic power from the PZT slab. Recently, the trends of piezoelectric-based transducer research have been dedicated on piezo ceramics which can offer a lower acoustic impedance, a higher damping (wider bandwidth), and an improved electro-mechanical coupling efficiency [32][33].

2.3 Transducer Arrays

Ultrasonic transducers can be classified into two types, which are single-element transducer and transducer array. A single-element transducer can be adopted for A-scan, which is to detect echo sources along the center line of the transducer. It can also be amounted onto a mechanical scanning station to conduct 1-D and 2-D scans to correspondingly achieve a 2-D and 3-D image. In comparison, an array transducer is made of a number of elements, which can be individually controlled. The most commonly used arrays include linear arrays, curvilinear arrays, phased arrays, radial arrays, annular arrays, and 2-D arrays (Fig. 2.3.1).

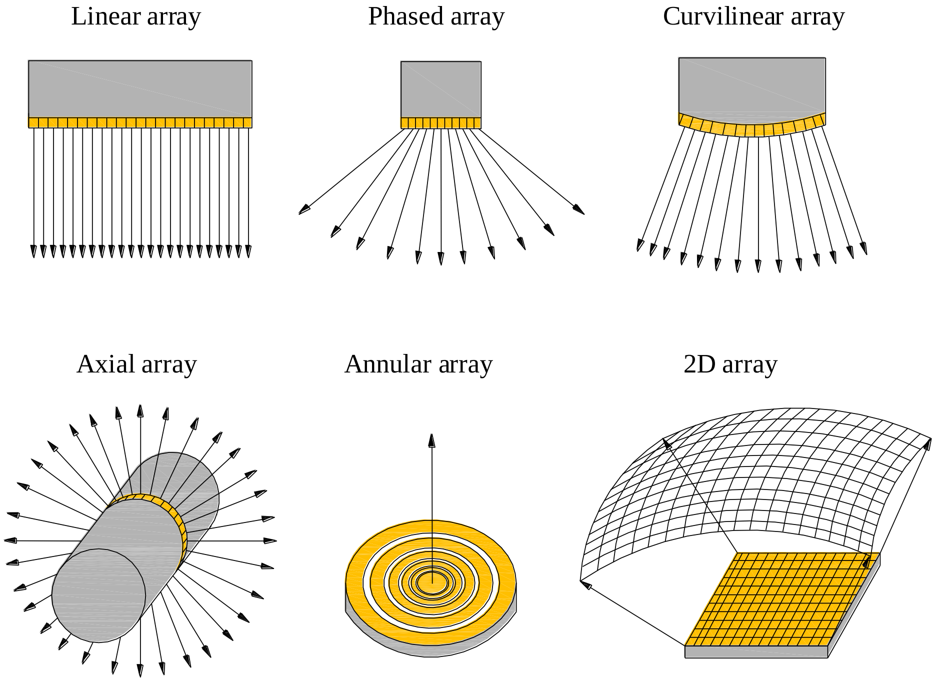
Linear array
Phased array
Curvilinear array
Axial array
Annular array
2D array

Figure. 2.3.1 Types of ultrasonic transducer arrays.

Linear arrays, phased arrays, and curvilinear arrays are all 1-D arrays which are used to conduct 1-D scan and generate a 2-D image. A linear array is normally long in size and has a constant width of field of view used for imaging organs near the skin. In comparison, a phased array and a curvilinear array have a fan-shaped field of view, which allows the acoustic wave to go through the gaps between ribs for cardiovascular imaging. The radial arrays are normally used for catheter-based endovascular imaging. An annular array is different from a single-element transducer by being able to focus along the depth direction. The capability of focusing along the depth direction allows an annular array to generate an improved acoustic power at the focal area as well as provide a large field of view in the depth direction. A 2-D array can come into different forms including a sparse array, fully-addressed 2-D array, and a row-column array. It can be used for conducting electrical 2-D scans to achieve 3-D images.

For air-coupled surface scanning applications, a 1-D or 2-D array can be adopted. However, for more common applications, such as air-coupled NDT of thin plates, the single-element transducers, which have fixed natural focal depths, are most commonly used. This is due to fact that the through-transmission mode (Fig. 2.3.2 (a)) [34] and the guided wave method (Fig. 2.3.2 (b)) [35], which only require one high-intensity acoustic beam, are the most effective methods to detect discontinues in a plate structure.

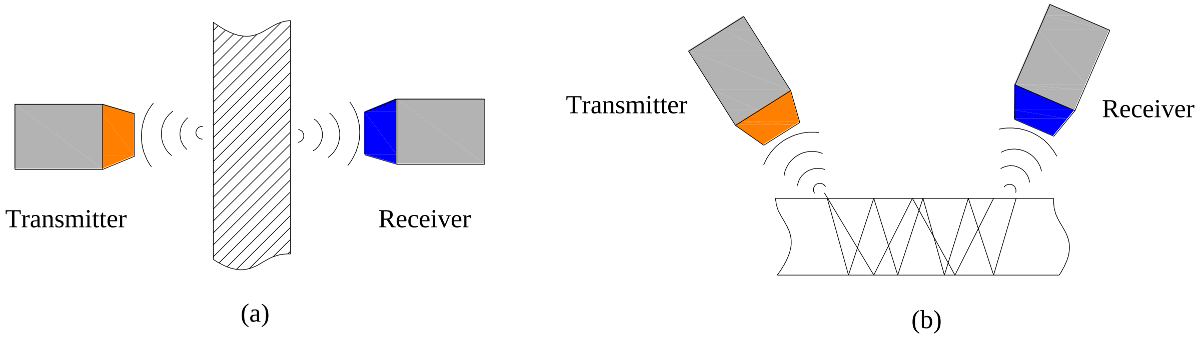

Figure. 2.3.2 Methods of air-coupled NDT of thin plates.

To improve the acoustic power output as well as increasing the lateral resolution, a single-element air-coupled transducer is normally manufactured with a curved aperture or a flat aperture with an acoustic lens or reflector in front of the acoustic source to enhance focusing. Figure. 2.3.3 governs three typical focused air-coupled ultrasonic transducers. For all these transducers, the backing space is filled with air instead of a damping material to maximize the Q factor of the piezo disk so as to improve the output power.

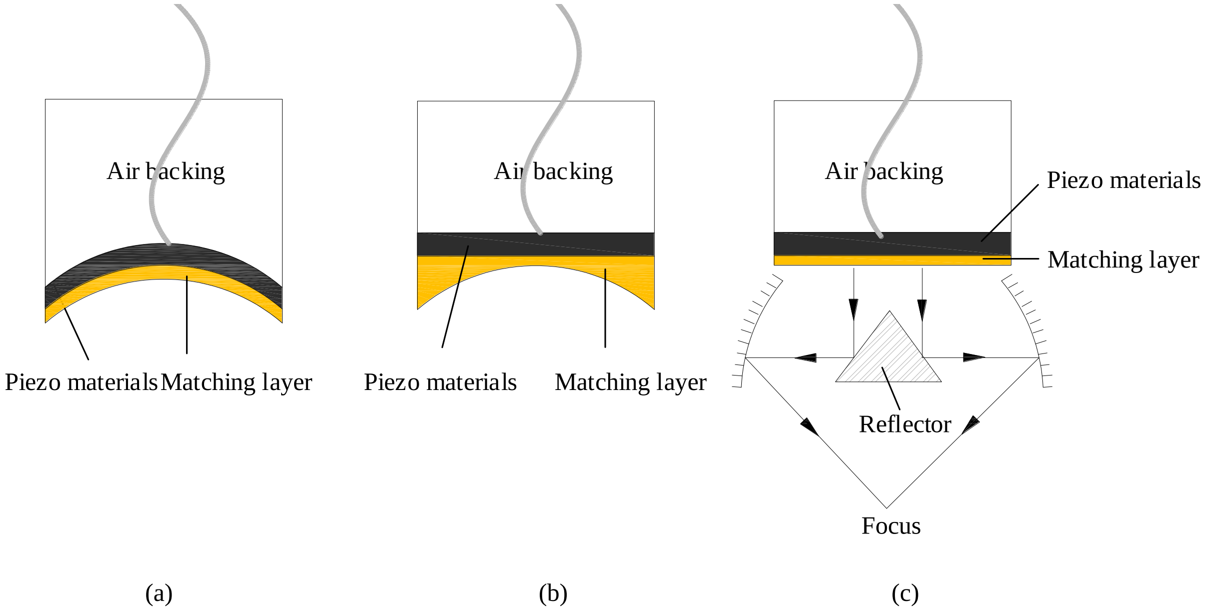

Figure. 2.3.3 Focused single-element transducers: (a) Spherically shaped piezo disk; (b) flat piezo disk with acoustic lens; (c) flat piezo disk with reflector.

2.4 Capacitive Micromachined Ultrasonic Transducers

Capacitive micromachined ultrasonic transducers (CMUTs) are a new generation of ultrasonic transducers fabricated with the micromachining technologies shared with the integrated circuit (IC) industry. CMUTs were invented by Dr. Khuri-Yakub's research group at Stanford University about fifteen years ago [36]. Since then they have been considered as the most promising replacement technology of present piezoelectric ultrasonic transducers.

2.4.1 Fundamental of Operation

Figure. 2.4.1 illustrates the schematic of a fundamental CMUT element - a CMUT cell. It is made of a thin plate suspending over a vacuum cavity. In transmit mode, an AC excitation voltage and a DC bias are simultaneously applied on the top and bottom electrodes. Due to the induced capacitive force between the electrodes, the plate will vibrate and generate acoustic waves at its surface. In the receive mode, the plate will be disturbed by an incident wave. The induced vibration leads to a capacitance change, which can be detected and measured by a front-end circuit.

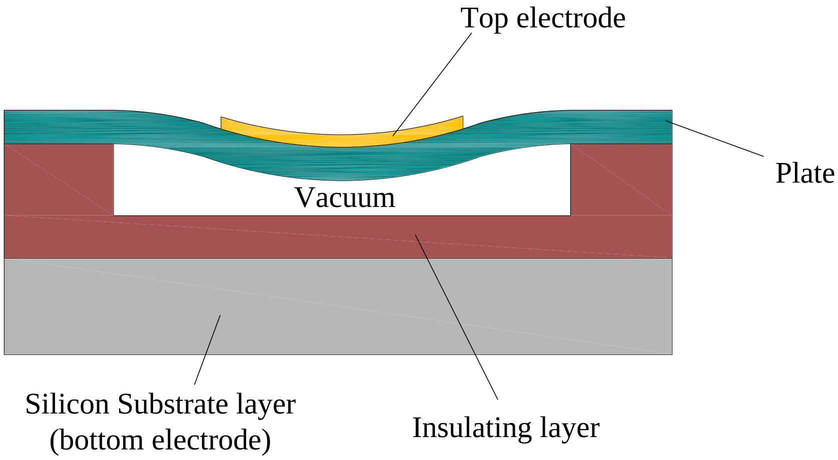

Figure. 2.4.1 The structure of a typical CMUT cell.

The most common CMUT plates are made of single-crystal silicon with a thickness ranging from hundreds of nanometers to dozens of micrometers depending on the design frequency. This is especially true for air-coupled CMUTs because they are normally designed with a low frequency which requires a large cell diameter and a thick (dozens of micrometers) plate. However, for the high-frequency CMUTs used for medical imaging, low pressure chemical vapor deposition (LPCVD) silicon nitride are a better material option since its thickness can be precisely controlled by the deposition conditions and time, and its Young's modulus is higher than that of single crystal silicon [37][38]. Given a higher Young's modulus, the CMUT plate can be made with a smaller thickness which enables a higher sensitivity. Another benefit of using silicon nitride as the plate material is that LPCVD silicon nitride has a good insulating property and therefore can help improve the breakdown voltage [39].

2.4.2 Fabrication Methods

Two typical fabrication processes for CMUTs are the surface micromachining process and fusion bonding process. They are distinguished by the ways how the plates are constructed. Surface micromachining is the first method used for CMUT fabrication [16][36][40][41][42][43][44][45]. In a typical surface micromachining process (Fig. 2.4.2), the plate is deposited on a sacrificial layer which is subsequently removed to create the suspended plate configuration. An additional plasma enhanced chemical vapor deposition (PECVD) step is used to seal the releasing holes in order to achieve a vacuum-sealed cavity.

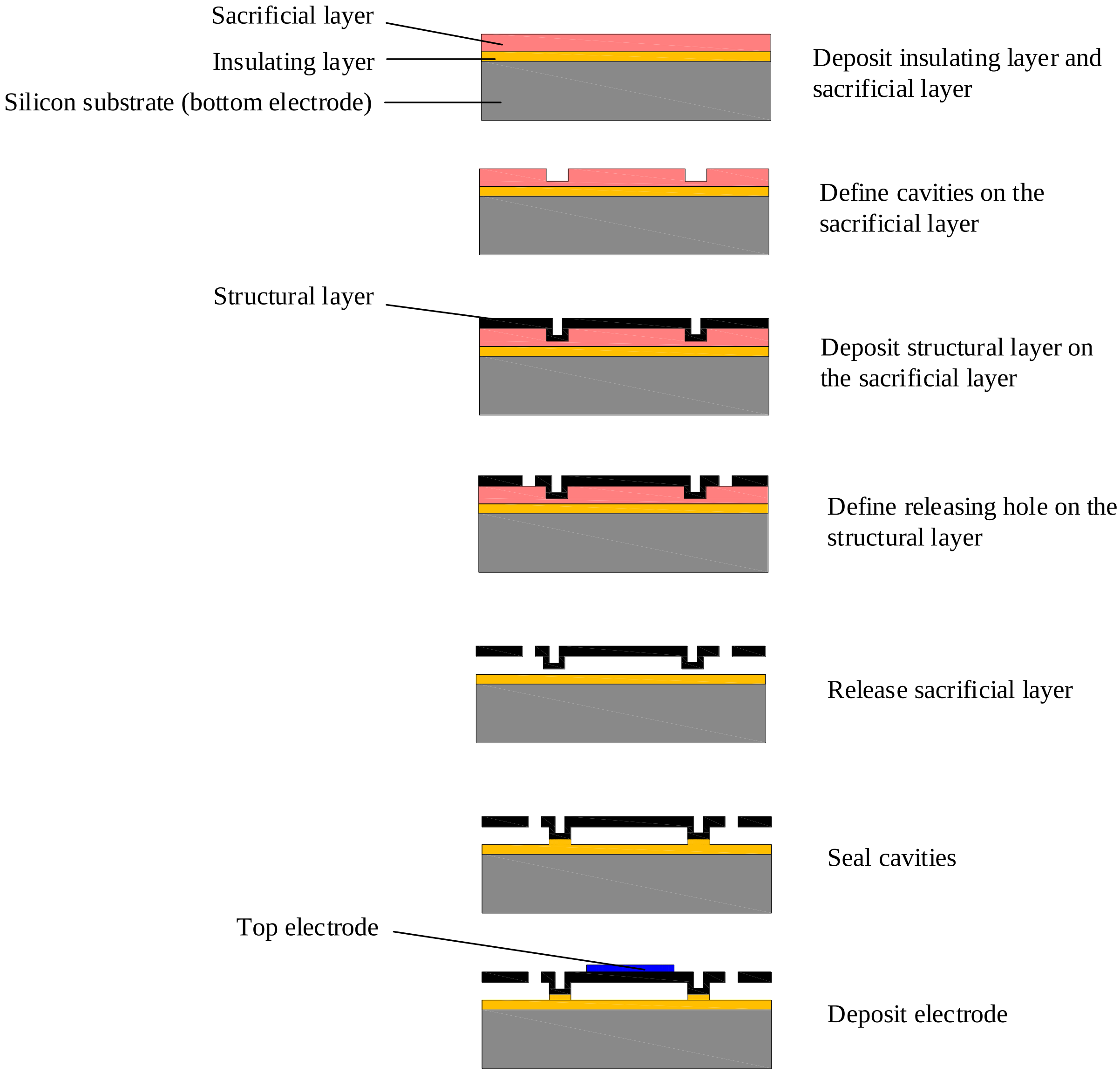

Figure. 2.4.2 Surface micromachining process for CMUT fabrication.

Compared with surface micromachining, the fusion bonding process, which was first reported by Huang et al in 2003 [46], is more straightforward. As shown in Fig. 2.4.3, the process begins with a highly doped silicon wafer which serves as the common bottom electrode and an SOI wafer of which the device layer is used as the plate. Cavities are etched into the insulating layer, which was deposited or grown from the silicon substrate. The two wafers are directly bonded and annealed to achieve a permanent covalent bond. The bonded pair is subsequently put into silicon etchant to remove the handling silicon of the top wafer. The buried oxide (BOX) layer of the SOI wafer is subsequently removed by buffered oxide etchant (BOE) to expose the suspending device layer as the plate.

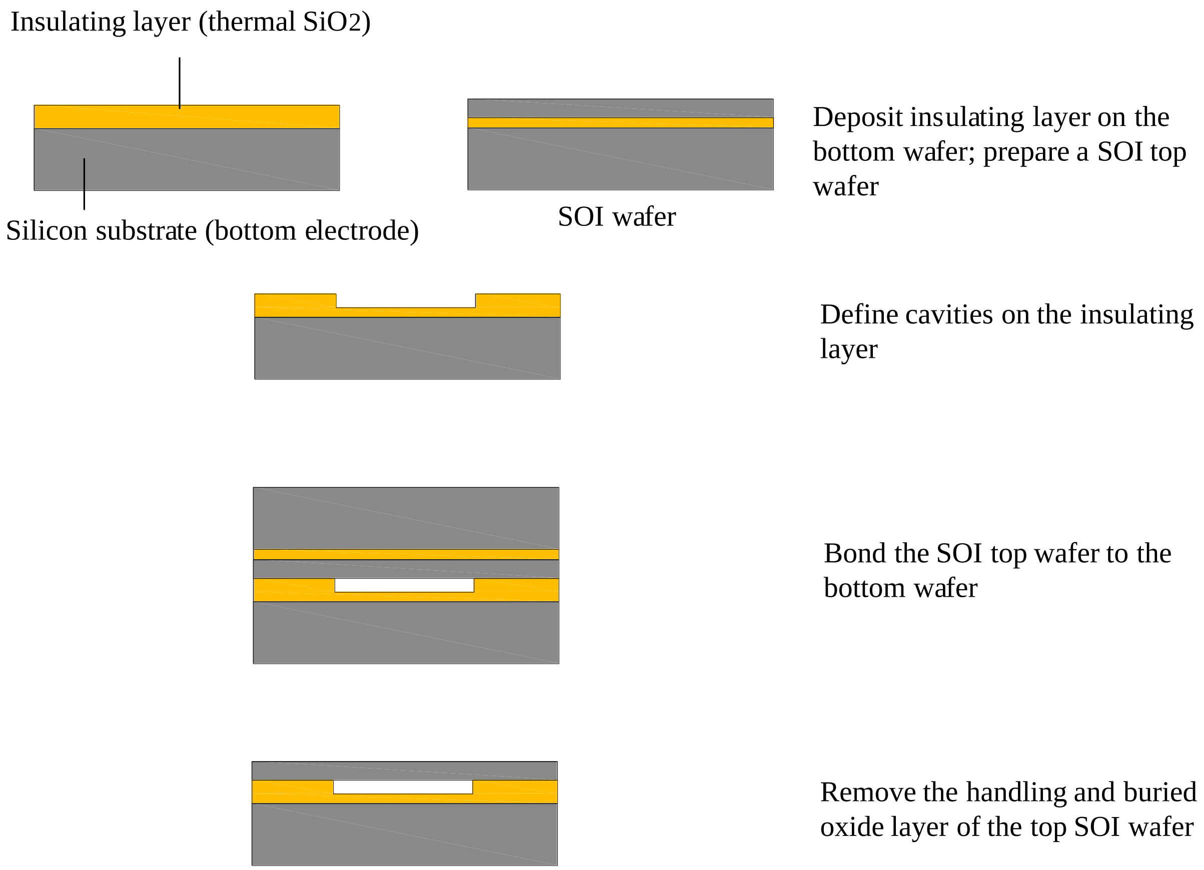

Figure. 2.4.3 Fusion bonding process for CMUT fabrication.

Figure. 2.4.3 only illustrates a typical wafer bonding process based on the SOI wafer as the top wafer. Investigations have also be conducted on the adhesive bonding process [47][48][49][50], anodic bonding process [51], LPCVD silicon nitride to LPCVD silicon nitride bonding process [38][52][53][54], and LPCVD silicon nitride to thermal silicon dioxide bonding process [55]. For either surface micromachining or wafer bonding processes, if an insulating material is used as the plate, a top electrode must be deposited on the plate. Alternatively, if the plate is made of conductive silicon, a top electrode may not be required because the plate itself can serve as the top electrode.

Comparing the micro-machining and wafer bonding processes, we can find that the fusion bonding process has a number of advantages over the surface micromachining one. The primary advantage is that the fusion bonding process is much simpler by only requiring one photomask for cavity patterning. Also, the plate thickness can be well controlled as the plate is transferred from a commercial SOI wafer. Moreover, without the need for releasing the sacrificial layer in the cavities, CMUT cells can be packed closer together, and a higher fill factor can be achieved. A significant problem associated with the sacrificial process is the stiction problem that the surface tension of the liquid etchant in the cavity brings the plate to the bottom and holds them together [56][57]. Since the wafer bonding step does not involve any liquid, the stiction problem can be avoided. Another benefit of using the wafer bonding process is that it allows the easy fabrication of arbitrary cavity shapes. Last but not least, by using the wafer bonding process, a very good cavity vacuum can be obtained since the wafer bonding can be conducted in a vacuum chamber.

2.5 CMUTs for Air-coupled Applications

The invention of CMUT originated from the researchers in Stanford University attempting to use air-coupled ultrasound to detect cracks in the wings of a fighter jet [58]. In 1997, the same group demonstrated transmitting air-coupled acoustic wave through a piece of aluminum which has a thickness of multiple of the half wavelength to allow the generation of standing waves inside the plate [59]. Soon after, it was found that the immersion performance of a CMUT was exceptionally high as fractional bandwidth of over 100% was reported. As a result, the focus of CMUT was shifted from air-coupled applications to immersion applications. However, there are still a number of papers on air-coupled CMUTs in the literature. For example, the radiated fields of air-coupled CMUTs were modeled, and CMUTs were used to scan the surface of a coin using a mechanical stage [60]. In 2008, General Electric reported a CMUT-based air-coupled transducer for NDT [61]. Here, the reported CMUTs demonstrated a higher transmit efficiency than the commercial piezoelectric transducers. More recently, researchers have investigated air-coupled CMUTs for chemical gases [62][63][64] and pressure sensing in harsh environments [65][66].These CMUTs operate at frequencies ranging from 100 kHz to 400 kHz depending on the air pressure. A CMUT array designed for vehicle collision avoidance applications was also reported in [67]. More recently, with the development of Human-Computer Interaction (HCI), ultrasound has also been demonstrated to be suitable for the applications such as pen tracking systems, in-door positioning systems, and range monitoring in air [8]. These potential air-coupled applications warrant the further development of air-coupled CMUTs.

Chapter 3 Modeling of a Circular CMUT Cell

3.1 Mass-spring-damper Model

The cross section of a typical circular CMUT cell is illustrated in Fig. 3.1.1 (a). The basic concept of analyzing a CMUT cell is to simplify it as a mass-spring-damper model as shown in Fig. 3.1.1 (b).

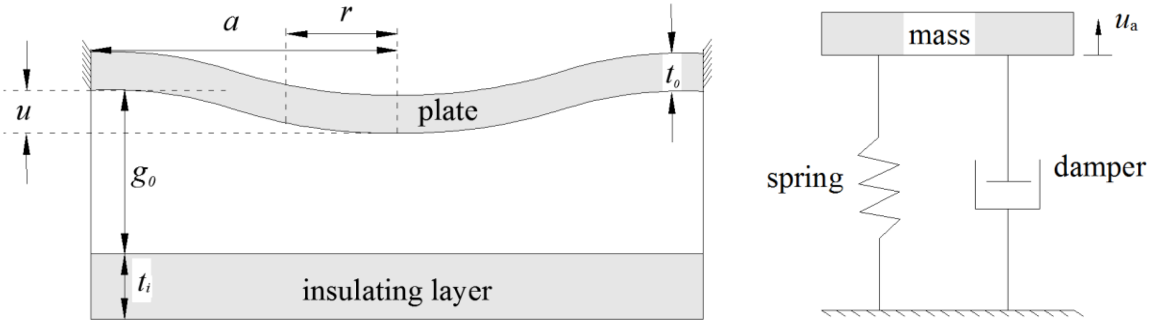

(a) (b)

Figure. 3.1.1 (a) Cross-sectional schematic of a circular CMUT cell. (b) Equivalent mass-spring-damper model.

The radial position, plate thickness, insulating layer thickness, cavity depth, cell radius are denoted by r, t_0, t_i, g_0, and a, respectively. The effective cavity depth g is calculated based on g_0, the relative permittivity of the insulating layer ε_i, and t_i based on the series capacitance theory as

$$g = g_0 + \frac{t_i}{\varepsilon_i}. \tag{3.1.1}$$

The circular plate is subject to a pressure $P = P_{atm} + P_e$, where P_{atm} and P_e represent the atmospheric pressure and electrostatic pressure, respectively. At static state ($P = P_{atm}, P_e = 0$), the plate displacement be expressed as [68]

$$u(r) = \frac{Pa^4}{64D}(1 - \frac{r^2}{a^2})^2, \tag{3.1.2}$$

where D is the flexural rigidity and equal to

$$D = \frac{Et_0{}^3}{12(1-\upsilon^2)}. \tag{3.1.3}$$

In Eq (3.1.3), E and υ are the Young's modulus and Poison's ratio of the plate material. Due to the symmetry of the clamped circular plate, the peak static displacement locates at the center and equals

$$u_p = \frac{Pa^4}{64D}. \tag{3.1.4}$$

For the equivalent mass-spring-damper model, the average plate displacement is widely used as the spatial variable, which can be derived by integrating Eq (3.1.2) over the entire plate area (A) to be

$$u_a = \frac{1}{A}\int_0^a 2\pi r u(r) dr = \frac{1}{3} u_p. \tag{3.1.5}$$

In the same way, the root mean square (RMS) displacement can be derived to be

$$u_{rms} = \sqrt{\frac{1}{A}\int_0^a 2\pi r u^2(r) dr} = \frac{1}{\sqrt{5}} u_p = \frac{3\sqrt{5}}{5} u_a. \tag{3.1.6}$$

In the case of small displacement (deflection obeys Hooke's law), the equivalent spring constant k_1 can be derived by dividing the force acting on the plate by u_a as

$$k_1 = \frac{AP}{u_a} = \frac{192\pi D}{a^2}. \tag{3.1.7}$$

According to the plate theory [69], the natural resonance frequency of a clamped circular plate can be expressed as

$$\omega_0 = \frac{10.22}{a^2}\sqrt{\frac{D}{\rho t_0}}, \tag{3.1.8}$$

where ρ represents the density of the plate material. As the natural resonance frequency of a mass-spring-damper system can also be expressed as

$$\omega_0 = \sqrt{k_1 / m}, \tag{3.1.9}$$

where *m* is the lumped mass, *m* can be developed to be

$$m = \frac{k_1}{\omega_0^2} = 1.84 m_0, \tag{3.1.10}$$

where m_0 is the actual mass of the plate.

When a resonator, such as a CMUT plate, works in the flexural mode, it will compress and decompress the medium. The effect of the medium on the vibrating resonator is called acoustic impedance and defined as

$$Z_{acoustic} = \frac{P}{v}, \tag{3.1.11}$$

where P and v are the surface pressure and particle velocity, respectively. For a single CMUT cell in an infinite, plane, rigid baffle, its plate is acoustically loaded by the pressure generated by itself, and thus the acoustic impedance is called "self-acoustic impedance" and denoted by Z_{11}. For a resonating CMUT cell surrounded by other active cells, its plate is not only subjected to the self-acoustic impedance but also acoustically loaded by the pressure generated by the other cells. The impedance resulting from the other cells is called "mutual-acoustic impedance". The mutual-acoustic effect is important when studying a CMUT cell in immersion, such as water, which has a large acoustic impedance, but it is insignificant in air because the air acoustic impedance is five orders of magnitude lower than that of water. Therefore, the mutual impedance is ignored throughout this thesis, and the acoustic impedance $Z_{acoustic}$ is simplified as the self-acoustic impedance ($Z_{acoustic} = Z_{11}$). Z_{11} has a complex value and can be separated into the real and imaginary parts as

$$Z_{11} = R_{11} + jX_{11}. \tag{3.1.12}$$

The acoustic resistance R_{11} represents the real power radiated into the medium in the form of a longitudinal wave, where the motion and the pressure are in phase. The imaginary part X_{11}

is called the acoustic reactance and represents the kinetic energy stored in the medium, where the motion and pressure are out of phase. Therefore, X_{11} acts as a mass load to the vibrating plate. Both R_{11} and X_{11} are functions of wave number ($k = \omega / c_m$, where ω and c_m are the frequency and sound speed in the medium) as well as the aperture size of the transducer.

For $ka \ll 1$, which implies that the aperture size is much smaller than the acoustic wave length, the transmitter will act as a point source, and X_{11} dominates the acoustic impedance. On the other hand, if $ka \gg 1$, which implies that the aperture size is much larger than the acoustic wavelength, R_{11} will be the dominant component in the acoustic impedance. As a result, it is approximately equal to the characteristic acoustic impedance of the medium as

$$R_{11} \approx Z_0 = \rho_m c_m, \tag{3.1.13}$$

where ρ_m is the medium density, and c_m stands for the sound speed in the medium. Since air-coupled CMUTs are generally designed with large cell sizes, which are larger than the acoustic wavelength, an approximation of purely real radiation impedance is made in this thesis. To achieve a higher accuracy, one can calculate the acoustic impedance for a given design referring to [70].

From Eqs (3.1.11) and (3.1.6), the acoustic pressure generated at the surface of the CMUT plate can be expressed as

$$P = Z_{11}\dot{u}_{rms} = \frac{3\sqrt{5}}{5} Z_{11}\dot{u}_a = Z_{11}(\dot{u}_0 + \dot{u}_{AC}) = Z_{11}\dot{u}_{AC} = Z_{11}\omega_{ac}u_{AC}, \tag{3.1.14}$$

where u_0 is the static average displacement at DC bias and under atmospheric pressure, and ω_{ac} is the frequency of the AC excitation voltage.

3.1.1 Quality Factor

The quality factor (Q factor) of a resonator is commonly defined as the ratio of the maximum energy stored to the energy dissipated per cycle by damping processes

$$Q = 2\pi \frac{E_{store}}{E_{dissipate/cycle}}. \tag{3.1.15}$$

Another definition of the Q factor is the ratio of resonance frequency to the -3dB bandwidth as

$$Q = \frac{f}{\Delta f_{-3dB}}, \tag{3.1.16}$$

where *f* is the resonance frequency, at which the amplitude of the output is maximum. Δf_{-3dB} is the -3dB frequency bandwidth and can be calculated from the frequency response. Eqs (3.1.14) and (3.1.15) are approximately equivalent when Q becomes larger, meaning the resonator becomes less damped.

For ultrasound imaging applications, a low Q factor, which indicates a broad bandwidth, is desired. This is because a large bandwidth results in a sharp pulse or less ringing effect in the time domain and thus allows a high axial imaging resolution. For applications such as gas sensing, a high Q factor is desired because it allows a high sensitivity of detecting small frequency shifts around the resonance frequency. However, for the CMUTs presented in this thesis, the Q factor is not a key design parameter since air-coupled ultrasonic transducers are normally actuated with burst signal, which is the main limitation of axial resolution. On the other hand, improving the bandwidth for vacuum-sealed air-coupled CMUTs is difficult due to the low damping effect of air. Even though the vented CMUT cell design, which makes use of the squeezing film effects to improve the damping effect, has been demonstrated with an improved bandwidth, the output power of such design is quite low [71][72].

Energy loss is a very important aspect for determining the Q factor. Studies show that, there are mainly five classes of energy loss in resonators. They are medium loss [73], support loss [74], thermo elastic damping loss [75], surface loss [76], and volume loss [77]. The overall Q factor is the combination of the Q factors corresponding to these losses

$$\frac{1}{Q} = \frac{1}{Q_{medium}} + \frac{1}{Q_{support}} + \frac{1}{Q_{thermoelastic}} + \frac{1}{Q_{surface}} + \frac{1}{Q_{volume}}. \tag{3.1.17}$$

For a vacuum-sealed CMUT cell, the medium loss is the dominant loss mechanism [77]. Hence Eq (3.1.17) is approximately equal to

$$Q = Q_{medium}. \tag{3.1.18}$$

The equilibrium equation of the mass-spring-damper system has the form of

$$\left[m + AX_{11}(f)\right]\ddot{u}_a + AR_{11}(f)\frac{3\sqrt{5}}{5}\dot{u}_a + k_1 u_a = 0. \tag{3.1.19}$$

The damped resonance frequency f_d can be determined by solving

$$f_d = \frac{\sqrt{4k_1\left[m + AX_{11}(f_d)\right] - \frac{9}{5}R_{11}{}^2(f_d)A^2}}{4\pi\left[m + AX_{11}(f_d)\right]}. \tag{3.1.20}$$

The Q factor can be calculated using

$$Q = \frac{f_d}{\Delta f_{-3dB}} = \frac{\sqrt{5\left[m + AX_{11}(f_d)\right]k_1}}{3AR_{11}(f_d)}. \tag{3.1.21}$$

The -3dB fractional bandwidth is therefore equal to

$$B_{-3dB} = \frac{\Delta f_{-3dB}}{f_d} = \frac{1}{Q} = \frac{3AR_{11}(f_d)}{\sqrt{5\left[m + AX_{11}(f_d)\right]k_1}}, \tag{3.1.22}$$

and the -6dB fractional bandwidth yields

$$B_{-6dB} = \frac{\Delta f_{-6dB}}{f_d} = \frac{\sqrt{3}\Delta f_{-3dB}}{f_d} = \frac{3\sqrt{3}AR_{11}(f_d)}{\sqrt{5\left[m + AX_{11}(f_d)\right]k_1}}. \tag{3.1.23}$$

In this thesis, since an approximation of purely real radiation impedance is made, Eq (3.1.19) can be simplified as

$$\ddot{u}_a + 2\xi\omega_0\dot{u}_a + \omega_0{}^2 u_a = 0, \tag{3.1.24}$$

where ξ denotes the damping factor and is given by

$$\xi = \frac{3\sqrt{5}Z_{11}A}{10\sqrt{k_1 m}}. \tag{3.1.25}$$

The damped frequency yields

$$f_d = \frac{\omega_0 \sqrt{1-\xi^2}}{2\pi}. \tag{3.1.26}$$

The Q factor can be calculated based on

$$Q = \frac{f_d}{\Delta f_{-3dB}} = \frac{1}{2\xi} = \frac{m\omega_0}{AZ_{11}} = \frac{4.05{t_0}^2}{a^2 Z_{11}} \sqrt{\frac{E\rho}{1-\upsilon^2}}. \tag{3.1.27}$$

The -3dB fractional bandwidth can be therefore derived to be

$$B_{-3dB} = \frac{a^2 Z_{11}}{4.05{t_0}^2} \sqrt{\frac{1-\upsilon^2}{E\rho}}, \tag{3.1.28}$$

and the -6dB fractional bandwidth yields

$$B_{-6dB} = \frac{a^2 Z_{11}}{4.05{t_0}^2} \sqrt{\frac{3(1-\upsilon^2)}{E\rho}}. \tag{3.1.29}$$

3.1.2 Capacitive Force

Assuming the CMUT as a pair of parallel plates, the capacitive force or electrostatic force induced by the DC bias V_{DC} can be calculated based on

$$F_e = \frac{1}{2} {V_{DC}}^2 \frac{dC_e}{du_a}. \tag{3.1.30}$$

where C_e is the capacitance between the plate and the bottom electrode. In the work [17], C_e is calculated based on two parallel plates at a separation distance of $g-u_a$. However, it is found that such assumption lacks accuracy and cannot give a precise prediction of the static and dynamic performance at the DC bias. Therefore, the actual capacitance, which takes the curvature of the deformed plate into consideration, is used in this thesis. It is calculated by integrating the capacitance over the entire plate area as [68][78]

$$C_e = \int_0^a \frac{2\pi r\varepsilon}{g-u(r)} dr = \frac{\varepsilon A \operatorname{arctan\,h}(\sqrt{3u_a/g})}{\sqrt{3u_a g}} = \frac{\varepsilon A \ln\left(\frac{1+\sqrt{3u_a/g}}{1-\sqrt{3u_a/g}}\right)}{2\sqrt{3u_a g}}. \tag{3.1.31}$$

The first and second derivatives of C_e with respect to u_a are:

$$\frac{dC_e}{du_a} = \frac{\varepsilon A}{2gu_a(1-\frac{3u_a}{g})} - \frac{C_e}{2u_a}, \tag{3.1.32}$$

and

$$\frac{d^2C_e}{du_a^2} = \frac{3\varepsilon A}{2g^2u_a(1-\frac{3u_a}{g})^2} - \frac{\varepsilon A}{2gu_a^2(1-\frac{3u_a}{g})} + \frac{C_e}{2u_a^2} - \frac{1}{2u_a}\frac{dC_e}{du_a}. \tag{3.1.33}$$

Taking all the forms of force into consideration, the equilibrium equation of the CMUT plate can be expressed as

$$F_{mass} = F_m + F_r + F_e + F_{atm}, \tag{3.1.34}$$

where F_{mass} is the inertia force, F_m represents the restoring force or mechanical force resulting from the clamped boundary, and F_r is the acoustic loading force. Assuming Eq 3.1.13 is valid, Eq 3.1.34 can be expended to be

$$m\frac{d^2u_a}{dt^2} + k_1u_a + \frac{3\sqrt{5}}{5}AZ_{11}\frac{du_a}{dt} - \frac{1}{2}V_{DC}{}^2\frac{dC_e}{du_a} - AP_{atm} = 0. \tag{3.1.35}$$

At static state, F_{mass} and F_r are equal to zero, and Eq (3.1.35) can be simplified as

$$k_1u_a - \frac{1}{2}V_{DC}{}^2\frac{dC_e}{du_a} - AP_{atm} = 0. \tag{3.1.36}$$

Therefore, V_{DC} can be expressed in terms of u_a as

$$V_{DC} = \sqrt{\frac{2\left(k_1u_a - AP_{atm}\right)}{\frac{dC_e}{du_a}}}. \tag{3.1.37}$$

Taylor expanding the fourth term of Eq (3.1.35) about the equilibrium position $u_a = u_0$ yields

$$\frac{1}{2}{V_{DC}}^2\frac{dC_e}{du_a}=\frac{1}{2}{V_{DC}}^2\left(\frac{5\varepsilon Ag-21\varepsilon Au_0}{4u_0(g-3u_0)^2}-\frac{5C_e(u_0)}{4u_0}+\left(\frac{15\varepsilon Au_0-3\varepsilon Ag}{4u_0^2(g-3u_0)^2}+\frac{3C_e(u_0)}{4u_0^2}\right)u_a\right),\tag{3.1.38}$$

where u_0 is the average static displacement under P_{atm} and at V_{DC}. Substituting Eq 3.1.38 into Eq 3.1.35 results in

$$\begin{aligned}&m\frac{d^2u_a}{dt^2}+\left(k_1-\frac{1}{2}{V_{DC}}^2\left(\frac{15\varepsilon Au_0-3\varepsilon Ag}{4u_0^2(g-3u_0)^2}+\frac{3C_e(u_0)}{4u_0^2}\right)\right)u_a\\&+\frac{3\sqrt{5}}{5}AZ_{11}\frac{du_a}{dt}-\frac{1}{2}{V_{DC}}^2\left(\frac{5\varepsilon Ag-21\varepsilon Au_0}{4u_0(g-3u_0)^2}-\frac{5C_e(u_0)}{4u_0}\right)-AP_{atm}=0.\end{aligned}\tag{3.1.39}$$

It is shown that at V_{DC}, the coefficient of the second term, which stands for the effective spring constant, is smaller than the lumped spring constant k_1 by an amount of $\frac{1}{2}{V_{DC}}^2\left(\frac{15\varepsilon Au_0-3\varepsilon Ag}{4u_0^2(g-3u_0)^2}+\frac{3C_e(u_0)}{4u_0^2}\right)$. This phenomenon is known as the “spring softening effect”. With the increase of V_{DC}, the effective spring constant will decrease to zero, and the electrostatic force becomes equal to the restoring force. The corresponding DC voltage is called “collapse voltage” or “pull-in voltage”. When V_{DC} is smaller than the collapse voltage, the plate will stabilize at a position. Once V_{DC} increases over the collapse voltage, the plate will lose its stability and collapse to the bottom. Therefore, combining Eqs (3.1.37) and (3.1.39), the collapse voltage can be calculated by solving

$$\begin{cases}k_1-\frac{1}{2}{V_{DC}}^2\left(\frac{15\varepsilon Au_0-3\varepsilon Ag}{4u_0^2(g-3u_0)^2}+\frac{3C_e(u_0)}{4u_0^2}\right)=0,\\ V_{DC}=\sqrt{\dfrac{2\left(k_1u_a-AP_{atm}\right)}{\dfrac{dC_e}{du_a}}}.\end{cases}\tag{3.1.40}$$

3.1.3 Q Factor at DC Bias

Defining the effective spring constant in Eq (3.1.39) as

$$k_2 = k_1 - \frac{1}{2} V_{DC}{}^2 \left(\frac{15\varepsilon A u_0 - 3\varepsilon A g}{4u_0^2 (g-3u_0)^2} + \frac{3C_e(u_0)}{4u_0^2} \right), \tag{3.1.41}$$

one can rewrite Eq (3.1.39) as

$$m\frac{d^2 u_a}{dt^2} + k_2 u_a + \frac{3\sqrt{5}}{5} A Z_{11} \frac{du_a}{dt} = \frac{1}{2} V_{DC}{}^2 \left(\frac{5\varepsilon A g - 21\varepsilon A u_0}{4u_0 (g-3u_0)^2} - \frac{5C_e(u_0)}{4u_0} \right) + AP_{atm}. \tag{3.1.42}$$

The natural resonance frequency at DC bias yields

$$\omega_{0dc} = \sqrt{\frac{k_2}{m}}. \tag{3.1.43}$$

Since the damping factor of Eq (3.1.42) is equal to

$$\xi_{dc} = \frac{3\sqrt{5} Z_{11} A}{10\sqrt{k_2 m}}, \tag{3.1.44}$$

the damped frequency becomes

$$\omega_{ddc} = \omega_{0dc}\sqrt{1-\xi_{dc}{}^2} = \omega_{0dc}\sqrt{1-\frac{9Z_{11}{}^2 A^2}{20 k_2 m}}. \tag{3.1.45}$$

Similar with Eq (3.1.27), the Q factor at DC bias can be derived to be

$$Q_{dc} = \frac{\sqrt{mk_2}}{AZ_{11}}. \tag{3.1.46}$$

The -3dB fractional bandwidths at DC bias is equal to

$$B_{-3dBdc} = \frac{3AZ_{11}}{\sqrt{5mk_2}}, \tag{3.1.47}$$

and the fractional bandwidth can be calculated based on

$$B_{-6dBdc} = \sqrt{3} B_{-3dBdc}. \tag{3.1.48}$$

3.1.4 Output Pressure

Assuming Eq (3.1.13) is valid and the AC excitation voltage is in the form of $V_{AC}\sin(\omega_{ac} t)$, Eq (3.1.39) can be rewritten as

$$m\frac{d^2u_a}{dt^2}+k_1u_a+\frac{3\sqrt{5}}{5}AZ_{11}\frac{du_a}{dt}-\frac{1}{2}\left(V_{AC}\sin(\omega_{ac}t)+V_{DC}\right)^2\frac{dC_e}{du_a}-AP_{atm}=0. \tag{3.1.49}$$

In order to operate the CMUT in the linear region, V_{AC} is normally given a small amplitude compared to that of V_{DC} .Therefore, the coefficient of the fourth term of Eq (3.1.49) can be simplified as:

$$-\frac{1}{2}\left(V_{AC}\sin(\omega_{ac}t)+V_{DC}\right)^2\frac{dC_e}{du_a}\approx-\frac{1}{2}\left(2V_{DC}V_{AC}\sin(\omega_{ac}t)+V_{DC}^2\right)\frac{dC_e}{du_a}. \tag{3.1.50}$$

The Taylor expansion of Eq (3.1.50) about $u_a=u_0$ yields

$$\begin{aligned}&-\frac{1}{2}\left(2V_{DC}V_{AC}\sin(\omega_{ac}t)+V_{DC}^2\right)\frac{dC_e}{du_a}=\\&-\frac{1}{2}\left(2V_{DC}V_{AC}\sin(\omega_{ac}t)+V_{DC}^2\right)\left(\frac{5\varepsilon Ag-21\varepsilon Au_0}{4u_0(g-3u_0)^2}-\frac{5C_e(u_0)}{4u_0}\right)\\&-\frac{1}{2}\left(2V_{DC}V_{AC}\sin(\omega_{ac}t)+V_{DC}^2\right)\left(\frac{15\varepsilon Au_0-3\varepsilon Ag}{4u_0^2(g-3u_0)^2}+\frac{3C_e(u_0)}{4u_0^2}\right)u_a.\end{aligned} \tag{3.1.51}$$

Substituting Eq (3.1.51) into Eq (3.1.49), one obtains

$$\begin{aligned}&m\frac{d^2u_a}{dt^2}+\left(k_1-\frac{1}{2}\left(2V_{DC}V_{AC}\sin(\omega_{ac}t)+V_{DC}^2\right)\left(\frac{15\varepsilon Au_0-3\varepsilon Ag}{4u_0^2(g-3u_0)^2}+\frac{3C_e(u_0)}{4u_0^2}\right)\right)u_a\\&+\frac{3\sqrt{5}}{5}AZ_{11}\frac{du_a}{dt}-\frac{1}{2}\left(2V_{DC}V_{AC}\sin(\omega_{ac}t)+V_{DC}^2\right)\left(\frac{5\varepsilon Ag-21\varepsilon Au_0}{4u_0(g-3u_0)^2}-\frac{5C_e(u_0)}{4u_0}\right)-AP_{atm}=0.\end{aligned} \tag{3.1.52}$$

Defining u_{AC} as the dynamic average displacement around the equilibrium position $u_a=u_0$, the total displacement can be expressed as $u_{AC}+u_0$. Substituting u_a in Eq (3.1.52) with $u_{AC}+u_0$ yields

$$\begin{aligned}&m\frac{d^2u_{AC}}{dt^2}+\left(k_1-\left(V_{DC}V_{AC}\sin(\omega_{ac}t)+\frac{1}{2}V_{DC}^2\right)\left(\frac{15\varepsilon Au_0-3\varepsilon Ag}{4u_0^2(g-3u_0)^2}+\frac{3C_e(u_0)}{4u_0^2}\right)\right)u_{AC}\\&+\frac{3\sqrt{5}}{5}AZ_{11}\frac{du_{AC}}{dt}=V_{DC}V_{AC}\left(\frac{\varepsilon A}{2u_0(g-3u_0)}-\frac{C_e(u_0)}{2u_0}\right)\sin(\omega_{ac}t).\end{aligned} \tag{3.1.53}$$

Eq (3.1.53) indicates a system with a time-varying stiffness, and it can only be solved via numerical approach. However, since V_{AC} is much smaller than V_{DC}, the stiffness term can be simplified as a constant by ignoring the time-dependent term $V_{DC}V_{AC}\sin(\omega_{ac}t)$, and Eq (3.1.53) becomes

$$m\frac{d^2u_{AC}}{dt^2}+k_2u_{AC}+\frac{3\sqrt{5}}{5}AZ_{11}\frac{du_{AC}}{dt}=V_{DC}V_{AC}\left(\frac{\varepsilon A}{2u_0(g-3u_0)}-\frac{C_e(u_0)}{2u_0}\right)\sin(\omega_{ac}t), \quad (3.1.54)$$

where

$$k_2=k_1-\frac{1}{2}V_{DC}^2\left(\frac{15\varepsilon Au_0-3\varepsilon Ag}{4u_0^2(g-3u_0)^2}+\frac{3C_e(u_0)}{4u_0^2}\right) \quad (3.1.55)$$

represents the effective spring constant. The solution of Eq (3.1.54) can be found to be

$$u_{AC}=U\sin(\omega_{ac}t-\varphi), \quad (3.1.56)$$

where

$$\begin{aligned}
&U=\frac{U_1}{k_2}\frac{1}{\sqrt{(1-\lambda^2)^2+(2\xi_{dc}\lambda)^2}},\\
&U_1=V_{DC}V_{AC}\left(\frac{\varepsilon A}{2u_0(g-3u_0)}-\frac{C_e(u_0)}{2u_0}\right), \quad (3.1.57)\\
&\lambda=\frac{\omega_{ac}}{\omega_{0dc}},\ \xi_{dc}=\frac{3\sqrt{5}Z_{11}A}{10\sqrt{k_2m}},\ \omega_{0dc}=\sqrt{\frac{k_2}{m}},\ \varphi=\tan^{-1}(\frac{2\xi_{dc}\lambda}{1-\lambda^2}).
\end{aligned}$$

The maximum amplitude of the average displacement U occurs at

$$\lambda=\sqrt{1-2\xi_{dc}{}^2}. \quad (3.1.58)$$

It should be noted that the frequency corresponding to the maximum displacement in the forced vibration is actually smaller than the resonance frequency of the damped free vibration. The maximum displacement is derived to be

$$U=\frac{U_1}{k_2}\frac{1}{2\xi_{dc}\sqrt{1-\xi_{dc}{}^2}}. \quad (3.1.59)$$

Substituting Eq (3.1.59) into Eq (3.1.48), we get the maximal output pressure as

$$P = Z_{11}\omega_{ac}U = \frac{U_1}{A}\frac{\sqrt{20k_2 m - 18Z_{11}^2 A^2}}{\sqrt{20k_2 m - 9Z_{11}^2 A^2}}. \tag{3.1.60}$$

Assuming $4mk_2 \gg A^2 {Z_{11}}^2$ is always valid, *P* can be further simplified as

$$P = \frac{U_1}{A}. \tag{3.1.61}$$

3.2 Equivalent Circuit Model

Even though a damped mass-spring model is more straightforward, the standard lumped element method, used to analytically model an ultrasound transducer, was derived from Mason's equivalent circuit [79], where the mechanical domain and the electrical domain are coupled together by a transformer. In this section, an equivalent circuit (Fig. 3.2.1), which acts as a full equivalence of the presented mass-spring-damper model, will be introduced in this section. It is a small-signal model, in which the CMUT cell is assumed to be pre-biased.

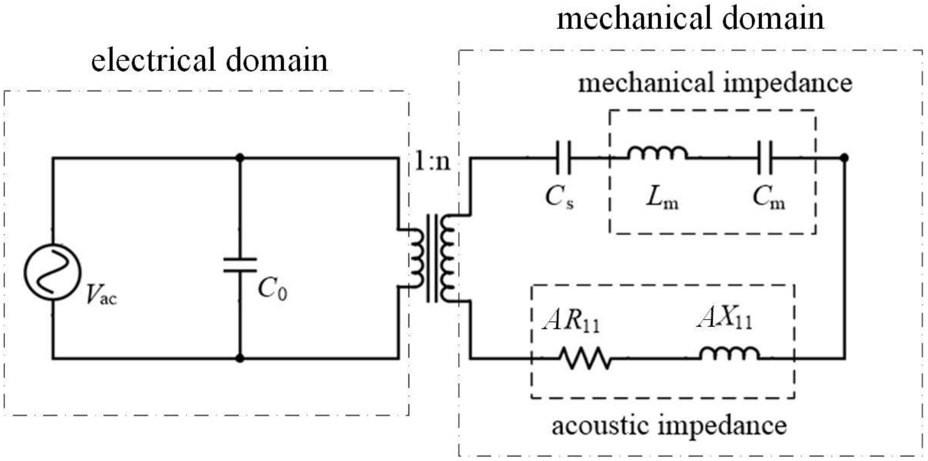

Figure. 3.2.1. Equivalent circuit of a CMUT cell.

As shown in Fig. 3.2.1, the equivalent circuit consists of two domains: the electrical domain on the left and the mechanical domain on the right. The capacitor C_0 in the electrical domain denotes the capacitance between the top and bottom electrodes of the CMUT cell under atmospheric pressure and at DC bias at static state, namely $C_0 = C_e(u_0)$. The input voltage V_{ac} represents the AC excitation voltage at the frequency of interest. Since the CMUT is assumed to be pre-biased, no DC voltage is physically input into the circuit.

A common analogy in the mechanical domain is that the electrical current represents the velocity, and the electrical voltage represents the force. Therefore, the mechanical domain is designed with a mechanical impedance to stand for the restoring force and mass of the clamped CMUT plate, an acoustic impedance to represent the acoustic loading of the medium, and a capacitor in series with the two impedances to denote the spring-softening effect of the plate. The capacitor in the mechanical impedance is equal to the reciprocal of the equivalent spring constant as

$$C_m = \frac{1}{k_1}. \tag{3.2.1}$$

The inductor in the mechanical impedance is equal to the mass of the plate as

$$L_m = m. \tag{3.2.2}$$

The capacitor representing the spring softening effect illustrated in Eq (3.1.39) has a negative amplitude and equals

$$C_s = -\frac{2}{V_{DC}{}^2\left(\dfrac{15\varepsilon A u_0 - 3\varepsilon A g}{4u_0^2(g-3u_0)^2} + \dfrac{3C_e(u_0)}{4u_0^2}\right)}. \tag{3.2.3}$$

Different from Eq 3.1.11, where the acoustic impedance is defined as the pressure over the area of the plate, the acoustic impedance in the equivalent circuit is defined to be the force over the area as

$$Z_{acoustic} = \frac{AP}{v} = \frac{F_r}{v} = AR_{11} + iAX_{11}. \tag{3.2.4}$$

The acoustic impedance is presented by a resistor (real part) and an inductor (imaginary part) connected in series in the mechanical domain of the equivalent circuit.

The transformer connecting the electrical and mechanical domains "converts" the AC excitation voltage to the electrostatic force. The capacitive force induced by V_{AC} is equal to the one induced by the superposition of V_{DC} and V_{AC} minus the one resulting from the DC bias as

$$F_e = \frac{1}{2}\left(V_{AC} + V_{DC}\right)^2 \frac{dC_e(u_0)}{du_0} - \frac{1}{2}V_{DC}^2 \frac{dC_e(u_0)}{du_0} \approx V_{DC}V_{AC}\frac{dC_e(u_0)}{du_0}. \tag{3.2.5}$$

As a result, the transforming ratio *n* can be derived to be

$$n = \frac{F_e}{V_{AC}} = V_{DC}\frac{dC_e(u_0)}{du_0}. \tag{3.2.6}$$

Comparing Eq (3.2.5) with Eq (3.1.61), it can be found that

$$n \cdot V_{AC} = AP. \tag{3.2.7}$$

This means that at resonance vibration, the output acoustic force is equal to the electrostatic force resulting from the AC excitation voltage. In other words, at resonance, all the electrical energy is transmitted into the medium, and the maximum efficiency is achieved.

For the convenience of calculation, the equivalent circuit can be simplified as a four-element circuit as shown below

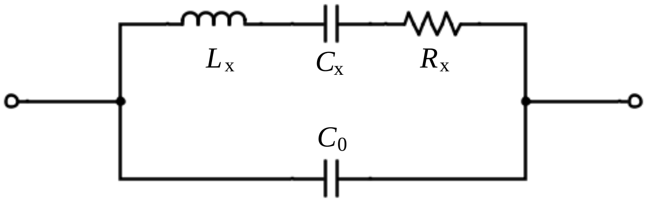

Figure. 3.2.2. Four element equivalent circuit model of a CMUT cell.

Based on the working principle of a transformer (equal power on each side), the elements in the mechanical domain in Fig. 3.2.1 can be converted to the following three elements

$$\begin{aligned} R_x &= Z_0 / n^2, \\ L_x &= \left(L_m + X_{11}\right) / n^2, \\ C_x &= \left(C_m + C_s\right) n^2. \end{aligned} \tag{3.2.8}$$

A simulation software, such as Simulink (The MathWorks, Inc), can be used to analyze the equivalent circuits. A real circuit can also be built for the same purpose.

So far, it has been demonstrated that the equivalent circuit model is a full equivalence of the mass-spring-damper model. Considering that the mass-spring-damper model is more straightforward, it will be used as the only modeling method in the following chapters.

Chapter 4 Annular CMUT Cells

4.1 Revisiting Motivation

The air-coupled CMUT cells reported to date have been primarily designed with one continuous boundary [80][81][82][83][84], which naturally leads to the adoption of circular geometry as it has no sharp corners and thus smaller concentrated stress and is easy to design and analyze due to the symmetric configuration. However, the transmit power of current air-coupled CMUTs is still considered weak. Several reasons can be summarized as follows. First, the piston-type motion has been demonstrated as the ideal mode of motion for CMUT [19][85]. Nevertheless, the actual deformation of a circular CMUT plate is parabolic, and as a consequence the total effective displacement is subject to the RMS displacement of the plate. Secondly, a high DC bias and AC excitation voltage are required to increase the RMS displacement in order to achieve a high output power [24][80][81]. However, the maximum amplitudes of the DC and AC voltages are restricted by the dielectric breakdown voltage of the insulating layer, which is also subject to fabrication contamination and defects. Thirdly, even though DC-free actuation strategies, which allow a CMUT plate to swing the entire cavity, were investigated, the strong non-linearity involves in these strategies make it difficult to model and analyze [86][87]. Last but not least, in order to perform beamforming and improve the acoustic power, realistic CMUTs are commonly designed in array forms. Since the space between neighbouring cells of a conventional circular-cell CMUT cells cannot be avoided, a high transducer fill factor is hard to be achieved.

Since the geometry and boundary conditions play important roles in the behaviours of a CMUT plate, more investigation about other geometries is prudent. A good example is the collapse-mode CMUT as shown in Fig 4.1, where the circular plate is in contact with the cavity bottom [88]. The boundary condition of a collapse plate is different from that of a conventional-mode plate by having two separate fixed boundaries. Experimental studies have shown that when a CMUT operates in collapse mode, the resonance frequency and the output pressure are both enhanced. The collapse-mode CMUT inspired the annular CMUT cell design in this thesis. In contrast to a conventional circular plate, an annular plate is clamped at the inner and outer edges, which result in two separate fixed constraints. It has three main advantages over the conventional circular design. First, a higher transmit sensitivity can be achieved due to a larger ratio of average-to-maximum displacement (RAMD) of the plate. Secondly, the receive sensitivity can be improved due to an increased capacitance between the top and bottom electrodes. Thirdly, multiple annular cells can be arranged in a concentric layout, which promises a high fill factor and allows acoustic focusing in the depth direction.

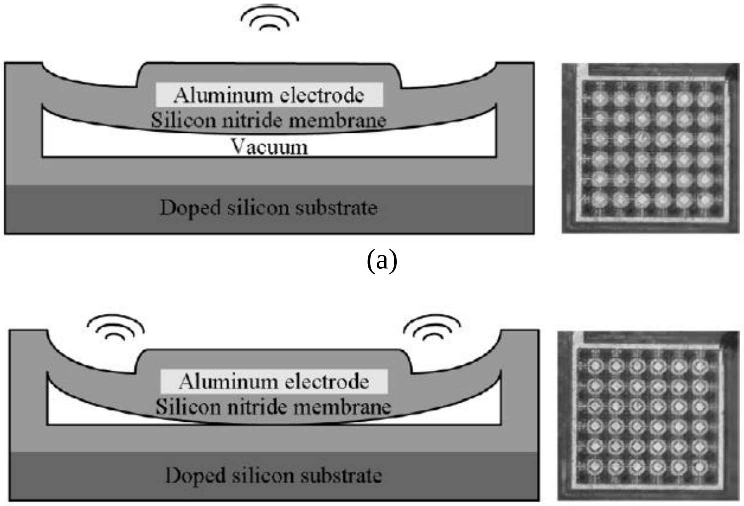

(a)

(b)

Figure. 4.1.1 Operation modes of a circular-cell CMUT: (a) conventional mode; (b) collapse mode [88].

In this chapter, the concept of an annular CMUT cell will be first introduced. A finite element model is built to evaluate the static and dynamic performance of an annular CMUT cell. Based on the finite element mode, a preliminary comparison study between the annular and circular cells is performed to reveal the advantage of the novel design. Next, the fabrication process and characterization results of the first-generation annular-cell CMUT are presented.

4.2 Design Concept

The static and dynamic behaviours of a CMUT cell plate are determined by the plate material, structural dimensions, and boundary conditions. For a typical vacuum-sealed circular plate, the maximum static displacement under atmospheric pressure locates at the center. However, if the plate is fixed at the center, the active area will become an annular shape while the maximum displacement moves to somewhere between the inner and outer edges. In Fig. 4.2.1, a schematic plot of such an annular CMUT cell is shown. The inner and outer radii of the annular plate are defined as a and b. The parameters r and h denote the radial position and the plate thickness. The effective cavity depth g can be calculated based on the actual cavity depth g_0, the insulating layer thickness t_i, and the relative permittivity of the insulating material ε_i using

$$g = g_0 + \frac{t_i}{\varepsilon_i}. \tag{4.2.1}$$

The ratio of the inner to outer radius is defined as

$$\tau = \frac{a}{b}. \tag{4.2.2}$$

The smaller τ is, the more similar the plate is to a “tent” which is supported at the center. In contrast, the larger τ is, the more similar the plate is to a “ring”.

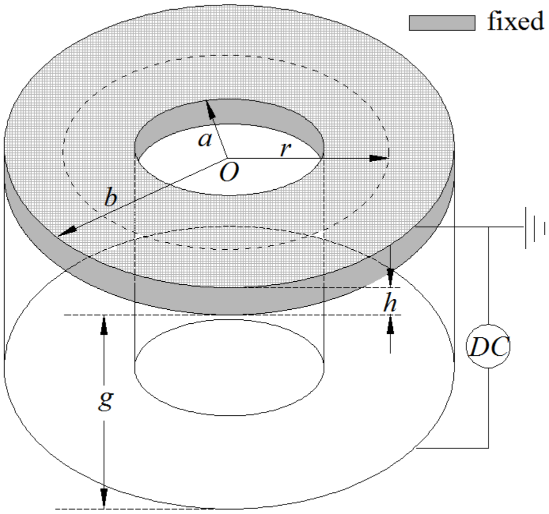

Figure. 4.2.1 Schematic of an annular CMUT cell.

When choosing the frequency of operation of an air-coupled transducer, one is forced to make a trade-off between the axial resolution and the penetration depth as high-frequency acoustic waves suffer significant attenuation loss in air. In this chapter, the natural resonance frequency was chosen as 100 kHz, which leads to a wavelength of 3.4 mm and acoustic attenuation factor of 2.19 dB/m at 20°C and 20% relative humidity [11]. Given a 100-kHz resonance frequency, the CMUT is required to be designed with a relatively thick plate. Otherwise, the undesired stress-stiffening effect will be induced and cause an increased resonance frequency and non-linear behaviours of the plate. The CMUT was finally designed to have a 20 µm thick plate with inner and outer radii of 1150 µm and 2500 µm, respectively. The plate thickness was selected based on the availability of commercial silicon-on-insulator (SOI) wafers from Ultrasil (Hayward, California). The outer radius was chosen to be 2500 µm as a middle ground: if it was too large, the thickness variation of SOI device layer might cause inconsistency, whereas if it was too small, the transmit power might be too small to be detected at a distance of several decimeters. The inner radius was determined based on the outer radius, plate thickness, and the designed resonance frequency using a FEA.

4.3 Finite Element Model

A finite element model of the annular CMUT cell was built in Comsol Multiphysics® (COMSOL Inc) to simulate its static and dynamic behaviours. When building the finite element model, the following conditions were defined:

1. The annular plate was made of highly conductive single crystal silicon which was simplified as a linear and isotropic material;
2. The insulating layer was made of wet thermal silicon dioxide;
3. The top surface of the plate was subjected to one standard atmosphere (atm);
4. The annular cavity was vacuum-sealed with depth of g;
5. The DC bias and AC excitation voltages were applied separately at the silicon plate and bottom surface of the cavity.

In the finite element model, five types of forces are involved: the inertia force $F_{inertia}$ caused by the mass of the plate, the restoring force $F_{restore}$ resulting from the boundary conditions, the acoustic force $F_{acoustic}$ induced by the ambient medium, the electrostatic force $F_{electro}$ induced by the DC bias and AC excitation, and atmospheric force F_{atm} due to atmospheric pressure. The dynamic equation can be expressed in terms of the five forces as

$$F_{inertia} + F_{restore} + F_{acoustic} + F_{electro} + F_{atm} = 0. \qquad 4.3.1$$

The physical properties of the materials involved in the model are listed in Table. 4.3.1

Table. 4.3.1 Physical properties of silicon and silicon dioxide used in the model.

Material	Density (kg/m^3)	Poisson's ratio	Young's modulus (GPa)	Relative permittivity
Si	2330	0.27	169	N/A
SiO_2	2200	0.17	70	3.9

4.3.1 Static Displacement under Atmospheric Pressure

The simulated static displacement under atmospheric pressure is shown in Fig. 4.3.1. Since the plate is symmetric about the central axis of its plane, the displacement u can be expressed as a function of the radial position *r*. In Fig. 4.3.2, the displacement profile cross section was shown. The maximum displacement $u_{\max}$ is located at $r = 1800$ μm and equals 7.24 μm. The radial position of the maximum displacement is 25 μm to the left side of the plate's median line. The 25-μm offset is induced by the asymmetric boundary conditions at the inner and outer edges. However, in contrast to the plate width (1350 μm), the offset is quite small. As a result, the displacement along the radial direction can be considered symmetrical about the plate median line.

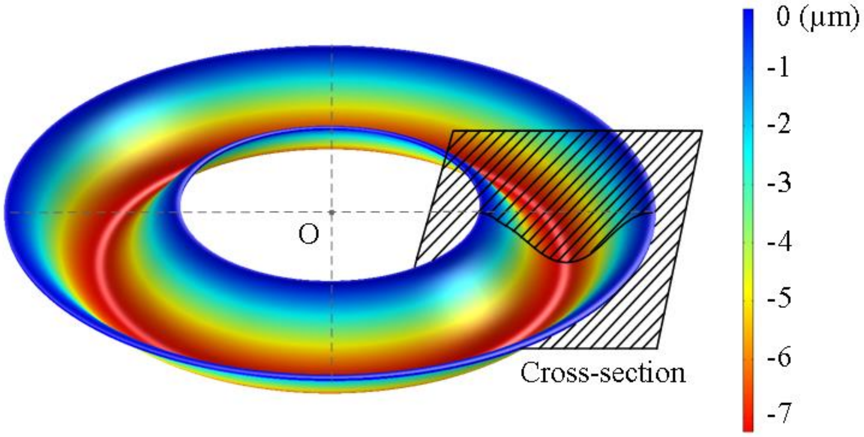

Figure. 4.3.1 Static displacement of the annular CMUT plate under atmospheric pressure.

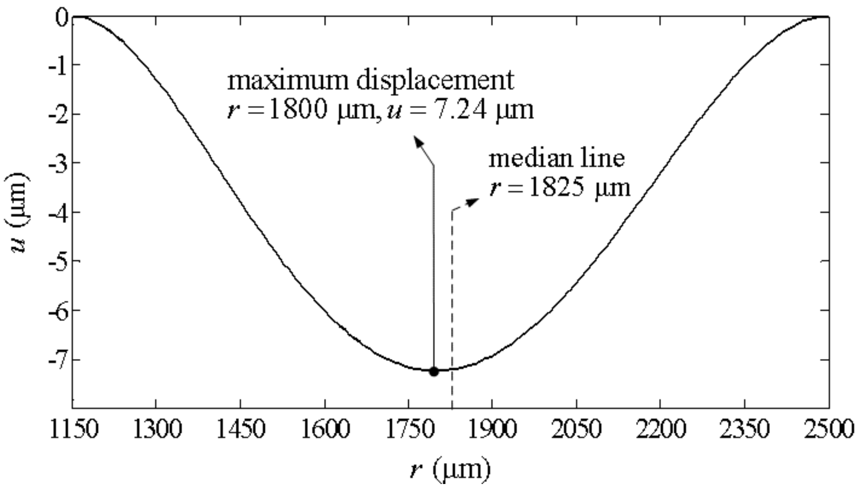

Figure. 4.3.2 Plate displacement profile on the cross section.

When studying a circular CMUT cell using a lumped model, the average displacement, which is defined as the average displacement over the entire plate area, is used as the displacement of the lumped mass [68][89]. In the same way, we define the average displacement of the annular plate as

$$u_a = \frac{1}{A}\int_a^b 2\pi r u(r)dr, \tag{4.3.2}$$

where A is the plate area, and u_a is the average displacement. u_a can be calculated to be 3.84 µm in this case. The RMS displacement is defined as

$$u_r = \sqrt{\frac{1}{A}\int_a^b 2\pi r u^2(r)dr}. \tag{4.3.3}$$

On the other hand, the RAMD is defined as

$$\gamma = \frac{u_a}{u_{\max}}, \tag{4.3.4}$$

and calculated to be 0.53. The dependence of RAMD on the design parameters of τ, *b*, and *h* was studied with τ ranging from 0.1 to 0.9 while b and *h* were fixed at different values. The simulation results are shown in Fig. 4.3.3.

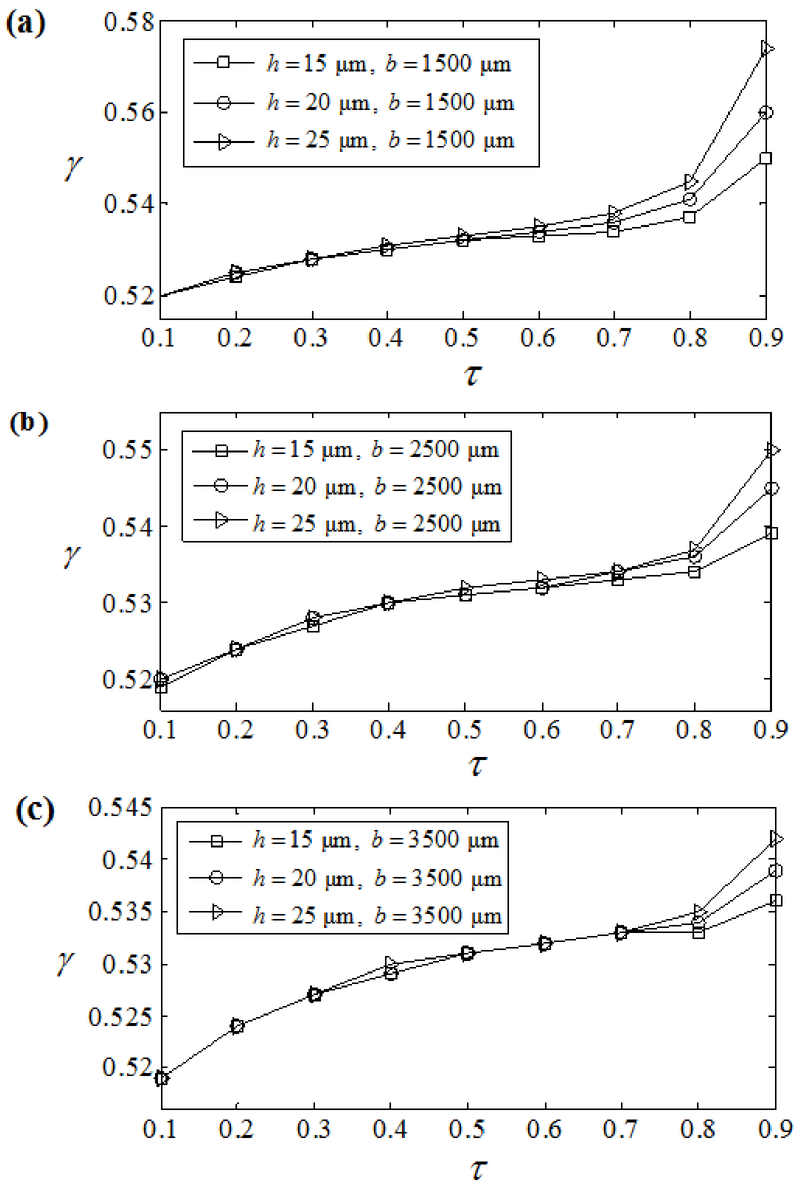

Figure. 4.3.3 Relationship between γ and τ for plate thicknesses of *h* =15, 20, and 30 µm and outer radii of a) 1500 µm, b) 2500, and c) 3000 µm, respectively.

From Fig. 4.3.3, the following conclusions may be drawn:

1. At fixed *b* and *h*, RAMD increases with the increase of τ ;
2. At fixed τ and *b*, *a* and larger *h* results in a larger RAMD, which is more obvious when τ is greater than 0.7;
3. At fixed *h* and τ , RAMD decreases with the increase of *b*.

Consequently, to achieve a larger RAMD at a certain designed frequency, a thick plate with a small inner radius should be used. In other words, a “tent” plate will result in a larger RAMD while a “ring” plate will lead to a smaller one. However, since the value of RAMD only varies within the range of 0.52 ~ 0.58, the dependence of it on the plate dimension parameters is relatively weak.

According to [68], the RAMD of a circular CMUT is 0.33. As a result, the RAMD of the designed annular CMUT is improved by 61%. In general, the RAMD of an annular CMUT can be improved by 58% to 76%. The larger the RAMD is, the more evenly the plate deflects, and the more the plate behaves like a piston. Due to a higher capacitance between the top and bottom electrodes, a piston has a larger volume displacement and a higher electro-mechanical coupling efficiency than a flexible plate. As a result, an annular CMUT should be more efficient in transmitting and receiving ultrasound.

4.3.2 Static Displacement at DC Bias

The amplitude of the DC bias is limited by the pull-in and breakdown voltages. The presented design was simulated to have a pull-in voltage of 498 V. The breakdown voltage of the 0.9-µm silicon dioxide insulating layer of the fabricated device, which will be introduced in Section 4.5, was measured to be around 200 V. Other factors, such as the capacity of the external power supply and safety issues can also limit the DC bias. In this Chapter, the maximum DC bias was set to 170 V as it was lower than the breakdown and pull-in voltages of the device and compatible with our power supply.

The simulated maximum displacement at 170-V DC bias and atmospheric pressure is 7.39 µm. The average displacement and RAMD were simulated to be 3.92 µm and 0.53, respectively. Compared with the static displacement without DC bias, the DC bias introduces an additional 0.15-µm maximum displacement and 0.08-µm average displacement.

4.3.3 Resonance Vibration

The dynamic performance of the presented CMUT was studied through its frequency response to the AC excitation. The CMUT was simulated to be biased at 100 V, 150 V, and 170 V and excited by a 20-V peak-to-peak (Vpp) AC excitation voltage. The simulation results (Fig. 4.3.4) indicate a typical response of an electrostatic-based transducer, namely, a higher DC bias results in a larger maximum dynamic displacement and a lower resonance frequency. At 100-V DC bias, the maximum displacement and resonance frequency is 1.14 µm and 98.53 kHz. At 150-V and 170-V DC bias, the resonance frequency decreases to 97.78 kHz and 97.38 kHz while the maximum dynamic displacement increases to 1.79 µm and 2.07 µm, respectively. The average displacement was simulated to be 0.60 µm, 0.95 µm, and 1.10 µm at 100-V, 150-V, and 170-V DC bias, respectively. The rms displacement was simulated to be 0.72 µm, 1.14 µm, and 1.33 µm at 100-V, 150-V, and 170-V DC bias, respectively.

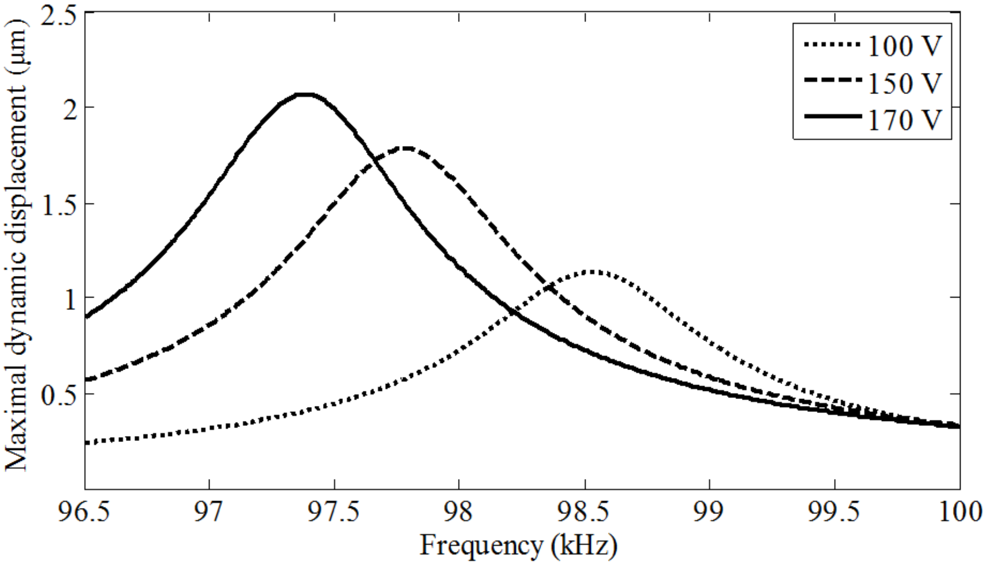

Figure. 4.3.4 Frequency responses at 100-V, 150-V, and 170-V DC biases.

The acoustic impedance of air can be expressed as

$$Z_{air} = R + iX, \tag{4.3.5}$$

where R and X are the resistive and reactive parts, respectively. The amplitude of the RMS acoustic pressure generated at the plate surface yields

$$P = |Z_{air}|\omega_{ac}u_{ac}, \tag{4.3.6}$$

where u_{ac} is the amplitude of the rms dynamic displacement induced by the AC excitation, and ω_{ac} is the frequency of the AC excitation. When biased at 100 V, 150 V and 170 V, the RMS output pressure was simulated to be 185.80 Pa, 288.60 Pa, and 331.15 Pa, and the transmit sensitivity yielded 18.58 Pa/V, 28.86 Pa/V, and 33.12 Pa/V. Based on Eq (4.3.6), the absolute value of the acoustic impedance was calculated to be 416.84 Rayls, 412.06 Rayls, and 406.93 Rayls, which was used to calculate the output pressure of the fabricated CMUT in Section 4.6. The -3-dB fractional bandwidths (FBWs) at 100-V, 150-V, and 170-V DC bias were simulated to be 0.89%, 0.88%, and 0.87%, respectively. The center frequencies of the -3-dB bandwidth at the three DC biases are consistent with the resonance frequencies.

4.4 Power Density Comparison between Circular and Annular Cells

Simulations were conducted on both circular and annular CMUT cells to study the efficacy of the latter design. The compared simulations shared the same natural resonance frequency (100 kHz), plate material (Si), membrane thickness (20 µm), insulating layer material ($\mathrm{SiO_2}$), insulating layer thickness (2 µm), DC biases (from 170 V to 370 V), and AC excitation (20 Vpp). 2 µm of insulating layer was selected to provide a high breakdown voltage (over 400 V). Based on the resonance frequency, the radius of the circular plate was simulated to be 911 µm. The annular plate was defined with the same inner and outer radius of the presented annular CMUT. The cavity depths for both designs were optimized for generating a maximum rms power density at the plate surface with an assumption that the plate would not touch the cavity bottom during vibrating. The transmit sensitivity was evaluated using the calculated rms output pressure divided by the amplitude of the AC excitation voltage. The optimized cavity depth g_{op}, simulated resonance frequency f_{dc} at DC bias V_{dc}, simulated rms output pressure P, calculated transmit sensitivity S_{tx}, calculated rms power intensity P_p, and the percentage of the transmit sensitivity and power intensity improvement S_{imp} and P_{imp} are summarized in Table. 4.4.1.

Table. 4.4.1 Comparison between circular and annular CMUT cell designs.

V_{dc} (V)		170	220	270	320	370
Circular cell	g_{op} (μm)	12.87	13.44	14.03	14.52	14.97
	f_{dc} (kHz)	97.10	96.25	95.60	94.70	93.90
	P (Pa)	377.3	422.5	444.3	481.2	511.3
	S_{tx} (Pa/V)	37.73	42.25	44.43	48.12	51.13
	P_p (W/m^2)	368.97	465.51	517.10	610.33	692.86
Annular cell	g_{op} (μm)	11.66	12.32	12.82	13.35	13.88
	f_{dc} (kHz)	94.90	93.90	92.50	91.50	90.70
	P (Pa)	586.3	627.9	657.2	705.0	731.4
	S_{tx} (Pa/V)	58.63	62.79	65.72	70.50	73.14
	P_p (W/m^2)	887.34	1041.68	1176.78	1383.21	1510.07
S_{imp}		55.4%	48.6%	48.4%	46.5%	43.0%
P_{imp}		140.5%	123.8%	127.6%	126.6%	117.9%

Table. 4.4.1 demonstrates that the transmit sensitivity and power intensity of an annular cell is on average 48.4% and 127.3% higher than that of a circular cell. Even though the size of a circular cell is smaller, and more circular cells can be put into the same area of an annular cell, the entire active area of such layout will become smaller because of the unavoidable spaces between neighboring circular cells. As a result, the total power improvement of an annular design may exceed 127.3%.

4.5 Fabrication

A wafer bonding process [46], in which the plate was bonded onto the substrate with predefined cavities, was used to fabricate the proposed annular CMUT cell. Since the plate and cavities were fabricated separately, one could independently control their dimensions as opposed to the limitations associated with surface micromachining process [16][36][40]. The three-dimensional (3-D) and cross-sectional views of the annular CMUT cell are shown in Fig. 4.5.1.

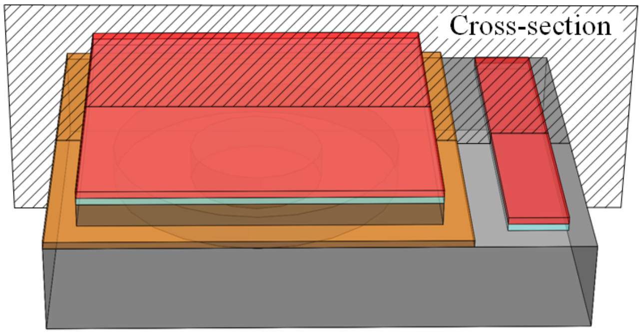

3-D View

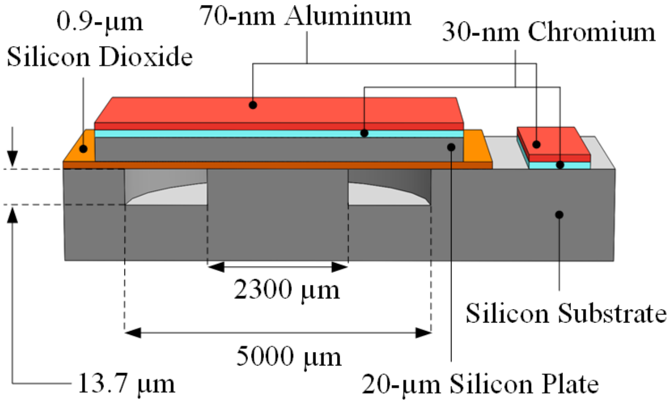

Cross-sectional View

Figure. 4.5.1 3-D and cross-sectional views of the annular CMUT.

The fabrication flow is illustrated in Fig. 4.5.2. First, a 4-inch, 500-μm thick, boron-doped, silicon substrate in <100> orientation with resistivity of $0.001\,\Omega\cdot\text{cm}$ was prepared as the bottom wafer. A 4-inch silicon-on-insulator (SOI) wafer with a 20-μm thick boron-doped, <111> orientation, $0.002\text{-}\Omega\cdot\text{cm}$ silicon device layer was prepared as the top wafer. In the second step, the substrate wafer was patterned and etched by deep reactive-ion etching (DRIE) (PlasmaPro Estrelas100, Oxford Instruments plc). For the top SOI wafer, 0.9 μm of wet thermal silicon dioxide, which would be used as the insulating layer, was grown on the device layer at 1100 °C. The wafer bonding was conducted in Step 3. First, both the top and bottom wafers were cleaned in standard SC-1 solution for 10 minutes at 80 °C, then rinsed in running DI water for 15 minutes and spin-dried. Afterwards they were treated by oxygen plasma for the purpose of surface activation for 10 minutes in the chamber of the wafer bonding machine (AWB-04 aligner wafer bonder, Applied Microengineering Ltd)..

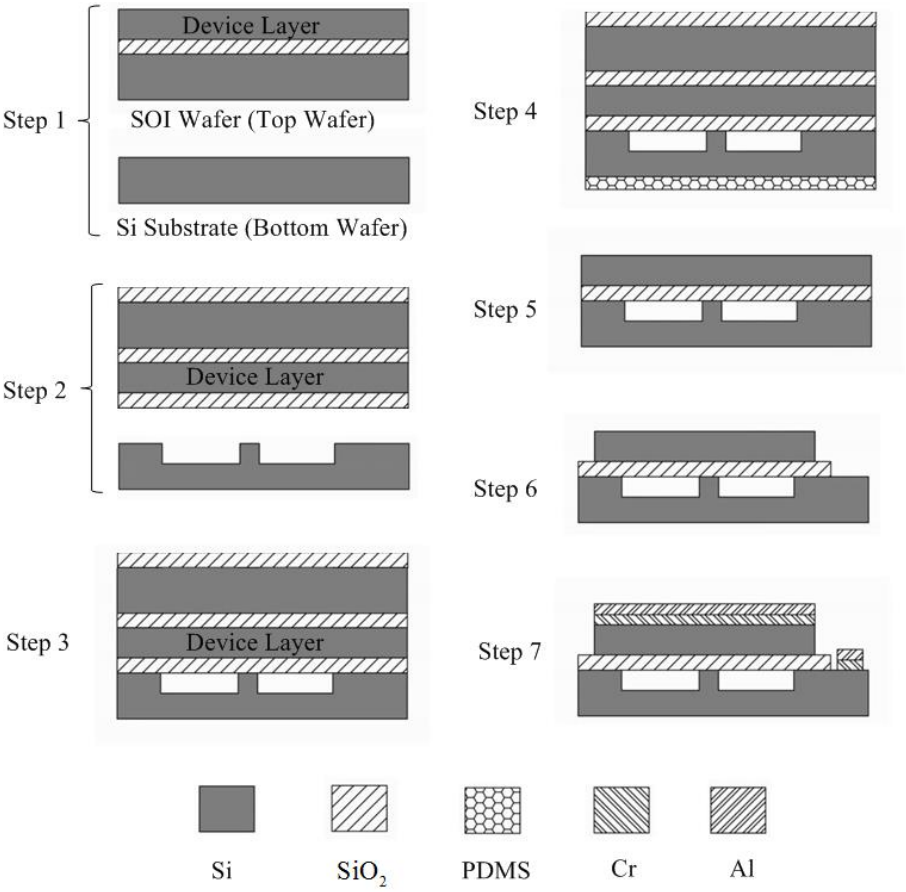

Figure. 4.5.2 Fabrication flow of the annular CMUT.

After plasma activation, the chamber was evacuated, and the top wafer was brought into contact with the bottom wafer. As soon as the two wafers contact, a compressive force of 2500 kN was exerted uniformly on the back sides of the two wafers and kept for 15 minutes to achieve a direct bonding. The direct-bonded pair was subsequently annealed at 1100 °C for 4 hours in a furnace with nitrogen injection. In the fourth step, a layer of Polydimethylsiloxane (PDMS) (Sylgard 184, Dow Corning Inc) was deposited and cured on the silicon substrate to protect it from being etched by the Tetramethylammonium hydroxide (TMAH) used in the following step. The bonded pair was then dipped in buffered oxide etch (BOE) to remove the silicon dioxide on the SOI handling layer introduced in step 2. The handling layer of the SOI wafer was etched away by 30% TMAH at 80 °C . Using BOE again, the buried silicon dioxide (BOX) layer of the SOI wafer was removed such that the device layer was exposed. The PDMS protection layer was simply peeled off by hands at the end of this step. Step 6 was used to isolate each CMUT plate as well as to expose a window on the substrate wafer for electrode deposition. In the last step, the top and bottom electrodes, which consisted of 30 nm of chromium covered with 70 nm of aluminum, were deposited through e-beam evaporation

A photograph of the fabricated device mounted and wire-bonded onto a printed circuit board (PCB) carrier is shown in Fig. 4.5.3. The ring-shaped shadow indicates the plate deformation due to atmospheric pressure. It should be mentioned that the illustrated device is the first-generation device and was fabricated using only one photomask (the one for cavity patterning) to save the cost. The electrode and device outlines were simply patterned with kapton tapes, which leads to the rough-looking appearance of the device. The first-generation devices were only used in this chapter to verify the FEA results and demonstrate the feasibility of the design concept. A new batch of second-generation devices, which was fabricated using a full set of photomasks, will be introduced in Chapter 5.

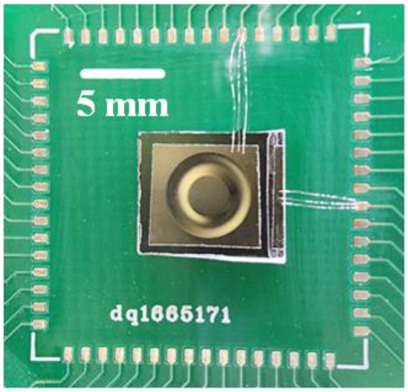

Figure. 4.5.3 A Photograph of the fabricated annular CMUT mounted and wire-bonded onto a PCB carrier.

4.6 Characterization

In this section, the fabricated device characterization for both the static and dynamic performance to demonstrate the transmit ability is presented. Since this thesis is mainly focused on transmitter CMUTs, which were designed with deep cavities to achieve a high output power, the presented devices are not optimized for receiving. Nevertheless, pitch-catch experiments were conducted to examine the fabricated device as a receiver. For the design of high-performance annular-cell CMUT for receiving, one can simply decrease the cavity depth to increase the receive sensitivity.

4.6.1 Static Displacement under Atmospheric Pressure

The static displacement resulting from atmospheric pressure was measured with a profilometer (Dektak 8 Stylus Profiler, Bruker Corp). The measured displacement is consistent along the circumferential direction. The displacement along the radial direction is shown in Fig. 4.6.1. The maximum displacement was measured to be 7.35 μm and occurred at $r = 1801\ \mu\text{m}$, which is 24 μm to the inner side of the plate's medium line ($r = 1825\ \mu\text{m}$). The average displacement was calculated to be 3.96 μm. As a result, the RAMD yields 0.54. The experiment results match well with the simulation results.

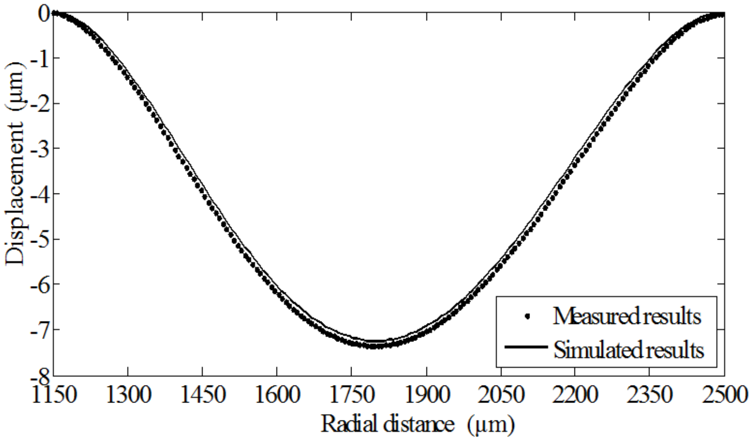

Figure. 4.6.1 Measured and simulated displacement along the radial direction.

4.6.2 Transmit Sensitivity

The transmit performance of the fabricated CMUTs was evaluated by two different AC excitation modes: a continuous wave (CW) and a 20-cycle burst. The dynamic displacement of the plate was measured with a laser Doppler vibrometer (OFV-5000, Polytec Inc). The rms output pressure at the plate surface was calculated based on the measured maximum dynamic displacement using Eqs (4.3.3) and (4.3.6).

A DC power source (GPR-30H10D, Good Will Instrument Co., Ltd) was used to bias the CMUT at 100 V, 150 V, and 170 V. At each bias voltage, the CMUT was excited by a 20-Vpp CW signal from a function generator (4040B, B&K Precision Corp). The CW signal was monitored using a digital oscilloscope (DSO-X 3034A, Agilent Technologies Inc). The frequency responses of the maximum dynamic displacements at different DC biases are consistent along the circumferential direction and plotted in Fig. 4.6.2. It is shown that a higher DC bias results in a larger dynamic displacement and a lower resonance frequency. The maximum dynamic displacement was measured to be 0.93 µm at 98.5 kHz, 1.57 µm at 96.2 kHz, and 2.18 µm at 94.5 kHz, at DC biases of 100 V, 150 V, and 170 V, respectively. Correspondingly, the rms output pressure at the plate surface was calculated to be 152.21 Pa, 249.07 Pa, and 338.27 Pa, and the transmit sensitivity was calculated to be 15.22 Pa/V, 24.91 Pa/V, and 33.83 Pa/V, respectively. The -3-dB FBW was measured to be 1.7%, 1.8%, and 1.4% when the CMUT was biased at 100 V, 150 V, and 170 V, respectively. The center frequency of the -3-dB bandwidth was measured to be 98.5 kHz, 96.3 kHz, and 94.7 kHz.

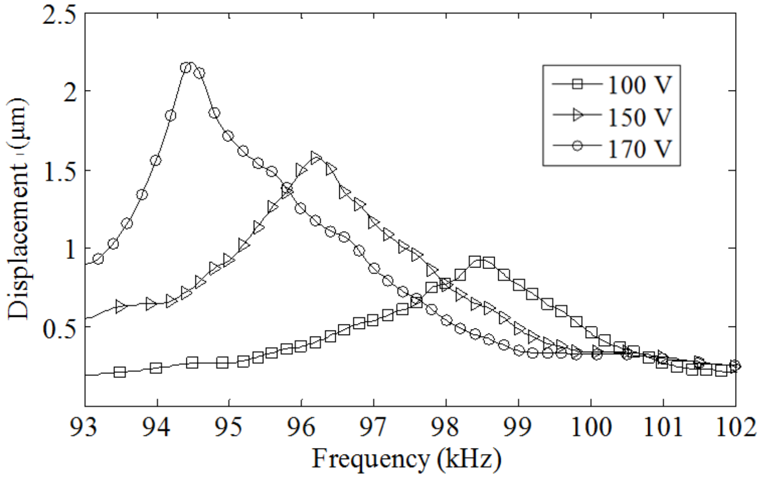

Figure. 4.6.2 Measured frequency responses of the CMUT biased at 100 V, 150 V, and 170 V and excited by a 20-Vpp CW signal.

The time-domain response at 170-V DC bias and 20-cycle, 94.5-kHz, 20-ppV burst excitation is shown in Fig. 4.6.3. The maximum dynamic displacement was measured to be 1.67 µm. The transmit sensitivity was calculated to be 25.85 Pa/V at the CMUT surface.

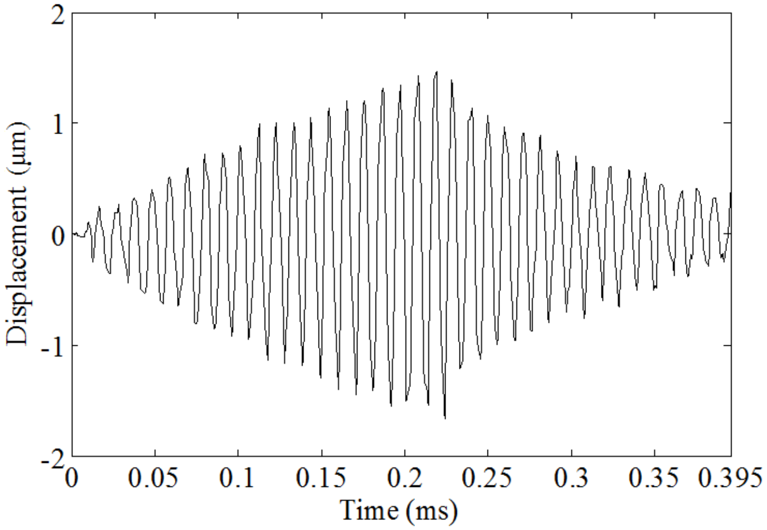

Figure. 4.6.3 Time-domain maximum dynamic displacement response when the CMUT was biased at 170-V DC and excited by a 20-cycle, 94.5-kHz, 20-ppV burst AC excitation signal.

4.6.3 Receive Sensitivity

The receive sensitivity was measured using a pitch-catch experiment setup consisting of two identical annular CMUTs, one for transmitting and the other for receiving. The two CMUTs were placed face to face at a separation distance of 20 cm, which was arbitrarily chosen such that the receiver was placed at the far field of the transmitter and was free from reflected echoes. Fig. 4.6.4 shows the schematic of the pitch-catch experiment setup. Both the transmit and receive CMUTs were biased at 170 V. The transmit CMUT was excited by a 20-cycle, 20-Vpp, 94.5-kHz burst-mode sinusoidal signal while the receive CMUT was connected to a pre-amplifier and a digital oscilloscope to measure the received signal. The pre-amplifier circuit is a transimpedance amplifier circuit which consists of an operational amplifier (OPA354, Texas Instruments Inc), a $25\text{-k}\Omega$ feedback resistor, and a 15-pF feedback capacitor.

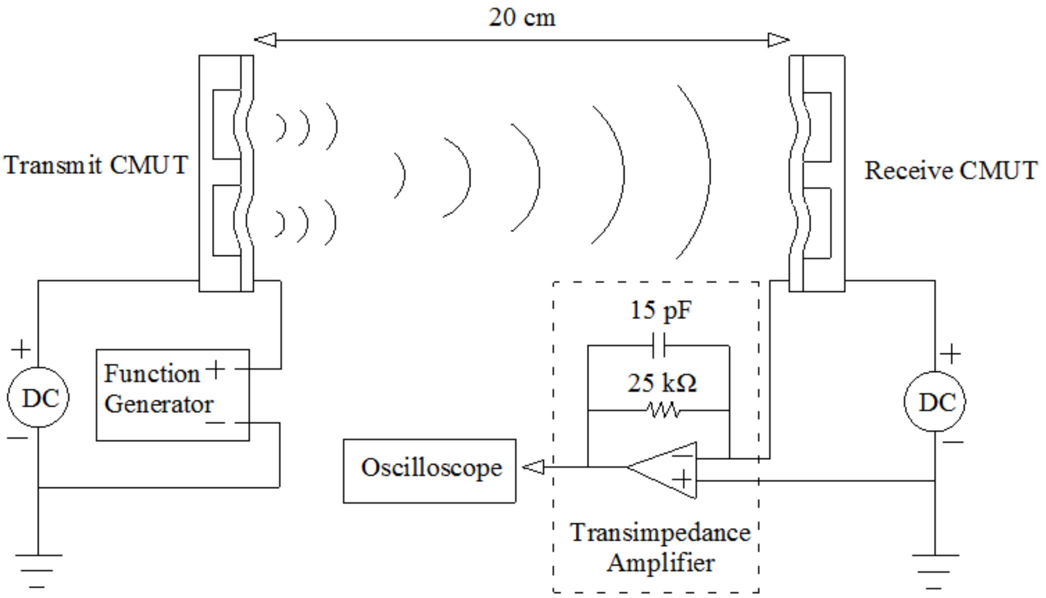

Figure. 4.6.4 Schematic of the pitch-catch experiment setup

Fig. 4.6.5 (top) shows the burst-model excitation signal. The output voltage from the pre-amplifier is shown in Fig. 4.6.5 (bottom). The maximum amplitude of the absolute pressure at the receive CMUT was simulated to be 5.3 Pa based on the measured output pressure at the transmitter's surface, air attenuation loss, and diffraction loss. The receive sensitivity was then calculated to be 7.7 mV/Pa (-42.3 dB re 1 V/Pa). In comparison, a continuous signal resulted in an absolute pressure of 7.2 Pa at the receive CMUT. The receive sensitivity was measured to be 15.0 mV/Pa (-36.5 dB re 1 V/Pa).

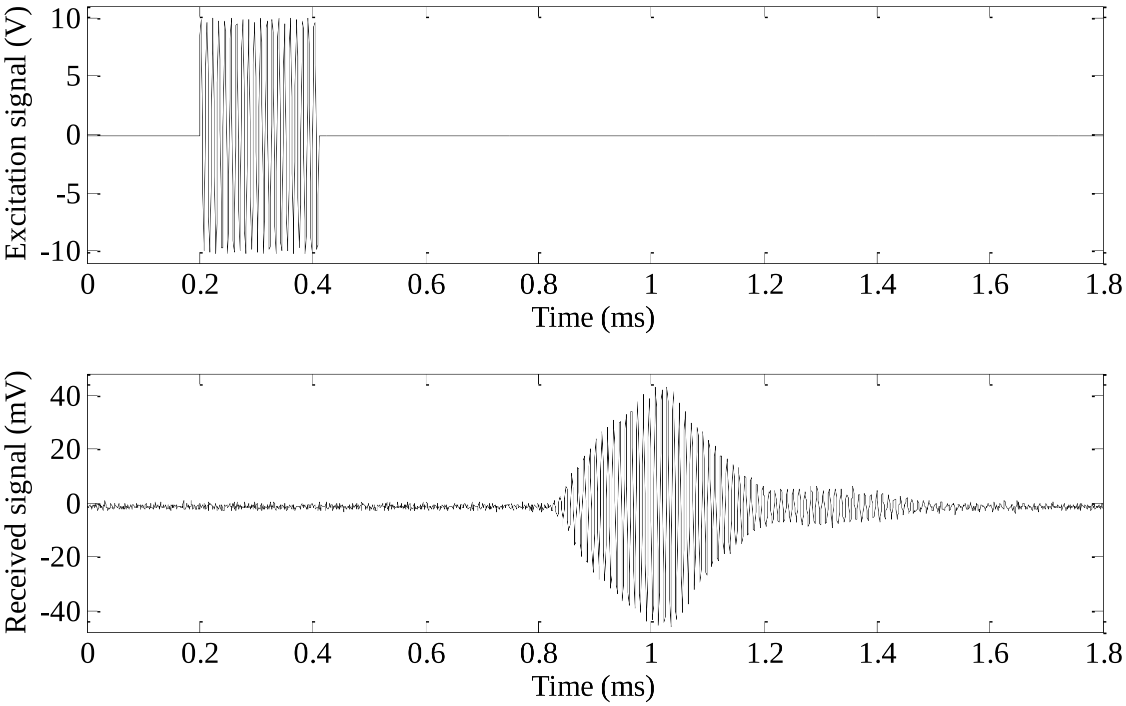

Figure. 4.6.5 Pitch-catch experiment results. (top) excitation voltage of the transmit CMUT; (bottom) received signal from the pre-amplifier of the receive CMUT.

Chapter 5 Lumped Element Modeling of an Annular CMUT Cell

In the last chapter, even though FEA predicted the performance of a particular annular CMUT design accurately, the computational expense makes it unsuitable in the design stage. Moreover, FEA could not demonstrate the principles of designing an annular-cell CMUT from an analytical perspective. As a result, it is necessary to develop an analytical model for more efficient analysis and design.

The lumped element model, which is a mass-spring-damper system and employs the average displacement as the spatial variable, has been used extensively when studying a circular CMUT cell. Determination of the lumped parameters, i.e., the lumped mass and spring constant, was based on the explicit formulas of the plate's resonance frequency and static displacement [17][68]. However, to the best of the author's knowledge, such explicit formulas have not been reported for annular plates. In this chapter, the explicit expressions of the resonance frequency and static displacement of an annular CMUT plate are first developed using the plate theory [69] and curve fitting method [90]. The lumped mass and spring constant are then derived based on these expressions. The electrostatic force is calculated through integrating the electrostatic pressure over the plate area. The dynamic formula, which employ the average displacement as the spatial variable and couple the inertial force of the lumped mass, restoring force of the equivalent spring, electrostatic force induced by the DC bias, atmospheric pressure, and the acoustic loading, are constructed and solved. FEA and experimental studies are conducted to verify the effectiveness of the analytical model in predicting the static and dynamic performance including the static displacement under atmospheric pressure and DC bias, pull-in voltage, and frequency and transient response of the maximum dynamic displacement. The model only involves the physics of the device and does not employ FEA for any parameter determination.

This chapter is organized as follows. Section 5.1 presents the modeling of a clamped annular plate based on the classical plate theory and curve fitting method. Explicit expressions of the natural resonance frequency and static displacement are also given in this section. The lumped element model is proposed and solved in Section 5.2, which is followed by verification studies in Section 5.3.

5.1 Modeling of a Clamped Annular Plate

An annular plate fixed at the inner and outer edges is shown in Fig. 5.1.1. The plate is assumed to be made of a linear isotropic material. The inner and outer radius, thickness, and material density of the plate are denoted by *a*, *b*, *h*, and ρ, respectively. The time, radial and angular spatial variables are represented by *t*, *r*, and θ, respectively.

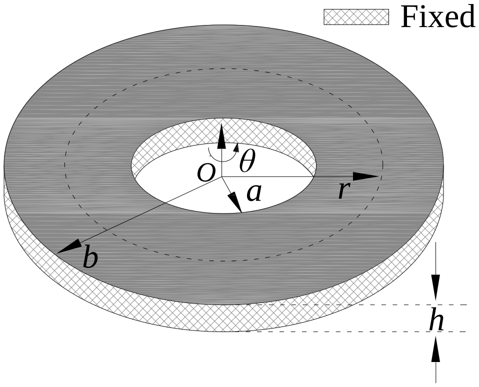

Figure. 5.1.1 An annular plate clamped at the inner and outer edges.

The differential equation of motion for transverse displacement $u(r,\theta,t)$ of the plate is given by [69]

$$D\left(\frac{\partial^2}{\partial r^2}+\frac{1}{r}\frac{\partial}{\partial r}+\frac{1}{r^2}\frac{\partial^2}{\partial\theta^2}\right)\left(\frac{\partial^2}{\partial r^2}+\frac{1}{r}\frac{\partial}{\partial r}+\frac{1}{r^2}\frac{\partial^2}{\partial\theta^2}\right)u+\rho h\frac{\partial^2 u}{\partial t^2}=0, \tag{5.1.1}$$

where *D* is the flexural rigidity and defined by

$$D=\frac{Eh^3}{12(1-\mu^2)}. \tag{5.1.2}$$

E is the Young's modulus, and μ is the Poisson ratio. Assuming free vibration, we can express $u(r,\theta,t)$ as

$$u(r,\theta,t)=U(r,\theta)\sin(\omega_0 t-\psi), \tag{5.1.3}$$

where $U(r,\theta)$ is the vibration amplitude, ω_0 is the resonance frequency, and ψ is a phase angle. According to [91], $U(r,\theta)$ has the form of

$$U(r,\theta)=R(r)\cos(n\theta), \tag{5.1.4}$$

where n $(n=0,\ 1,\ 2\ ,...,)$ represents the number of radial nodal lines. In axially symmetric vibration modal, *n* is equal to zero, and *U* is independent of θ. Taking Eq (5.1.3) back into Eq (5.1.1) yields

$$\left(\frac{\partial^2}{\partial r^2}+\frac{1}{r}\frac{\partial}{\partial r}+\frac{1}{r^2}\frac{\partial^2}{\partial\theta^2}+\beta^2\right)\left(\frac{\partial^2}{\partial r^2}+\frac{1}{r}\frac{\partial}{\partial r}+\frac{1}{r^2}\frac{\partial^2}{\partial\theta^2}-\beta^2\right)R\cos(n\theta)=0, \tag{5.1.5}$$

where we define

$$\beta^2=\sqrt{\frac{\rho h\omega_0{}^2}{D}}. \tag{5.1.6}$$

To find its solutions, Eq (5.1.5) is rewritten as two separate equations with "or" logic relationship

$$\frac{\partial^2 R}{\partial r^2}+\frac{1}{r}\frac{\partial R}{\partial r}+\left(\beta^2-\frac{n^2}{r^2}\right)R=0\ \Big\|\ \frac{\partial^2 R}{\partial r^2}+\frac{1}{r}\frac{\partial R}{\partial r}-\left(\beta^2+\frac{n^2}{r^2}\right)R=0. \tag{5.1.7}$$

The first equation of Eq (5.1.7) is the Bessel's differential equation of the *n*th order, and it has a solution of [92]

$$R(r)=C_1J_n(\beta r)+C_2N_n(\beta r), \tag{5.1.8}$$

where J_n and N_n are the Bessel's functions of the first and second kinds and can be expressed as

$$J_n(\beta r)=\sum_{m=0}^{\infty}\frac{(-1)^m}{m!(m+n)!}\left(\frac{\beta r}{2}\right)^{2m+n}, \tag{5.1.9}$$

$$N_n(\beta r)=\frac{J_n(\beta r)\cos(n\pi)-J_{-n}(\beta r)}{\sin(n\pi)}. \tag{5.1.10}$$

The second equation in Eq (5.1.7) is the modified Bessel's differential equation of the *n*th order and has the following solution [92]

$$R(r) = C_3 I_n(\beta r) + C_4 K_n(\beta r), \tag{5.1.11}$$

where I_n and K_n are the modified Bessel's functions of the first and second kinds, respectively. I_n and K_n can be expressed as

$$I_n(\beta r) = \sum_{m=0}^{\infty} \frac{1}{m!(m+n)!} \left(\frac{\beta r}{2} \right)^{2m+n}, \tag{5.1.12}$$

$$K_n(\beta r) = \frac{I_{-n}(\beta r) - I_n(\beta r)}{\sin(n\pi)} \left(\frac{\pi}{2} \right). \tag{5.1.13}$$

J_n, N_n, I_n and K_n have the following recursion properties [93]

$$\frac{d}{dr} J_n(\beta r) = \beta \left[\frac{n}{\beta r} J_n(\beta r) - J_{n+1}(\beta r) \right], \tag{5.1.14}$$

$$\frac{d}{dr} N_n(\beta r) = \beta \left[\frac{n}{\beta r} N_n(\beta r) - N_{n+1}(\beta r) \right], \tag{5.1.15}$$

$$\frac{d}{dr} I_n(\beta r) = \beta \left[\frac{n}{\beta r} I_n(\beta r) + I_{n+1}(\beta r) \right], \tag{5.1.16}$$

$$\frac{d}{dr} K_n(\beta r) = \beta \left[\frac{n}{\beta r} K_n(\beta r) - K_{n+1}(\beta r) \right]. \tag{5.1.17}$$

The general solution of $R(r)$ can be achieved by combining Eqs (5.1.8) and (5.1.11) as

$$R(r) = C_1 J_n(\beta r) + C_2 N_n(\beta r) + C_3 I_n(\beta r) + C_4 K_n(\beta r), \tag{5.1.18}$$

where $\left[C_1; C_2; C_3; C_4 \right]$ is the modal vector. The boundary conditions of the clamped annular plate can be expressed as

$$u\big|_{r=a} = 0, \ \left. \frac{\partial u}{\partial r} \right|_{r=a} = 0, \ u\big|_{r=b} = 0, \ \left. \frac{\partial u}{\partial r} \right|_{r=b} = 0. \tag{5.1.19}$$

Combining Eqs (5.1.14) to (5.1.19), we have

$$\begin{cases} C_1 J_n(\beta a) + C_2 N_n(\beta a) + C_3 I_n(\beta a) + C_4 K_n(\beta a) = 0, \\ C_1 J_n(\beta b) + C_2 N_n(\beta b) + C_3 I_n(\beta b) + C_4 K_n(\beta b) = 0, \\ C_1\left[\dfrac{n}{\beta a} J_n(\beta a) - J_{n+1}(\beta a)\right] + C_2\left[\dfrac{n}{\beta a} N_n(\beta a) - N_{n+1}(\beta a)\right] \\ +C_3\left[\dfrac{n}{\beta a} I_n(\beta a) + I_{n+1}(\beta a)\right] + C_4\left[\dfrac{n}{\beta a} K_n(\beta a) - K_{n+1}(\beta a)\right] = 0, \\ C_1\left[\dfrac{n}{\beta b} J_n(\beta b) - J_{n+1}(\beta b)\right] + C_2\left[\dfrac{n}{\beta b} N_n(\beta b) - N_{n+1}(\beta b)\right] \\ +C_3\left[\dfrac{n}{\beta b} I_n(\beta b) + I_{n+1}(\beta b)\right] + C_4\left[\dfrac{n}{\beta b} K_n(\beta b) - K_{n+1}(\beta b)\right] = 0. \end{cases} \tag{5.1.20}$$

Since $C_1,\ C_2,\ C_3,$ and C_4 have non-zero solutions, the determinant of the coefficient matrix of Eq (5.1.20) should equal zero. Taking $n = 0$, we have

$$\begin{vmatrix} J_0(\beta a) & N_0(\beta a) & I_0(\beta a) & K_0(\beta a) \\ J_0(\beta b) & N_0(\beta b) & I_0(\beta b) & K_0(\beta b) \\ -J_1(\beta a) & -N_1(\beta a) & I_1(\beta a) & -K_1(\beta a) \\ -J_1(\beta b) & -N_1(\beta b) & I_1(\beta b) & -K_1(\beta b) \end{vmatrix} = 0. \tag{5.1.21}$$

$\left[C_1; C_2; C_3; C_4\right]$ is equal to the first column of the adjugate matrix of Eq (5.1.21). We define the ratio of inner to outer radius as

$$\tau = \frac{a}{b}. \tag{5.1.22}$$

Based on Eqs (5.1.21) and (5.1.22), the relationship between βb and τ is plotted in solid lines in Fig. 5.1.2.

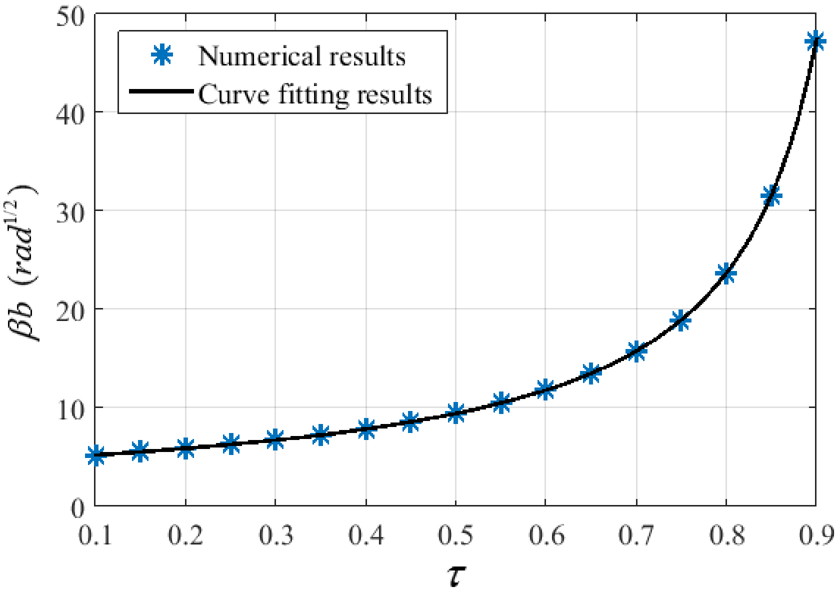

Figure. 5.1.2 Relationship between βb and τ .

Since the plotted curve has a very regular shape, curve fitting was employed to extract an approximate analytical expression of βb in terms of τ . Assuming the expression in the form of reciprocal of a quadratic function, it can be developed using nonlinear least squares fitting method [90] to be

$$\beta b = \frac{478.1}{\tau^2 - 102.8\tau + 101.8}. \tag{5.1.23}$$

The root-mean-square error (rmse) and the summed square of residuals (sse) of the fitting results are calculated to be 4.214×10^{-3} and 2.664×10^{-4}, respectively. Taking Eq (5.1.23) into Eq (5.1.6), the resonance frequency can be obtained as

$$\omega_0 = \sqrt{\frac{D}{\rho h b^4}}\left(\frac{478.1}{\tau^2 - 102.8\tau + 101.8}\right)^2. \tag{5.1.24}$$

The first-order modal shape yields

$$U(r) = C_1 J_0(\beta r) + C_2 N_0(\beta r) + C_3 I_0(\beta r) + C_4 K_0(\beta r). \tag{5.1.25}$$

When atmospheric pressure (P_{atm}) is taken into consideration, the equilibrium equation yields

$$D\left(\frac{\partial^2}{\partial r^2}+\frac{1}{r}\frac{\partial}{\partial r}\right)\left(\frac{\partial^2}{\partial r^2}+\frac{1}{r}\frac{\partial}{\partial r}\right)u=P_{atm}. \tag{5.1.26}$$

According to [94], the general solution of Eq (5.1.26) can be written as

$$u=u_{ps}+c_1+c_2r^2+c_3r^2\ln r+c_4\ln r, \tag{5.1.27}$$

where u_{ps} is a particular solution. To find u_{ps}, we rewrite Eq (5.1.26) as

$$\left(\frac{\partial^2}{\partial r^2}+\frac{1}{r}\frac{\partial}{\partial r}\right)M=\frac{P_{atm}}{D}, \tag{5.1.28}$$

where

$$M=\left(\frac{\partial^2}{\partial r^2}+\frac{1}{r}\frac{\partial}{\partial r}\right)u. \tag{5.1.29}$$

M can be found through undetermined coefficient method to be

$$M=\frac{P_{atm}r^2}{4D}. \tag{5.1.30}$$

In the same way, u_{ps} can be derived to be

$$u_{ps}=\frac{P_{atm}r^4}{64D}. \tag{5.1.31}$$

$c_1,\ c_2,\ c_3,$ and c_4 can then be determined by taking Eqs (5.1.29) and (5.1.31) into the boundary conditions Eq (5.1.19) as

$$\begin{cases}\dfrac{P_{atm}a^4}{64D}+c_1+c_2a^2+c_3a^2\ln a+c_4\ln a=0,\\ \dfrac{P_{atm}b^4}{64D}+c_1+c_2b^2+c_3b^2\ln b+c_4\ln b=0,\\ \dfrac{P_{atm}a^3}{16D}+2c_2a+c_3\left(2a\ln a+a\right)+c_4\dfrac{1}{a}=0,\\ \dfrac{P_{atm}b^3}{16D}+2c_2b+c_3\left(2b\ln b+b\right)+c_4\dfrac{1}{b}=0.\end{cases} \tag{5.1.32}$$

Taking a silicon (simplified as an isotropic material) annular plate with $h=20$ μm, $\tau=0.46$,

$b = 2500\ \mu\text{m}$, $\mu = 0.27$, and $E = 169\ \text{GPa}$ as example, the static displacement under atmospheric pressure ($P_{atm} = 1.01\times10^5\ \text{Pa}$) is shown in the dotted line in Fig. 5.1.3.

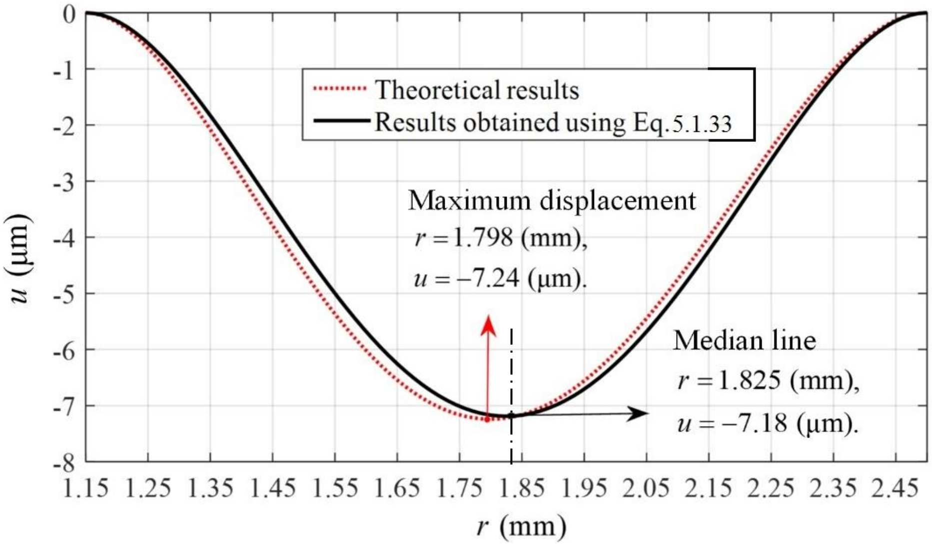

Figure. 5.1.3 Static displacement of a clamped silicon annular plate under atmospheric pressure.

Figure. 5.1.3 indicates that the maximum displacement locates at $27\ \mu\text{m}$ to the left of the median line (dot dash line), which means the displacement is not strictly symmetric about the median line. However, as the difference of the spatial distance is rather small compared to the width of the plate, the displacement can be simplified to be symmetric about the median line. As a result, we can define the expression of the displacement in a similar form with that of a clamped circular plate [68] as

$$u(r) = \frac{P_{atm}(b-a)^4}{384D}\left(1-\left(\frac{2r-a-b}{a-b}\right)^2\right)^2 = \frac{P_{atm}(r-a)^2(r-b)^2}{24D}. \qquad (5.1.33)$$

The constant coefficient (384) in front of D is determined by matching the maximum displacement with the theoretical result. The displacement profile, calculated using Eq (5.1.33), is plotted in the solid line in Fig. 5.1.3. Verification calculations were also conducted on plates with other dimensions, the results obtained with Eq (5.1.33) all showed very good agreement with the theoretical results.

5.2 Lumped Element Model

When investigating the electromechanical coupling effects in a CMUT cell, the lumped model, more specifically the one-dimensional mass-spring-damper model, is regularly used to simplify the spatially distributed system into a discrete system [17][68]. In this section, we will also present a similar lumped element model to guide the annular CMUT analysis and design. The cross-section schematic of the annular CMUT cell is shown in Fig. 5.2.1 (a), and its corresponding lumped model is shown in Fig. 5.2.1 (b).

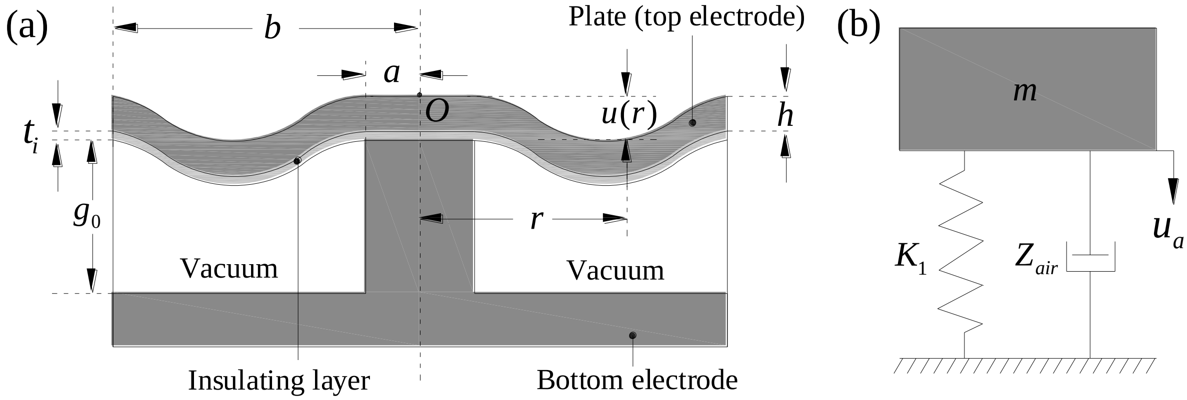

Figure. 5.2.1 Schematic (a) and lumped model (b) of an annular CMUT cell.

The cavity between the top and bottom electrodes is assumed to be vacuum with an equivalent depth of g, which is determined by the actual cavity depth (g_0), insulating layer thickness (t_i), and relative permittivity (ε_i) of the insulating material using

$$g = g_0 + \frac{t_i}{\varepsilon_i}. \tag{5.2.1}$$

m, k_1, and Z_{air} in Fig. 5.2.1 (b) represent the lumped mass, spring constant, and damping, respectively. Defining the electrostatic pressure as P_e, the total pressure exerted on the plate can be written as

$$P = P_{atm} + P_e. \tag{5.2.2}$$

Taking Eq (5.2.2) into Eq (5.1.33), the peak displacement u_p is derived to be

$$u_p = \frac{P(b-a)^4}{384D}. \tag{5.2.3}$$

The average displacement u_a is defined as

$$u_a = \frac{1}{A}\int_a^b 2\pi r u(r)dr = \frac{8}{15}u_p \approx 0.533u_p. \tag{5.2.4}$$

From Eq (5.2.4), the RAMD of a clamped annular plate is 0.533 which agrees with the result obtained in Chapter 4. On the other hand, the root-mean-square (rms) displacement is defined as

$$u_r = \sqrt{\frac{1}{A}\int_a^b 2\pi r u^2(r)dr} = \frac{48}{\sqrt{5670}}u_p \approx 0.638u_p, \tag{5.2.5}$$

which is 20% larger than the average displacement. Using u_a as the spatial variable, the spring constant can be calculated by dividing the total force with the average displacement as

$$k_1 = \frac{AP}{u_a} = \frac{720\pi D}{b^2}\frac{(1+\tau)}{(1-\tau)^3}. \tag{5.2.6}$$

Since the natural resonance frequency of a mass-spring system is

$$\omega_0 = \sqrt{\frac{k_1}{m}}, \tag{5.2.7}$$

m can be derived by combining Eqs (5.1.24) and (5.2.7) to be

$$m = \frac{720(\tau^2 - 102.8\tau + 101.8)^4}{478.1^4(1-\tau)^4}m_0, \tag{5.2.8}$$

where m_0 is the actual mass of the plate and equal to $\rho h\pi b^2(1-\tau^2)$. Considering that air-coupled applications usually require low operating frequencies (several hundred kHz), and air-coupled CMUT cells typically have larger sizes than the acoustic wave length, we simplify the acoustic impedance as plane wave impedance (specific impedance)

$$Z_{air} \approx \rho_{air}c_{air}, \tag{5.2.9}$$

where ρ_{air} and c_{air} are the density and sound speed of air, respectively. For more accuracy, the calculated radiation impedance for a given design could be used in place of Eq (5.2.9).

5.2.1 Static Analysis at DC Bias

The electrical capacitance between the top and bottom electrodes is defined as the capacitance integrated over the entire plate area

$$C_e = \int_a^b \frac{2\pi r \varepsilon_0}{g - u(r)} dr$$
$$= \frac{(b^2 - a^2)\pi\varepsilon_0}{2\sqrt{g}} \left(\frac{\arctan\left(\dfrac{\sqrt{15u_a/2}}{2\sqrt{\sqrt{15gu_a/8} - 15u_a/8}} \right)}{\sqrt{\sqrt{15gu_a/8} - 15u_a/8}} + \frac{\operatorname{arctanh}\left(\dfrac{\sqrt{15u_a/2}}{2\sqrt{\sqrt{15gu_a/8} + 15u_a/8}} \right)}{\sqrt{\sqrt{15gu_a/8} + 15u_a/8}} \right),$$

(5.2.10)

where ε_0 is the permittivity of vacuum. The first derivative of C_e with respect to u_a is

$$\frac{dC_e}{du_a} = \frac{(a-b)(a+b)\pi\varepsilon_0}{15\sqrt{2g}(15u_a - 8g)^2 u_a^{3/2}} \cdot \Big(30\sqrt{2u_a g}(15u_a - 8g)$$
$$+ \sqrt{2\sqrt{30u_a g} - 15u_a}\,(8\sqrt{30}g^{3/2} - 45u_a\sqrt{30g} - 225u_a^{3/2}) \arctan\left(\frac{\sqrt{u_a}}{\sqrt{\sqrt{8gu_a/15} - u_a}} \right) \qquad (5.2.11)$$
$$+ \sqrt{2\sqrt{30gu_a} + 15u_a}\,(8\sqrt{30}g^{3/2} - 45u_a\sqrt{30g} + 225u_a^{3/2}) \operatorname{arctanh}\left(\frac{\sqrt{15u_a}}{\sqrt{2\sqrt{30gu_a} + 15u_a}} \right) \Big).$$

The second derivative of C_e is

$$\frac{d^2C_e}{du_a^2} = \frac{3A\varepsilon_0}{2u_a(g - 3u_a)^2} - \frac{A\varepsilon_0}{2u_a^2(g - 3u_a)} + \frac{C_e}{2u_a^2} - \frac{1}{2u_a}\frac{dC_e}{du_a}. \qquad (5.2.12)$$

The electrostatic force F_e can be calculated based on

$$F_e = \frac{1}{2} V_{DC}{}^2 \frac{dC_e}{du_a}. \qquad (5.2.13)$$

Combining the inertial, restoring, electrostatic, and atmospheric force, the equilibrium equation of the lumped system is expressed as

$$m\frac{d^2u_a}{dt^2}+k_1u_a-\frac{1}{2}V_{DC}{}^2\frac{dC_e}{du_a}-AP_{atm}=0. \tag{5.2.14}$$

The electrostatic force can be expanded based on Taylor's expansion at $u_a = u_0$ (u_0 is the static average displacement under atmospheric pressure and at DC bias) as

$$\begin{aligned}\frac{1}{2}V_{DC}{}^2\frac{dC_e}{du_a} &= \frac{1}{2}V_{DC}{}^2\left(\frac{dC_e}{du_a}+\frac{d^2C_e}{du_a^2}(u_a-u_0)\right)+o(u_a-u_0)\\ &\approx \frac{1}{2}V_{DC}{}^2\left(C_{e-1}+C_{e-2}\cdot u_a\right),\end{aligned} \tag{5.2.15}$$

where

$$\begin{aligned}C_{e-1} &= (a-b)(a+b)\pi\varepsilon_0\Bigg(\sqrt{2\sqrt{30gu_0}+15u_0}\,(9\sqrt{2g}(25u_0-8g)\sqrt{2\sqrt{30gu_0}-15u_0}\\ &+(144g^2-32g\sqrt{30u_0g}-690gu_0+105u_0\sqrt{30gu_0}+1125u_0{}^2)\arctan\left(\frac{\sqrt{u_0}}{\sqrt{\sqrt{8gu_0/15}-u_0}}\right)\Bigg)\\ &+\sqrt{2\sqrt{30gu_0}-15u_0}\,(144g^2+32g\sqrt{30gu_0}-690gu_0-105u_0\sqrt{30gu_0}+1125u_0{}^2)\\ &\operatorname{arctanh}\left(\frac{\sqrt{15u_0}}{\sqrt{2\sqrt{30gu_0}+15u_0}}\right)\Bigg)\Bigg/\left(2\sqrt{2}(8g-15u_0)^2u_0\sqrt{120g^2u_0-225gu_0{}^2}\right),\end{aligned} \tag{5.2.16}$$

and

$$\begin{aligned}C_{e-2} &= -(a-b)(a+b)\pi\varepsilon_0\Bigg(\sqrt{2\sqrt{30gu_0}+15u_0}\,(5\sqrt{2g}(33u_0-8g)\sqrt{2\sqrt{30gu_0}-15u_0}\\ &+(80g^2-16g\sqrt{30gu_0}-330gu_0+75u_0\sqrt{30gu_0}+675u_0{}^2)\arctan\left(\frac{\sqrt{u_0}}{\sqrt{\sqrt{8gu_0/15}-u_0}}\right)\Bigg)\\ &+\sqrt{2\sqrt{30gu_0}-15u_0}\,(80g^2+16g\sqrt{30gu_0}-330gu_0-75u_0\sqrt{30gu_0}+675u_0{}^2)\\ &\operatorname{arctanh}\left(\frac{\sqrt{15u_0}}{\sqrt{2\sqrt{30gu_0}+15u_0}}\right)\Bigg)\Bigg/\left(2\sqrt{2}(8g-15u_0)^2u_0{}^2\sqrt{120g^2u_0-225gu_0{}^2}\right).\end{aligned} \tag{5.2.17}$$

By taking Eq (5.2.15) into Eq (5.2.14), we have

$$m\frac{d^2u_a}{dt^2}+k_2u_a-\frac{1}{2}{V_{DC}}^2C_{e-1}-AP_{atm}=0. \tag{5.2.18}$$

where $k_2=k_1-\frac{1}{2}{V_{DC}}^2C_{e-2}$. Since k_2 is the coefficient of the displacement variable, it is also the equivalent spring constant resulting from the spring softening effect. The pull-in voltage V_{pi} and its corresponding displacement can be found by assuming k_2 to be zero and Eq (5.2.14) to be satisfied

$$\begin{cases} k_2=0, \\ k_1u_0-\frac{1}{2}{V_{pi}}^2\left.\frac{dC_e}{du_a}\right|_{u_a=u_0}-AP_{atm}=0. \end{cases} \tag{5.2.19}$$

The resonance frequency at DC bias can be achieved by substituting k_1 in Eq (5.2.7) with k_2 to be

$$\omega_{0dc}=\sqrt{\frac{k_2}{m}}. \tag{5.2.20}$$

5.2.2 Resonance Vibration

Defining the AC actuation voltage as $V_{AC}=\bar{V}_{AC}\sin(\omega_{ac}t)$, the amplitude of the generated output pressure at the plate surface can be expressed as

$$P=Z_{air}\dot{U}_{rac}=Z_{air}\omega_{ac}U_{rac}, \tag{5.2.21}$$

where $\dot{U}_{rac}$ and U_{rac} are the amplitudes of the rms dynamic velocity $(\dot{u}_{rac})$ and rms dynamic displacement (u_{rac}), respectively. The dynamic equation at AC excitation yields

$$m\frac{d^2u_a}{dt^2}+k_1u_{ac}+AZ_{air}\frac{du_{rac}}{dt}-\frac{1}{2}\left(V_{AC}+V_{DC}\right)^2\frac{dC_e}{du_a}-AP_{atm}=0. \tag{5.2.22}$$

If small signal ($\bar{V}_{AC}<<V_{DC}$) is considered, the fourth term of Eq (5.2.22) can be simplified as $-1/2\left(2V_{DC}V_{AC}+V_{DC}^2\right)dC_e/du_a$, which can further be expanded at $u_a=u_0$ to be

$-1/2\left(2V_{DC}V_{AC}+V_{DC}^2\right)\left(C_{e\_1}+C_{e\_2}u_a\right)$. Considering $u_a=u_0+u_{ac}$, Eq (5.2.22) can be rewritten as

$$m\frac{d^2u_{ac}}{dt^2}+\left(k_1-\frac{1}{2}\left(2V_{DC}V_{AC}+V_{DC}^2\right)C_{e\_2}\right)u_{ac}+1.2AZ_{air}\frac{du_{ac}}{dt}=V_{DC}V_{AC}\left(C_{e\_1}+C_{e\_2}u_0\right). \quad (5.2.23)$$

Eq (5.2.23) indicates a system with time-dependent stiffness due to the existence of V_{AC}. However, since V_{AC} is a small signal, we can further simplify Eq (5.2.23) as

$$m\frac{d^2u_{ac}}{dt^2}+k_2u_{ac}+1.2AZ_{air}\frac{du_{ac}}{dt}=V_{DC}V_{AC}\left(C_{e\_1}+C_{e\_2}u_0\right). \quad (5.2.24)$$

Rewriting Eq (5.2.24), we have

$$\ddot{u}_a+2\xi\omega_{0dc}\dot{u}_a+\omega_{0dc}{}^2u_a=\frac{1}{m}V_{DC}V_{AC}\left(C_{e\_1}+C_{e\_2}u_0\right), \quad (5.2.25)$$

where ξ is the damping factor and equal to

$$\xi=\frac{0.6Z_{air}A}{\sqrt{k_2m}}. \quad (5.2.26)$$

The damped frequency at DC bias can be calculated to be

$$\omega_{ddc}=\omega_{0dc}\sqrt{1-\xi^2}. \quad (5.2.27)$$

The Q factor of a CMUT cell is mainly determined by the energy loss mechanisms involving the medium loss, support loss, thermo elastic damping loss, surface loss, and volume loss. For a vacuum-sealed CMUT cell, the medium loss is the dominant loss factor [84]. The Q factor of the lumped system is

$$Q=\frac{1}{2\xi}. \quad (5.2.28)$$

The -3-dB and -6-dB fractional bandwidth (FBW) are

$$B_{-3dB}=\frac{1}{Q}=2\xi, \quad (5.2.29)$$

and

$$B_{-6dB} = \sqrt{3}B_{-3dB} = 2\sqrt{3}\xi. \tag{5.2.30}$$

Eq (5.2.25) indicates a typical single-degree-of-freedom (SDOF) system with harmonic actuation. Its steady-state solution can be found to be [95]

$$u_{ac\_s} = U_{ac}\sin(\omega_{ac}t - \varphi), \tag{5.2.31}$$

where

$$\begin{gathered} U_{ac} = \frac{U_1}{k_2}\frac{1}{\sqrt{(1-\lambda^2)^2 + (2\xi\lambda)^2}}, \\ U_1 = V_{DC}\bar{V}_{AC}\left(C_{e\_1} + C_{e\_2}u_0\right), \\ \lambda = \frac{\omega_{ac}}{\omega_{0dc}},\ \varphi = \tan^{-1}\left(\frac{2\xi\lambda}{1-\lambda^2}\right). \end{gathered} \tag{5.2.32}$$

From the expression of U_{ac} in Eq (5.2.32), we can find that the maximum dynamic displacement corresponds to

$$\lambda = \sqrt{1-2\xi^2}, \tag{5.2.33}$$

which means that the AC frequency at the maximum dynamic displacement is slightly lower than ω_{0dc}. Substituting λ in U_{ac} with Eq (5.2.33), we have

$$U_{ac} = \frac{U_1}{k_2}\frac{1}{2\xi\sqrt{1-\xi^2}}. \tag{5.2.34}$$

Taking Eq (5.2.34) back to Eq (5.2.21), we can get the amplitude of the output pressure as

$$P = 1.2Z_{air}\omega_{ac}U_{ac} = \frac{U_1}{A}\sqrt{\frac{k_2 m - 0.72{Z^2}_{air}A^2}{k_2 m - 0.36{Z^2}_{air}A^2}}. \tag{5.2.35}$$

Since $mk_2 >> 0.72A^2{Z_{air}}^2$ normally holds, Eq (5.2.35) can be further simplified as

$$P = \frac{U_1}{A}. \tag{5.2.36}$$

5.2.3 Transient Response

Burst input signals are commonly used to drive air-coupled transducers for improved transmit efficiency [10]. In this sense, the transient response to a burst signal can better reflect the actual performance of an air-coupled CMUT. Based on [95], the transient solution of Eq (5.2.25) can be expressed as

$$u_{ac}(t)=e^{-\xi\omega_{0dc}t}U_{ac}\left(\sin(\varphi)\cos(w_{ddc}t)-\left(\frac{w_{ac}}{w_{ddc}}\cos(\varphi)-\frac{\xi\omega_{0dc}}{w_{ddc}}\sin(\varphi)\right)\sin(w_{ddc}t)\right)+u_{ac\_s}. \tag{5.2.37}$$

The first term represents the free vibration induced by the excitation signal and will attenuate with time. The second term indicates the forced vibration which is the same with Eq (5.2.31). Base on Eq (5.2.37), the transient velocity can be achieved by calculating the first-order derivation of $u_{ac}(t)$ as

$$\begin{aligned}\dot{u}_{ac}(t)=&-\xi\omega_{0dc}e^{-\xi\omega_{0dc}t}U_{ac}\left(\sin(\varphi)\cos(w_{ddc}t)-\left(\frac{w_{ac}}{w_{ddc}}\cos(\varphi)-\frac{\xi\omega_{0dc}}{w_{ddc}}\sin(\varphi)\right)\sin(w_{ddc}t)\right)\\&+e^{-\xi\omega_{0dc}t}U_{ac}\left(-w_{ddc}\sin(\varphi)\sin(w_{ddc}t)-\left(w_{ac}\cos(\varphi)-\xi\omega_{0dc}\sin(\varphi)\right)\cos(w_{ddc}t)\right)\\&+\omega_{ac}U_{ac}\cos(\omega_{ac}t-\varphi).\end{aligned} \tag{5.2.38}$$

At the moment when the input signal terminates, the lumped mass will hold an instantaneous velocity $\dot{u}_{ac\_0}$ and dynamic displacement u_{ac_0} which can further be used as the initial conditions to calculate the free vibration of the mass using

$$u_{ac}(t)=e^{-\xi\omega_{0dc}t}\left(\frac{\dot{u}_{ac\_0}+u_{ac\_0}\xi\omega_{0dc}}{w_{ddc}}\sin(w_{ddc}t)+u_{ac\_0}\cos(w_{ddc}t)\right). \tag{5.2.39}$$

5.3 Experimental and Simulation Verification

In this section, experimental and simulation studies on a fabricated second-generation annular CMUT (Fig. 5.3.1) were performed to verify the correctness of the developed lumped element model. The second-generation devices share the same architecture with the first-generation devices but was fabricated using a full set of photomasks based on the processes stated in Chapter 4. The vibrating plate is made of <111> single-crystal silicon with a resistivity of 0.002 $\Omega\cdot\text{cm}$. The substrate, which also acts as the bottom electrode, is made of 500-μm-thick silicon in <100> orientation with a resistivity of 0.001 $\Omega\cdot\text{cm}$. Wet thermal silicon dioxide (grown at

1100 ˚C) is used as the insulating layer. Except for being fabricated with a full set of photomasks, the second-generation devices are different from the first-generation for their smaller cavity depth, which leads to an improved sensitivity. The dimensions of the second-generation CMUT are listed in Table. 5.3.1.

Figure. 5.3.1 A photograph of the fabricated annular-cell CMUT on a PCB carrier.

Table. 5.3.1 Design dimensions of the annular-cell CMUT.

a (μm)	b (μm)	h (μm)	g_0 (μm)	t_i (μm)	g (μm)
1150	2500	20	12	1	12.26

FEA of the fabricated device was conducted using Comsol Multiphysics® (COMSOL Inc). The single-crystal silicon plate was simplified as a linear and isotropic elastic material in both the analytical calculation and FEA. The physical properties of the materials used in the two models are the same with those shown in Table. 4.3.1.

5.3.1 Static Displacement under Atmospheric Pressure

The static displacement of the annular CMUT plate under atmospheric pressure was measured using a profilometer (Dektak 8 Stylus Profiler, Bruker Corp). The measured, analytical, and simulation results are shown in Fig. 5.3.2. It demonstrates that the analytical results are in good agreement with the simulation and measured results.

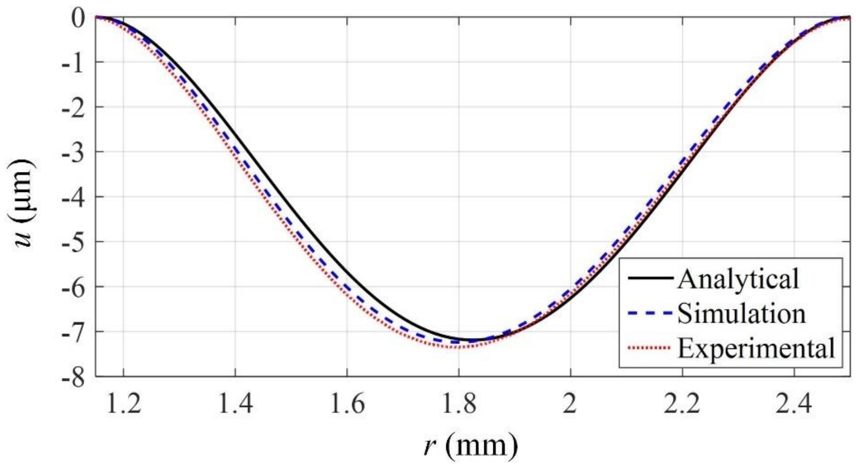

Figure. 5.3.2 Analytical, experimental, and simulation displacements under atmospheric pressure.

The results of the maximum displacement (u_p) and its position (r), average displacement (u_a), and the RAMDs are listed in Table. 5.3.2. Even though minor difference exists in the maximum displacements and its positions, the RAMDs are in good consistency. The results verify the correctness of the annular plate model presented in Section 5.2. On the other hand, we should note that the derivation of the static displacement did not involve the nonlinear strengthening effects caused by the plate deformation [96]. For designs with thin plate thickness and wide plate width, neglecting the effects may cause over estimation of the static displacement.

Table. 5.3.2 Static parameters under atmospheric pressure.

Parameters	u_p (μm)	r (μm)	u_a (μm)	RAMD
Analytical	7.189	1825	3.832	0.533
Simulation	7.239	1798	3.842	0.531
Experimental	7.351	1800	3.965	0.539

5.3.2 Static Displacement at DC Bias

FEA was used to verify the static displacement at DC bias and under atmospheric pressure. Experimental results are not provided because a charged device might cause damage to the profilometer during measurement. In the FEA model, the dielectric breakdown voltage of the insulating layer was assumed to be higher than the pull-in voltage. For the analytical results, the pull-in voltage (V_{pi}) was determined using Eq (5.2.19), the average displacement (u_a) was derived based on Eq (5.2.18), and the maximum displacement (u_p) was calculated by multiplying the calculated average displacement with the RAMD. Table. 5.3.3 summarizes the analytical and simulation results. Simulation results show that the RAMD is consistent at different DC biases, which verifies the assumption of constant RAMD in the analytical model.

Table. 5.3.3 Analytical and simulation results at DC bias and under atmospheric pressure.

V_{DC} (V)	Analytical				Simulation			
	V_{pi} (V)	u_a (μm)	u_p (μm)	RAMD	V_{pi} (V)	u_a (μm)	u_p (μm)	RAMD
100	341	3.878	7.271	0.533	334	3.888	7.328	0.531
150		3.936	7.380	0.533		3.947	7.442	0.530
200		4.025	7.548	0.533		4.039	7.620	0.530

5.3.3 Frequency Response

The effectiveness of the analytical model in predicting the frequency response was evaluated at DC biases of 100 V, 150 V, and 200 V. A 20-Vpp AC excitation signal was used to actuate the biased CMUT, and a laser Doppler vibrometer (LDV) (OFV-5000, Polytec Inc) was used to measure the maximum dynamic displacement of the vibrating plate. The analytical, simulation, and experimental frequency responses are plotted in Fig. 5.3.3.

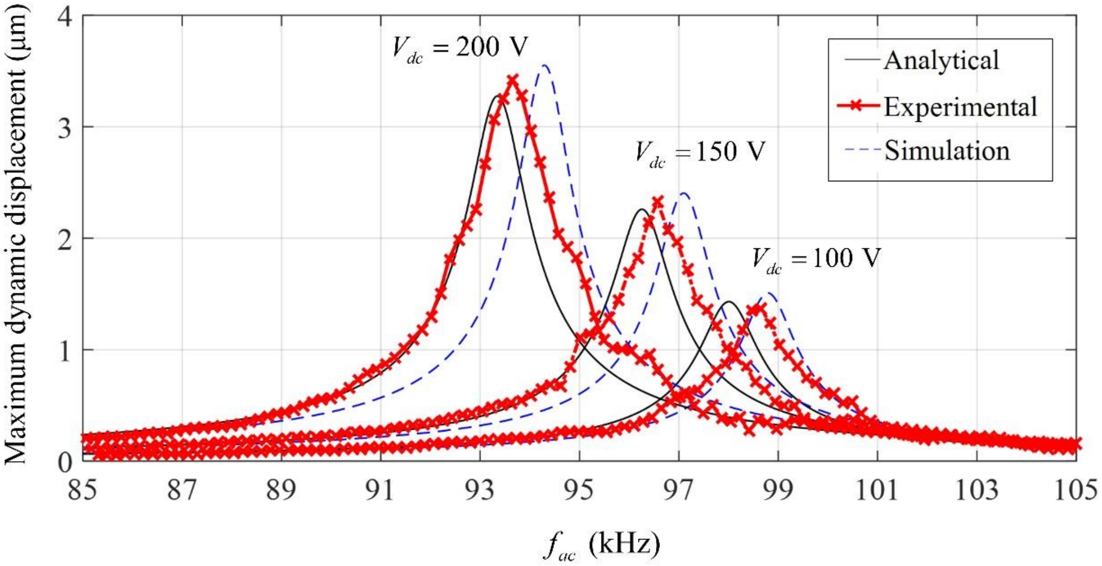

Figure. 5.3.3 Analytical, simulation, and experimental frequency responses of the maximum dynamic displacements.

The spring softening effect, namely a higher bias voltage leading to a lower resonance frequency and a larger dynamic displacement, can be observed. The analytical resonance frequencies at DC bias of 100 V, 150 V, and 200 V are calculated to be 98.01 kHz, 96.26 kHz, and 93.35 kHz, respectively. At 200-V bias, the analytical amplitude of the maximum displacement is 3.28 μm, which is very close to the experimental and simulation results. On the other hand, it can be found that the simulation data is more accurate than the analytical data at $V_{DC} = 100$ V. But with the increase of DC bias, the experimental data shifts more to a lower frequency than the simulation data does. One possible explanation is that the actual cavity depth is smaller than the designed value, and consequently the spring softening effect is more obvious at a higher DC bias. In other word, this is caused by fabrication errors. Overall, the analytical, experimental, and simulation results are very close, which verifies the accuracy of the analytical model.

A higher DC bias leads to a larger electric field and dynamic displacement, but also sets a higher requirement on the thickness and quality of the insulating layer (thermally grown oxide). On the other hand, since the whole plate is used as the top electrode, the plate beyond the cavity areas should be isolated or minimized in order to reduce the parasitic capacitance as well as the chance of dielectric breakdown. In this sense, the presented design can be further improved.

5.3.4 Transient Response

To verify the transient model presented in Section 5.2.3, the CMUT was biased at 200 V and actuated by a 20-Vpp 20-cycle burst input at the device's resonance frequencies (analytical: 93.35 kHz; simulation: 94.29 kHz; experimental: 93.65 kHz). The transient responses during and after the excitation signal are shown in Fig. 5.3.4. The analytical maximum transient displacement reaches 1.68 μm at the end of the burst excitation, and then attenuates to -3-dB after 10 cycles. In comparison, the simulated and measured vibration attenuates a little bit faster. One possible explanation is that the reactance impedance was ignored in the analytical model. Moreover, the in-plane energy coupled into the support substrates [77] was not considered, which can also explain why the measured attenuation was faster than the simulation results.

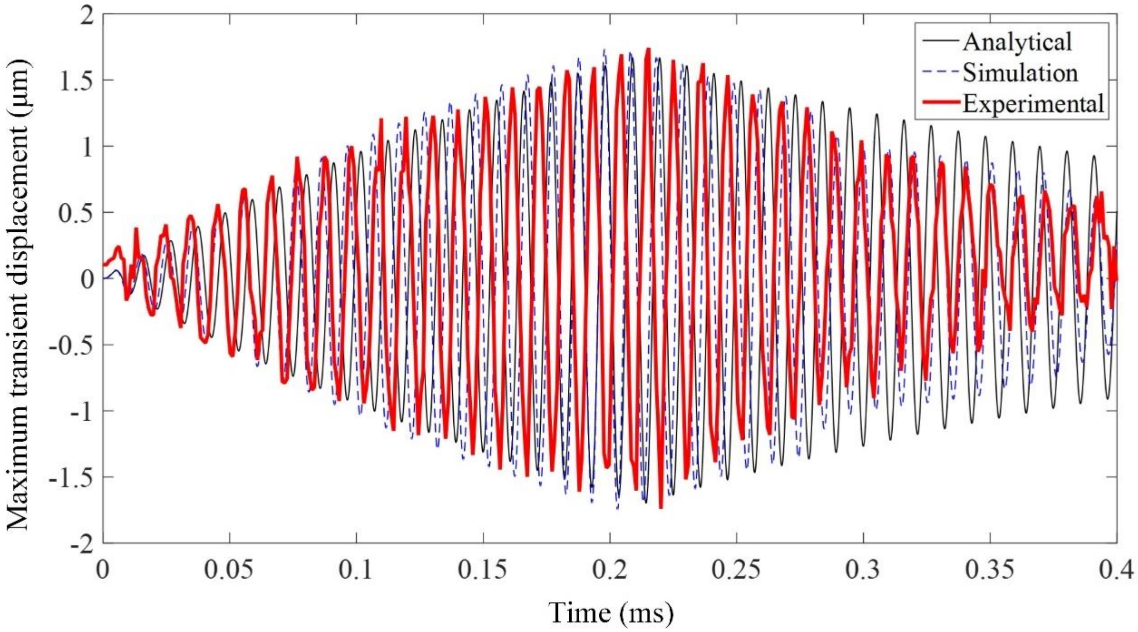

Figure. 5.3.4 Transient responses of the CMUT biased at 200-V and actuated by a 20-cycle 20-Vpp AC excitation signal.

Since the FEA model uses the results of the previous time step as the initial conditions to calculate the next time step, the time step, absolute tolerance, and relative tolerance must be set as small as possible to minimize the error accumulation and avoid non-convergence issues. As a result, about 7 hours were spent calculating the presented example using a personal computer (Processor: Intel(R) Core(TM) i7-4790 CPU @ 3.60 GHz; Random-access memory (RAM): 16 GB). In comparison, the analytical model, implemented using a customized program in MATLAB (The MathWorks, Inc), only took a few seconds to run. In this sense, the analytical model is more efficient in the design stage.

Chapter 6 Optimization and Comparison of Circular and Annular CMUT Cells

In the previous chapters, air-coupled annular-cell CMUTs have been studied through FEA, analytical, and experimental methods and demonstrated with a promising transmit sensitivity. In this chapter, three optimization design schemes are presented to maximize the transmit sensitivity and make a reasonable comparison between the circular and annular cells. In these schemes, the cavity depth is optimized based on the principle that the maximum plate displacement is equal to the cavity depth. In other words, the optimal design allows the plate to swing from the initial static position to the bottom of the vacuum cavity. Based on the lumped element modes, an optimization flow chart is constructed to implement the three schemes analytically. Circular and annular CMUTs with a common 97-kHz natural resonance frequency are fabricated and characterized to verify the efficacy of the optimization principle. Using the optimization flow chart, annular and circular cells with frequencies ranging from 100 to 300 kHz are optimized and compared.

6.1 Optimization Schemes

The parameters involved in the three optimization schemes (I, II, and III) are listed in Table. 6.1.1, where “g” indicates parameters with given values, “opt” denotes parameters to be optimized, and “max” and “min” refer to the parameters whose minimum and maximum parameter values are to be determined, respectively. In each design, the natural resonance frequency, plate thickness, and insulating layer thickness are fixed. This is due to the fact that the resonance frequency is determined by the application, and the plate and insulation layer thicknesses are most often limited by the availability of silicon-on-insulator (SOI) wafers and thermal oxidation cost and qualities, respectively [23][97]. In Scheme I, the cavity depth is optimized, such that the maximum surface power density can be achieved at a given DC bias and AC excitation voltage. Scheme II optimizes the cavity depth to minimize the requirement on DC bias when the output power density and AC voltage are predefined. Similar to Scheme II, Scheme III optimizes the cavity depth in order to minimize the AC driving voltage at a given output power density and DC bias.

Table. 6.1.1 Optimization schemes of air-coupled CMUT cells.

Parameters	Schemes		
	I	II	III
Nat. freq.	g	g	g
AC volt.	g	g	min
DC volt.	g	min	g
Power density	max	g	g
Plate thickness	g	g	g
Insulating layer thickness	g	g	g
Cavity depth	opt	opt	opt

The schematics of circular and annular cells are illustrated in Figs. 6.1.1 and 6.1.2, respectively. For the circular cell, the plate radius and thickness, insulating layer thickness, and cavity depth are denoted by x_0 , h_0 , t_{i0} , and g_{00} , respectively. The radial position and displacement of the circular plate are defined as x and $d(x)$, respectively. The maximum displacement under atmospheric pressure P_{atm} and at DC bias V_{DC} is defined as d_{p_DC}. The maximum dynamic displacement induced by AC excitation voltage (V_{AC}) is denoted by d_{p_AC}. For the annular cell, a and b denote the inner and outer radii, respectively. The plate thickness, thickness of insulating layer, and cavity depth are represented by h, t_i, and g_0, respectively. The displacement at radial position r is defined as $u(r)$. The maximum static displacement under ATM and at V_{DC} is denoted by u_{p_DC}. The maximum dynamic displacement at V_{DC} and V_{AC} is represented by u_{p_AC}.

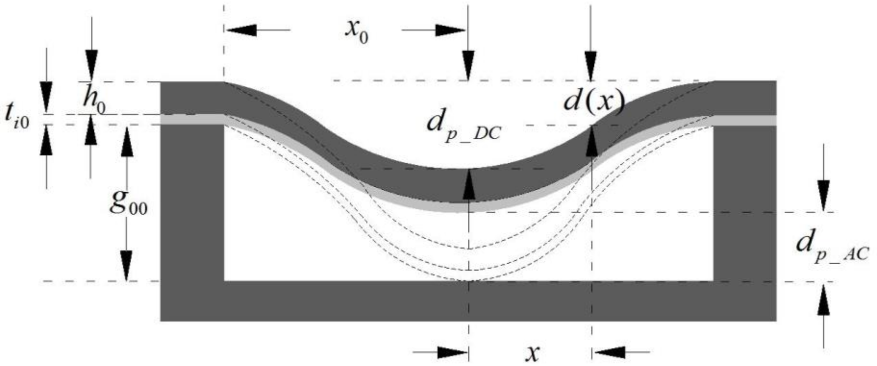

Figure. 6.1.1. Cross-section schematic of a circular CMUT cell.

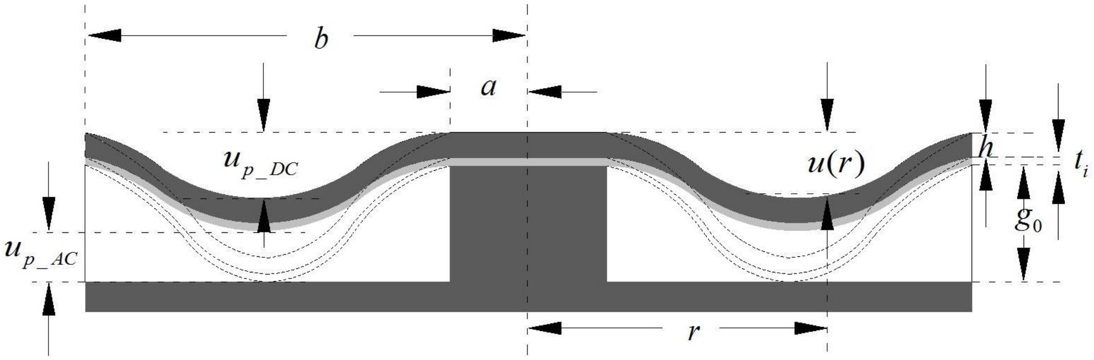

Figure. 6.1.2. Cross-section schematic of an annular CMUT cell.

The cell plates shown in Figs. 6.1.1 and 6.1.2 are laminate structures and simplified as single-layer structures in the previous chapters. In order to improve the accuracy of the optimization calculation, the actual laminate structure of the plates will be taken into consideration in this chapter. However, since the insulating layer is normally much thinner than the silicon layer, its residual stress will be ignored considering its little contribution to the plate deformation.

The cavity depth is optimized based on the principle that the maximum plate displacement equals the cavity depth. In other words, a larger or smaller cavity depth will either result in a lower electrical coupling efficiency or hinder the plate movement. Therefore, the optimized cavity depth of a circular CMUT cell can be described as

$$g_{00} = d_{p\_DC} + d_{p\_AC}. \tag{6.1.1}$$

The optimized cavity depth of an annular cell can be governed by

$$g_0 = u_{p\_DC} + u_{p\_AC}. \tag{6.1.2}$$

6.2 Lumped Element Models

For reading convenience, we will briefly revisit the lumped element models of both air-coupled circular and annular cells before introducing the optimization flow chart. Meanwhile, modifications are made to the expressions of the plate flexural rigidities to take the laminate plate structures into account.

6.2.1 Circular Cell

The static displacement of a clamped circular plate under uniform pressure P is expressed as

$$d(x) = \frac{P{x_0}^4}{64D_0}\left(1-\frac{x^2}{{x_0}^2}\right)^2, \tag{6.2.1}$$

where D_0 is the plate flexural rigidity. For the presented laminate structure, D_0 can be calculated based on [98]

$$\begin{aligned} D_0 &= \frac{B_{01}D_{01}-{C_{01}}^2}{B_{01}},\ B_{01} = \frac{E_i t_{i0}}{1-{\mu_i}^2}+\frac{Eh_0}{1-\mu^2}, \\ C_{01} &= \frac{E_i((h_0+t_{i0})^2-{h_0}^2)}{2(1-{\mu_i}^2)}+\frac{E{h_0}^2}{2(1-\mu^2)}, \\ D_{01} &= \frac{E_i((h_0+t_{i0})^3-{h_0}^3)}{3(1-{\mu_i}^2)}+\frac{E{h_0}^3}{3(1-\mu^2)}. \end{aligned} \tag{6.2.2}$$

The maximum displacement at $x = x_0$ is equal to

$$d_p = \frac{P{x_0}^4}{64D_0}. \tag{6.2.3}$$

The average displacement of a clamped circular plate is defined as

$$d_a = \frac{1}{A_0}\int_0^{x_0} 2\pi x d(x)dx = \frac{1}{3}d_p, \tag{6.2.4}$$

where $A_0 = \pi {x_0}^2$ is the plate area. Therefore the RAMD of a circular plate is

$$RAMD_c = \frac{1}{3}. \tag{6.2.5}$$

The RMS displacement d_{rms} can be derived to be

$$d_{rms} = \sqrt{\frac{1}{A_0}\int_0^{x_0} 2\pi x d^2(x) dx} = \frac{1}{\sqrt{5}} d_p. \tag{6.2.6}$$

Therefore, the ratio of RMS-to-maximum displacement (RRMD) is equal to $1/\sqrt{5}$. The relationship between d_{rms} and d_a yields

$$d_{rms} = \frac{3\sqrt{5}}{5} d_a. \tag{6.2.7}$$

The natural resonance frequency of a clamped circular plate is equal to [69]

$$\omega_{c0} = \frac{10.22}{x_0{}^2}\sqrt{\frac{D_0}{\rho_0(h_0+t_{i0})}}, \tag{6.2.8}$$

where ρ_0 is the average density of the plate.

The lumped spring constant is defined as

$$k_{01} = \frac{A_0 P}{d_a} = \frac{192\pi D_0}{x_0{}^2}. \tag{6.2.9}$$

The lumped mass is equal to

$$m_c = 1.84 m_{c0}, \tag{6.2.10}$$

where $m_{c0} = \pi x_0{}^2 \rho_0 (h_0 + t_{i0})$ is the actual mass of the plate. The effective cavity depth is defined as

$$g_{c0} = g_{00} + \frac{t_{i0}}{\varepsilon_i}, \tag{6.2.11}$$

where ε_i is the relative permittivity of the insulating layer. Defining the permittivity of vacuum as ε_0, the capacitance between the top and bottom electrodes can be derived to be

$$C_{ce} = \int_0^{x_0} \frac{2\pi x \varepsilon_0}{g_{c0} - d(x)} dx = \frac{\varepsilon_0 A_0 \ln\left(\frac{1+\sqrt{3d_a / g_{c0}}}{1-\sqrt{3d_a / g_{c0}}} \right)}{2\sqrt{3d_a g_{c0}}}. \tag{6.2.12}$$

When both DC bias and atmospheric pressure are considered, the static equilibrium equation yields

$$k_{01} d_a - \frac{1}{2} V_{DC}^2 \frac{dC_{ce}}{dd_a} - A_0 P_{atm} = 0. \tag{6.2.13}$$

By Taylor expanding dC_{ce} / dd_a at static displacement $d_a = d_0$, we can write Eq (6.2.13) as

$$k_{02} d_a - A_0 P_{atm} - \frac{1}{2} V_{DC}^2 \left(\frac{5\varepsilon_0 A_0 g_{c0} - 21\varepsilon_0 A_0 d_0}{4d_0 (g_{c0} - 3d_0)^2} - \frac{5C_{ce}(d_0)}{4d_0} \right) = 0, \tag{6.2.14}$$

where k_{02} is the effective spring constant and equal to

$$k_{02} = k_{01} - \frac{1}{2} V_{DC}^2 \left(\frac{15\varepsilon_0 A_0 d_0 - 3\varepsilon_0 A_0 g_{c0}}{4{d_0}^2 (g_{c0} - 3d_0)^2} + \frac{3C_{ce}(d_0)}{4{d_0}^2} \right). \tag{6.2.15}$$

The collapse voltage V_{pi} and its corresponding average displacement can be obtained by solving Eq (6.2.15) at $k_{02} = 0$.

Defining $V_{AC} = \bar{V}_{AC} \sin(\omega_{ac} t)$, the amplitude of the acoustic pressure generated at the plate surface can be expressed as

$$P_s = Z_{air} \dot{D}_{rms\_ac} = Z_{air} \omega_{ac} D_{rms\_ac}, \tag{6.2.16}$$

where $\dot{D}_{rms\_ac}$ and D_{rms_ac} are the amplitudes of RMS dynamic velocity and displacement, respectively. Z_{air} denotes the amplitude of air acoustic impedance. The RMS power density at the plate surface can be written as

$$P_{ower} = Z_{air} \dot{D}_{rms\_ac}^2 = \frac{P_s^2}{Z_{air}}, \tag{6.2.17}$$

Considering that the frequency of interest for most air-coupled ultrasonic applications is several hundred kHz, and the sizes of air-coupled CMUT cells are typically larger than the wavelength, the acoustic impedance is simplified as plane wave impedance [27][68]

$$Z_{air} \approx \rho_{air} c_{air}, \tag{6.2.18}$$

where ρ_{air} and c_{air} are the air density and sound speed in air, respectively. Defining *t* as the time variable and d_{a_ac} as the average dynamic displacement, the dynamic equation can be expressed as

$$\begin{aligned} & m_c \frac{d^2 d_{a\_ac}}{dt^2} + A_0 Z_{air} \frac{3\sqrt{5}}{5} \frac{dd_{a\_ac}}{dt} + \left(k_{01} - \frac{1}{2} V_{DC}^2 \left(\frac{15\varepsilon_0 A_0 d_0 - 3\varepsilon_0 A_0 g_{c0}}{4{d_0}^2 (g_{c0} - 3d_0)^2} + \frac{3C_{ce}(d_0)}{4{d_0}^2} \right) \right) d_{a\_ac} \\ & = V_{DC} \bar{V}_{AC} \left(\frac{\varepsilon_0 A_0}{2d_0 (g_{c0} - 3d_0)} - \frac{C_{ce}(d_0)}{2d_0} \right) \sin(\omega_{ac} t). \end{aligned} \tag{6.2.19}$$

The steady-state solution of Eq (6.2.19) has the following form

$$d_{ac} = D_{ac} \sin(\omega_{ac} t - \varphi_0), \tag{6.2.20}$$

where,

$$\begin{aligned} & D_{ac} = \frac{D_1}{k_{02}} \frac{1}{\sqrt{(1 - {\lambda_0}^2)^2 + (2\xi_{0\_dc} \lambda_0)^2}}, \\ & D_1 = V_{DC} \bar{V}_{AC} \left(\frac{\varepsilon_0 A_0}{2d_0 (g_{c0} - 3d_0)} - \frac{C_{ce}(d_0)}{2d_0} \right), \\ & \lambda_0 = \frac{\omega_{ac}}{\omega_{0\_dc}}, \\ & \xi_{0\_dc} = \frac{3\sqrt{5} Z_{air} A_0}{10\sqrt{k_{02} m_c}}, \\ & \varphi_0 = \tan^{-1}\left(\frac{2\xi_{0\_dc} \lambda_0}{1 - {\lambda_0}^2}\right). \end{aligned} \tag{6.2.21}$$

In Eq (6.2.21), D_{ac} represents the amplitude of the average dynamic displacement, ω_{0_dc} is the resonance frequency and equal to $\sqrt{k_{02} / m_c}$, and ξ_{0_dc} stands for the damping coefficient at DC bias. The maximum amplitude of dynamic displacement can be derived to be

$$D_{ac} = \frac{D_1}{k_{02}} \frac{1}{2\xi_{0\_dc} \sqrt{1 - \xi_{0\_dc}^2}}. \tag{6.2.22}$$

Substituting Eq (6.2.22) into Eq (6.2.16), the surface output pressure can be achieved as

$$P_s = \frac{D_1}{A_0}\sqrt{\frac{20k_{02}m_c - 18Z_{air}^2 A_0^{\ 2}}{20k_{02}m_c - 9Z_{air}^2 A_0^{\ 2}}}. \tag{6.2.23}$$

6.2.2 Annular Cell

The displacement of a clamped annular plate under *P* has the form of

$$u(r) = \frac{P(r-a)^2(r-b)^2}{24D}, \tag{6.2.24}$$

where *D* represents the flexural rigidity. Due to the laminate plate structure, it should also be calculated based on [98]. From Eq (6.2.24), the maximum static displacement is equal to

$$u_p = u\left(\frac{(a+b)}{2}\right) = \frac{P(b-a)^4}{384D}. \tag{6.2.25}$$

The average displacement of a clamped annular cell is defined as

$$u_a = \frac{1}{A}\int_a^b 2\pi r u(r)dr = \frac{8}{15}u_p, \tag{6.2.26}$$

where *A* represents the area of the annular plate. From Eq (6.2.26), the RAMD is equal to 8/15. Since the RMS displacement is defined as

$$u_{rms} = \sqrt{\frac{1}{A}\int_a^b 2\pi r u^2(r)dr} = \frac{8\sqrt{70}}{105}u_p. \tag{6.2.27}$$

the RRMD of an annular plate yields $8\sqrt{70}/105$. Based on Eqs (6.2.26) and (6.2.27), the relation between u_{rms} and u_a obeys

$$u_{rms} \approx 1.2u_a. \tag{6.2.28}$$

Defining the radio of inner to outer radius as $\tau = a/b$, the natural resonance frequency can be expressed as

$$\omega_0 = \sqrt{\frac{D}{\rho(h+t_i)b^4}}\left(\frac{478.1}{\tau^2 - 102.8\tau + 101.8}\right)^2, \tag{6.2.29}$$

where ρ is the average density of the annular plate.

The lumped spring constant and mass are equal to

$$k_1 = \frac{AP}{u_a} = \frac{720\pi D}{b^2} \frac{(1+\tau)}{(1-\tau)^3} \tag{6.2.30}$$

and

$$m = \frac{720(\tau^2 - 102.8\tau + 101.8)^4}{478.1^4 (1-\tau)^4} m_0, \tag{6.2.31}$$

respectively. Here, $m_0 = \rho\pi b^2 (h + t_i)(1-\tau^2)$ is the actual mass of the annular plate. The effective cavity depth is defined as

$$g = g_0 + \frac{t_i}{\varepsilon_i}, \tag{6.2.32}$$

The capacitance between the top and bottom electrodes can be expressed as

$$\begin{aligned} C_e &= \int_a^b \frac{2\pi r \varepsilon_0}{g - u(r)} dr \\ &= \frac{(b^2 - a^2)\pi\varepsilon_0}{2\sqrt{g}} \cdot \left(\frac{\arctan\left(\dfrac{\sqrt{15u_a/2}}{2\sqrt{\sqrt{15gu_a/8} - 15u_a/8}} \right)}{\sqrt{\sqrt{15gu_a/8} - 15u_a/8}} + \frac{\operatorname{arctanh}\left(\dfrac{\sqrt{15u_a/2}}{2\sqrt{\sqrt{15gu_a/8} + 15u_a/8}} \right)}{\sqrt{\sqrt{15gu_a/8} + 15u_a/8}} \right). \end{aligned} \tag{6.2.33}$$

The equilibrium equation under ATM and at DC bias is

$$k_1 u_a - \frac{1}{2} V_{DC}^2 \frac{dC_e}{du_a} - AP_{atm} = 0. \tag{6.2.34}$$

Assuming the solution of Eq (6.2.34) as $u_a = u_0$ and the average dynamic displacement as u_{ac}, the dynamic equation can be expressed as follow

$$m \frac{d^2 u_{ac}}{dt^2} + k_2 u_{ac} + 1.2AZ_{air} \frac{du_{ac}}{dt} = V_{DC} V_{AC} \left. \frac{dC_e}{du_a} \right|_{u_a = u_0}, \tag{6.2.35}$$

where k_2 is the effective spring constant and equal to

$$k_2 = k_1 - \frac{1}{2}V_{DC}^2 \left.\frac{d^2C_e}{du_a{}^2}\right|_{u_a=u_0}. \tag{6.2.36}$$

Similar to Eq (6.2.20), the steady-state solution of Eq (6.2.35) also has the form of

$$u_{ac} = U_{ac}\sin(\omega_{ac}t - \varphi), \tag{6.2.37}$$

where U_{ac} is the amplitude of average dynamic displacement and can be calculated based on

$$\begin{aligned} U_{ac} &= \frac{U_1}{k_2}\frac{1}{\sqrt{(1-\lambda^2)^2 + (2\xi_{dc}\lambda)^2}}, \\ U_1 &= V_{DC}\bar{V}_{AC}\frac{dC_e}{du_a}, \\ \xi_{dc} &= \frac{0.6Z_{air}A}{\sqrt{k_2 m}}, \\ \lambda &= \frac{\omega_{ac}}{\omega_{dc}}, \\ \varphi &= \tan^{-1}(\frac{2\xi_{dc}\lambda}{1-\lambda^2}). \end{aligned} \tag{6.2.38}$$

Here, $\omega_{dc} = \sqrt{k_2 / m}$ and ξ_{dc} are the resonance frequency and damping coefficient at DC bias, respectively. Based on Eq (6.2.16), the amplitude of output pressure at the plate surface is derived to be

$$P_s = \frac{U_1}{A}\sqrt{\frac{mk_2 - 0.72Z_{air}^2A^2}{mk_2 - 0.36Z_{air}^2A^2}}. \tag{6.2.39}$$

6.3 Design Optimization Flow chart

Based on the lumped models, a design optimization flow chart (Fig. 6.3.1), which involves the three optimization schemes, is built to facilitate analytical optimization of both circular and annular air-coupled CMUT cells. For simplicity, only the parameters and variables of circular cells ae listed. The variables and parameters associated with annular cells which are written in brackets.

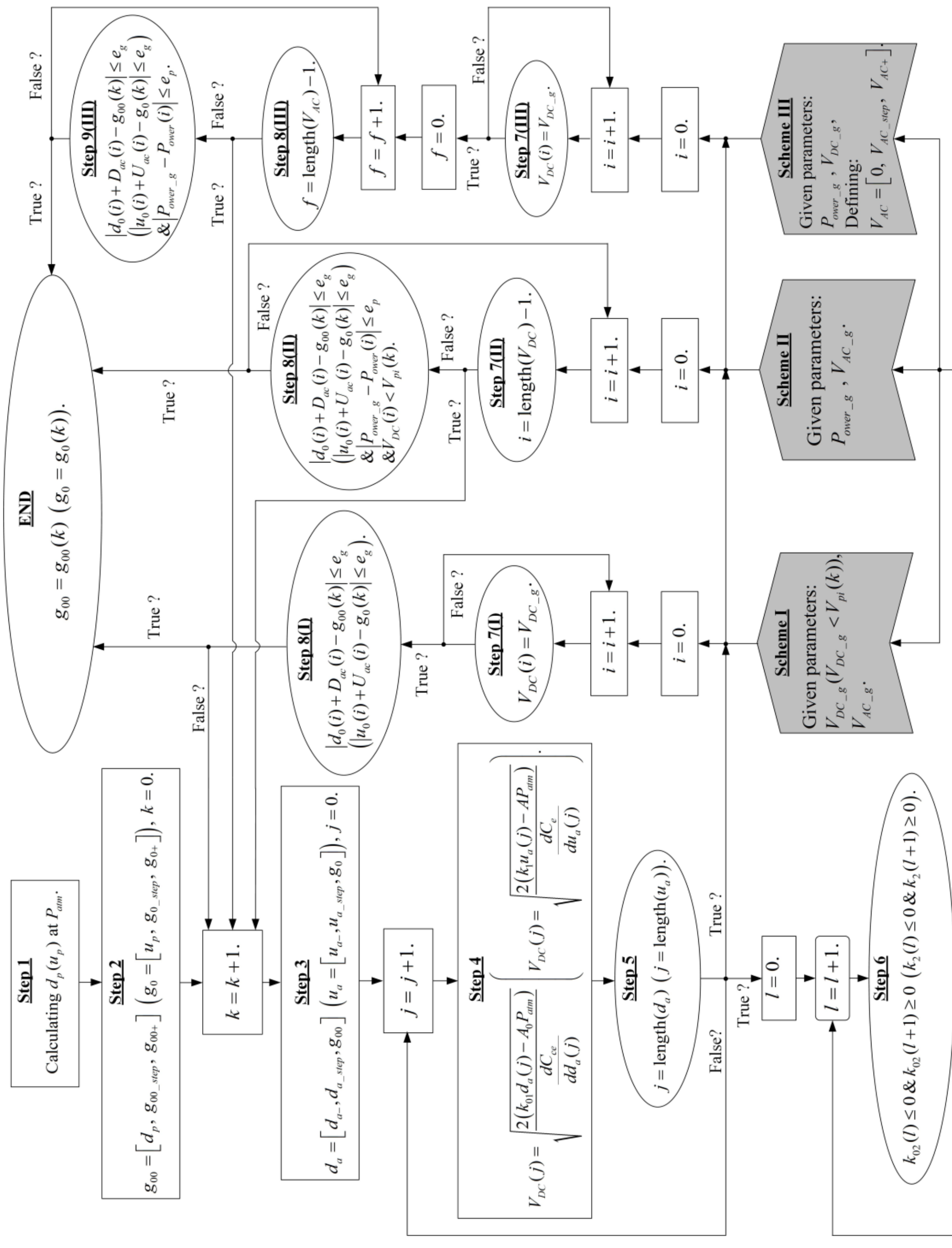

Figure. 6.3.1 Design optimization flow chart

According to Fig. 6.3.1, the first step of optimization is to calculate the maximum plate displacement d_p (u_p) under P_{atm} using Eq (6.2.3) (Eq (6.2.25)). d_p (u_p) is then set as the initial cavity depth in the optimization loop starting from Step 2, where g_{00_step} (g_{0_step}) and

$g_{00+}(g_{0+})$ represent the searching step length and termination value, respectively. Step 3 is used to define the searching range of the average displacement in the *k*-th optimization loop of cavity depth. The searching step length is denoted by d_{a_step} (u_{a_step}). The DC bias $V_{DC}(j)$, which corresponds to the average displacement $d_a(j)$ $\left(u_a(j)\right)$, is calculated based on Eq (6.2.13) (Eq (6.2.34)) in Step 4. Step 5 is used to create a DC bias series for all the discrete average displacement values in the *k*-th cavity depth optimization loop. The collapse voltage $V_{pi}(k)$ is calculated based on the criterion illustrated in Step 6, which defines that the effective spring constant k_{02} (k_2) decreases from a positive to a negative value when the cell plate collapses.

The definitions of Schemes I to III are described in the three solid blocks, where V_{DC_g} represents the given DC bias, V_{AC_g} denotes the given AC excitation voltage, and the predefined surface power density is defined as P_{ower_g}. A searching series of V_{AC} is created with 0 V as the initial value, V_{AC_step} as the step length, and V_{AC+} as the maximum value. Step 7(I) is used to locate the index *i* where $V_{DC}(i) = V_{DC\_g}$. Step 8(I) is used to estimate the absolute error of the calculated cavity depth. If the error is within the tolerance e_g, the optimization loop will terminate, else a new optimization loop will start. Based on the criteria illustrated in Step 8(II), Step 7(II) is used to terminate the *k*-th optimization loop of cavity depth. The absolute error between the given and calculated surface power density is controlled by e_p. Step 7(III) is used to find the index *i* where $V_{DC}(i) = V_{DC\_g}$. Step 8(III) is used to terminate the *k*-th optimization loop of cavity depth if the criteria shown in Step 9(III) are not satisfied.

In this study, the proposed optimization flow chart was implemented using a customized program in MATLAB (The MathWorks, Inc). The values of g_{0_step}, g_{00_step}, e_g, and e_p were chosen to be 10 nm, 10 nm, 10 nm, and 0.01W/m^2, respectively. Even though smaller values of these parameters can help increase the accuracy, a longer calculation time will also be consumed.

6.4 Experimental Verification

To investigate the effectiveness of the stated optimization principle, circular and annular CMUT cells with a common 97-kHz natural resonance frequency were fabricated based on the process introduced in Chapter 5 and used to perform transmit tests. The design dimensions are summarized in Table. 6.4.1.

Table. 6.4.1 Design dimensions.

Radius, circular cell (μm)	911
Inner radius, annular cell (μm)	1150
Outer radius, annular cell (μm)	2500
Plate thickness (μm)	19.2
Insulating layer thickness (μm)	1.6
Cavity depth (μm)	11.8

The CMUT plates, which were provided by SOI wafers, are made of single-crystal silicon (simplified as an isotropic material) with orientation of <111> and resistivity of 0.001 Ω·cm. A layer of silicon dioxide, which serves as the insulating layer, was wet thermally grown on the top of the SOI device layer before wafer bonding. The substrate wafer is made of 500-μm single-crystal silicon with resistivity of 0.001 Ω·cm and orientation of <100>. As both types of cells were fabricated in one die, they share the same plate thickness, insulating layer thickness, and cavity depth.

Photographs of the fabricated CMUT cells are shown in Fig. 6.4.1, where the circular- and annular-shape shadows indicate the plate deformation due to atmospheric pressure. The triangular metal pads located in the corners are the top electrodes. They were directly deposited on the conductive silicon plate layer. The highly conductive silicon substrate itself was used as the bottom electrode.

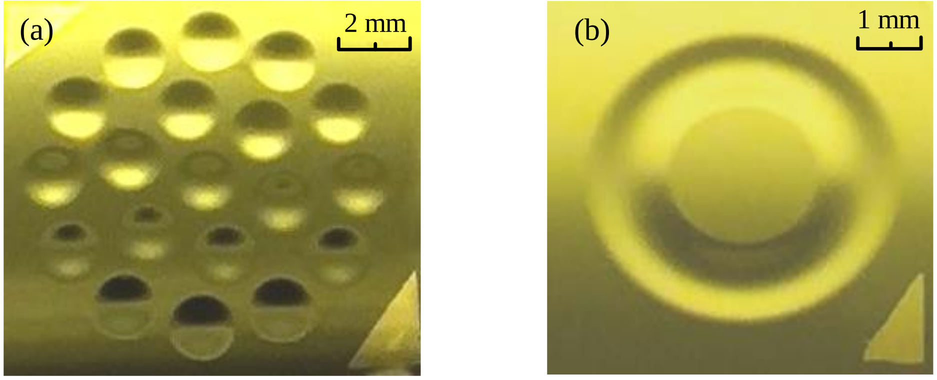

Figure. 6.4.1 Photographs of the fabricated devices: (a) Circular cells. (b) An annular cell.

A profilometer (Dektak 8 Stylus Profiler, Bruker Corp) was used to measure the static displacement of the CMUT plates under atmospheric pressure. The measured and calculated results are illustrated in Fig. 6.4.2.

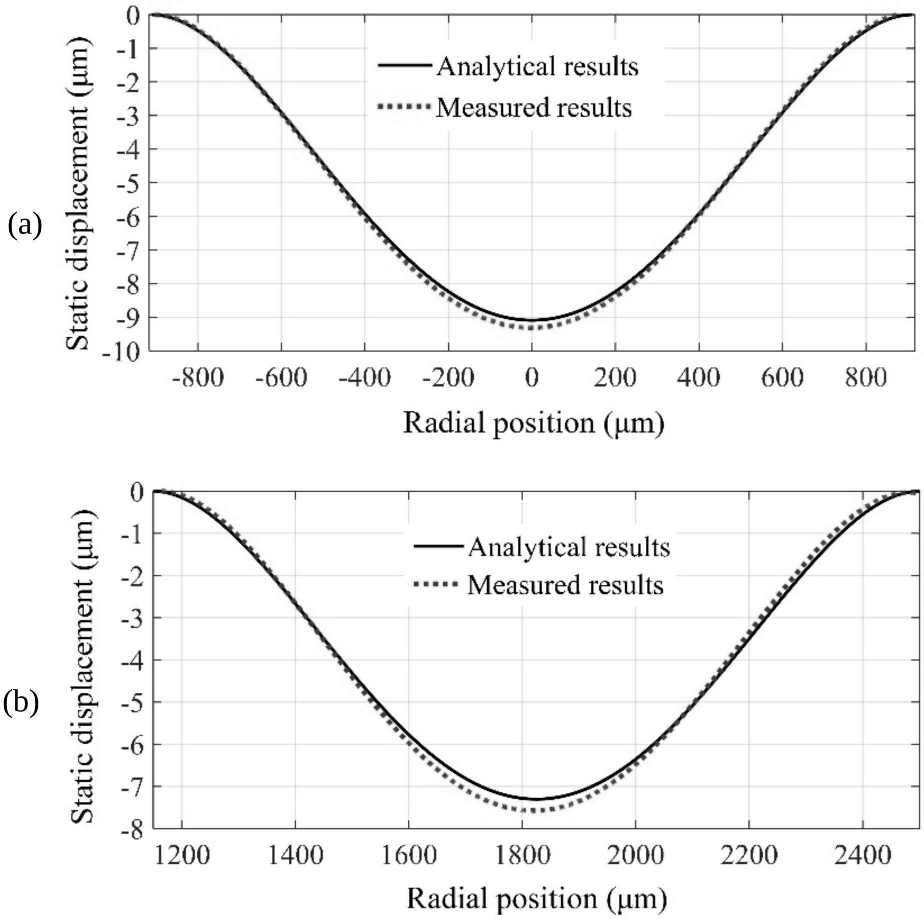

Figure. 6.4.2 Static displacement of the CMUT plates under ATM: (a) Circular CMUT cell. (b) Annular CMUT cell.

We note that for both types of cells, the measured maximum static displacement is slightly smaller than the analytical displacement. One possible explanation is that the actual plate thickness is smaller than 19.2 µm, which was calculated based on the specified value provided by the manufacturer. In Fig. 6.4.2 (b), it can be found that the measured maximum displacement of the annular plate is located at the left of the center radius position (1825 µm), where the maximum analytical displacement is. This is due to the fact that the established annular plate model assumed the deformation to be symmetrical about the center line as indicated in Eq (6.2.24). Overall, the measured results match well with the calculated ones.

To evaluate the dynamic performance of the CMUTs, a DC power source (GPR-30H10D, Good Will Instrument Co., Ltd) was used to provide a DC bias, and a signal amplifier (Model 9400, Tabor Electronics Ltd) was used to amplify the output sinusoidal signal from a function generator (4040B, B&K Precision Corp) to drive the CMUTs at different frequencies in continuous mode. A laser Doppler vibrometer (OFV-5000, Polytec Inc) was used to measure the frequency response of the maximum dynamic displacement to find the resonance frequency and its relative maximum dynamic displacement. Fig. 6.4.3 shows the measured and calculated minimum AC voltages required for maximizing the dynamic displacement at different DC biases. An approximately linear relationship between the DC bias and AC excitation voltage can be found. It is also shown that a higher DC bias requires a lower AC excitation voltage to maximize the dynamic displacement. The maximum dynamic displacement and resonance frequencies corresponding to Fig. 6.4.3 are illustrated in Figs. 6.4.4 and 6.4.5, respectively. Fig. 6.4.4 demonstrates that a higher DC bias leads to a smaller maximum dynamic displacement. This can be explained by the fact that a higher DC bias results in an increased static displacement, which in turn squeezes the active volume in the cavity. In Fig. 6.4.5, the spring softening effect, i.e., a higher DC bias leads to a lower resonance frequency, can be observed.

Figs. 6.4.3 to 6.4.5 show that the measured results are overestimated by the calculation. This is also possibly due to the underestimated plate thickness which leads to a larger static displacement, a lower resonance frequency, a smaller active volume in the cavity, and a higher electrical field between electrodes. A higher electric field reduces the requirement of AC excitation voltage for a maximum dynamic displacement (Fig. 6.4.3). A smaller active volume reduces the maximum dynamic displacement (Fig. 6.4.4). Since the electrostatic force is inversely proportional to the square of the distance between the electrodes, a larger spring softening effect can be found at a higher DC bias (Fig. 6.4.5). Nevertheless, the trends of the calculated results overall agree with those of the measured results. This validates the effectiveness of the optimization principle and accuracy of the lumped models.

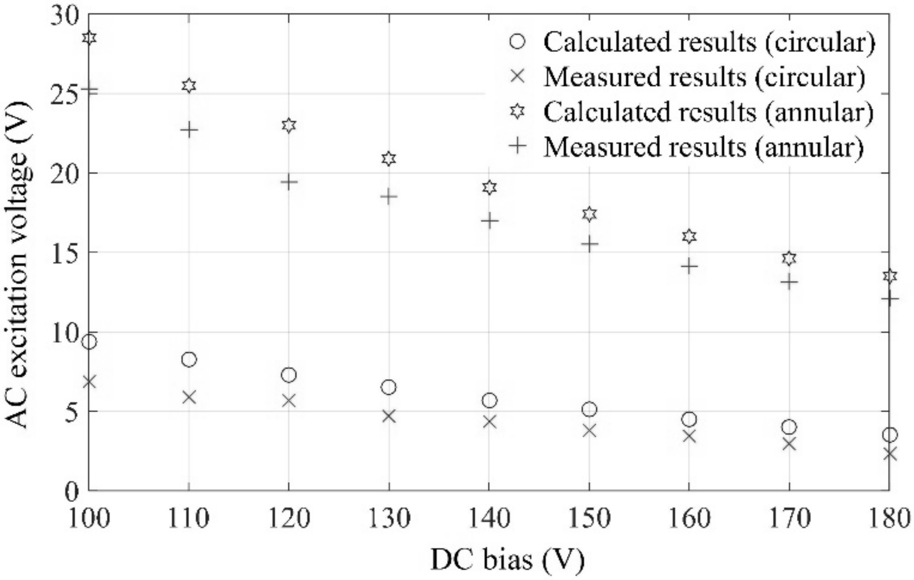

Figure. 6.4.3 Optimized AC voltages at different DC biases.

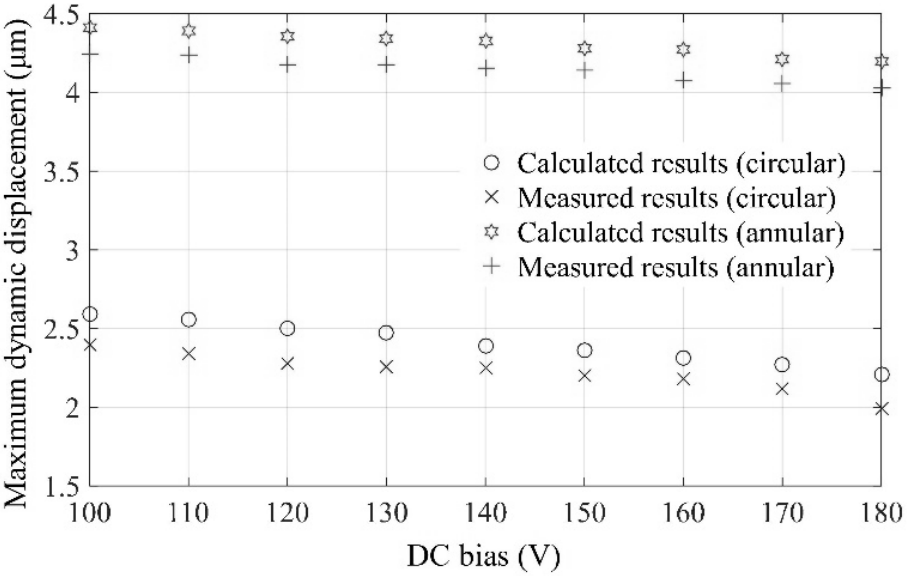

Figure. 6.4.4 Maximum dynamic displacement at different DC biases.

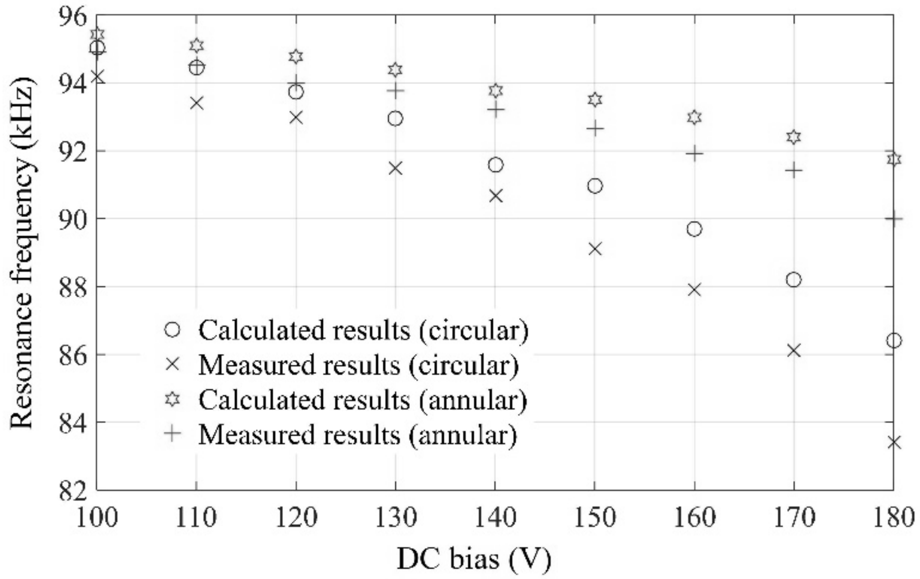

Figure. 6.4.5 Resonance frequencies at different DC biases.

6.5 Comparison of circular and annular cells.

A comparative study is performed on optimizing both of the annular and circular cells in parallel. For simplicity, both types of cells were designed with 20-μm single-crystal silicon plates and 1.5-μm wet thermally grown silicon dioxide insulating layer. The radius dimensions are listed in Table. 6.5.1.

Table. 6.5.1 Radius dimensions of the CMUT cells.

Resonance frequency (kHz)	100	200	300
Radius, circular cell (μm)	918	649	530
Inner radius, annular cell (μm)	648	1000	1200
Outer radius, annular cell (μm)	2000	2000	2000

6.5.1 Scheme I

Scheme I is suitable for optimizing CMUT cells when there exists limits on the amplitudes of DC bias and AC excitation voltage. These limits may result from the dielectric breakdown voltage of the device, difficulties in achieving high-voltage pulsers or integrating them into the driving circuits, and certain safety requirements. Based on the optimization flow chart of Scheme I, the cavity depth of both circular and annular cells was optimized for the maximum surface RMS power density. To reduce the complexity, the AC voltage was fixed at 40 Vpp, and the DC bias was increased from 100 V to 300 V to represent different DC-to-AC ratios. The power density of the optimized CMUT cells at different DC biases is shown in Fig. 6.5.1. It indicates that both a higher DC bias and a higher resonance frequency will lead to a higher power density. This is reasonable because the power density is proportional to the square of both frequency and RMS dynamic displacement (Eq (6.2.17)). The power density is approximately a linear function of the DC bias at a certain frequency, but has a larger slope at a higher frequency. On average, the power density of the annular cells is double that of circular cells when the same DC bias and AC excitation voltage are applied.

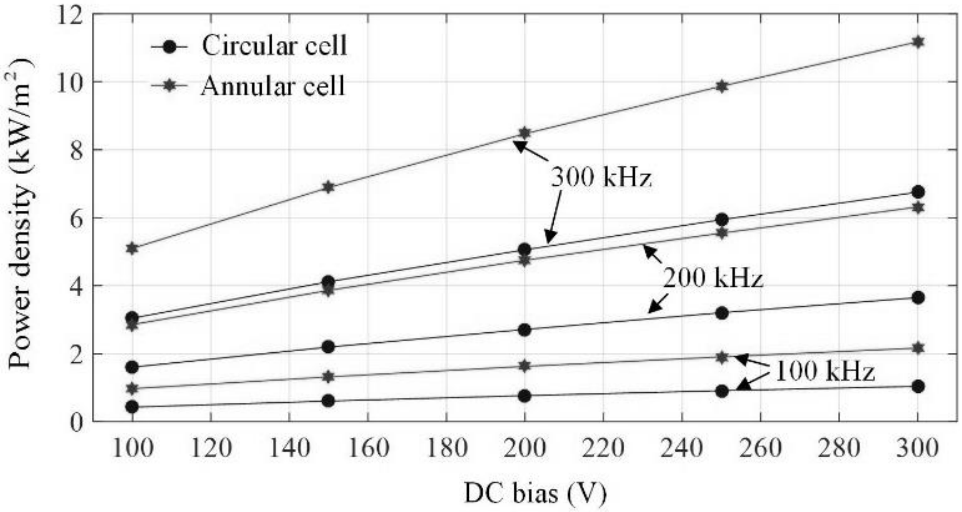

Figure. 6.5.1 Calculated maximum output power density at the plate surface.

Table. 6.5.2 lists the resonance frequencies, static and dynamic displacement, pull-in voltages, and optimized cavity depth at 100- and 300-V DC bias. It is noted that the frequencies at DC biases and collapse voltages of the annular cells are lower than those of the circular cells. This means that the optimized annular cells have a greater spring softening effect. It can also be found that the smaller static displacement of the annular plates under ATM leads to smaller optimized cavity depth. On the other hand, even though both types of cells have similar maximum dynamic displacement, the higher RRMD of annular cells enables them to generate a higher acoustic power.

Table. 6.5.2 Calculated optimization results of circular and annular cells for Scheme I.

Nat. freq. (kHz)	100	100	200	200	300	300
DC bias (V)	100	300	100	300	100	300
Circular cell						
Freq. at DC (kHz)	98.73	96.19	198.64	195.98	298.59	295.94
Collapse volt. (V)	336.43	604.43	464.46	811.65	566.60	982.86
Opt. cavity depth (μm)	12.12	14.66	5.66	7.65	4.19	5.91
Max. static disp. at ATM (μm)	8.37	8.37	2.09	2.09	0.93	0.93
Max. static disp. at DC (μm)	8.45	8.77	2.13	2.28	0.96	1.04
Max. dynamic disp. (μm)	3.69	5.91	3.54	5.43	3.24	4.89
Annular cell						
Freq. at DC (kHz)	98.13	94.26	198.16	194.29	298.18	294.34
Collapse volt. (V)	283.58	519.75	397.42	700.40	486.20	847.12
Opt. cavity depth (μm)	10.51	12.92	5.01	6.82	3.71	5.26
Max. static disp. at ATM (μm)	6.58	6.58	1.66	1.66	0.74	0.74
Max. static disp. at DC (μm)	6.68	7.04	1.70	1.86	0.77	0.86
Max. dynamic disp. (μm)	3.90	6.06	3.32	5.03	2.94	4.41

6.5.2 Scheme II

In Scheme II, the cavity depth was optimized at a given AC excitation voltage (40 Vpp) such that a predefined RMS power density could be achieved by applying the minimum DC bias. Table. 6.5.3 summarizes the optimization results of circular and annular cells with different natural frequencies and output power density. In Fig. 6.5.2, the minimum DC biases required for different power density are shown. Combining Table. 6.5.3 and Fig. 6.5.2, it can be seen that the minimum DC biases of annular cells are, on average, half those of the circular cells. It is also shown that a higher DC bias leads to a greater spring softening effect. With the increase of power density, the required minimum DC bias increases at a larger slope at lower frequencies. The collapse voltages of the optimized annular cells are around half those of the circular cells.

Table. 6.5.3 Calculated optimization results of circular and annular cells for Scheme II.

Nat. freq. (kHz)	100	100	200	200	300	300
Power density (kW/m^2)	0.8	1.2	2.0	4.0	5.0	7.0
Circular cell						
Freq. at DC (kHz)	97.3	95.40	198.19	195.38	297.31	295.71
Collapse volt. (V)	502.48	674.09	541.08	882.6	797.57	1014.86
Opt. cavity depth (μm)	13.74	15.27	6.13	8.02	5.18	6.03
Max. static disp. at ATM (μm)	8.37	8.37	2.09	2.09	0.93	0.93
Max. static disp. at DC (μm)	8.62	8.89	2.16	2.32	0.99	1.05
Max. dynamic disp. (μm)	5.10	6.36	3.96	5.70	4.17	4.98
Annular cell						
Freq. at DC (kHz)	98.54	97.49	198.87	197.04	298.20	297.13
Collapse volt. (V)	254.90	336.71	317.47	503.18	493.32	607.57
Opt. cavity depth (μm)	10.18	11.09	4.46	5.68	3.74	4.26
Max. static disp. at ATM (μm)	6.58	6.58	1.66	1.66	0.74	0.74
Max. static disp. at DC (μm)	6.65	6.73	1.68	1.74	0.77	0.79
Max. dynamic disp. (μm)	3.52	4.35	2.76	3.94	2.91	3.45

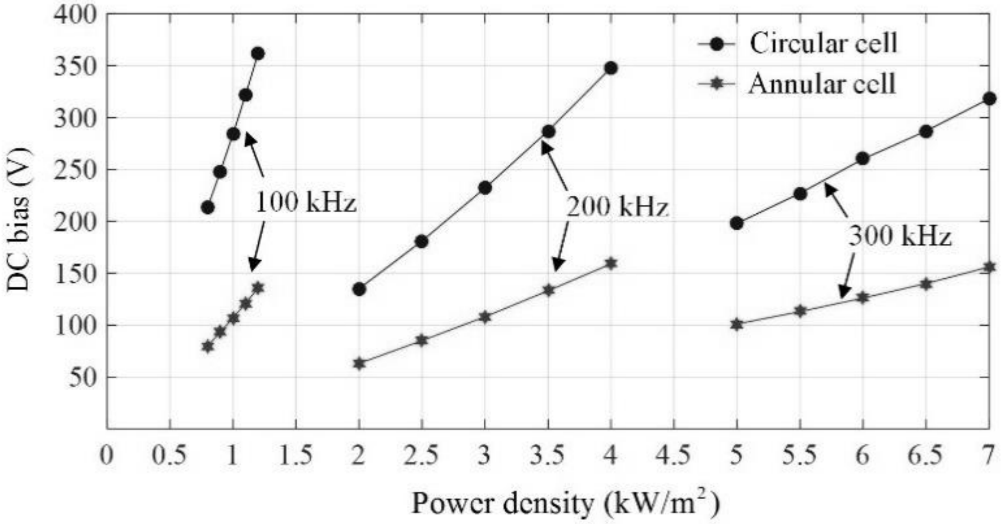

Figure. 6.5.2 Calculated minimum DC biases required for different surface output power density.

Scheme II can be used to optimize CMUT cells when there is an upper limit on the AC excitation voltage and minimum requirement on the amplitude of surface power density. Since the minimum DC bias required by an annular cell is half that of a circular cell, an annular cell holds a higher sensitivity in transmitting ultrasound and allows a lower breakdown voltage.

6.5.3 Scheme III

Scheme III is designed for optimizing the cavity depth to minimize the AC excitation voltage required by a predefined RMS power density at a given DC bias. In this section, a lower power density was predefined at a lower frequency to make the calculated AC voltages comparable at different frequencies. The resonance frequencies at DC bias, static and dynamic average displacement, collapse voltages, and optimized cavity depth are summarized in Table. 6.5.4. It can be found that the optimized annular cells show a greater spring softening effect, which is similar to Scheme I.

Table. 6.5.4 Calculated optimization results of circular and annular cells for Scheme III.

Nat. freq. (kHz)	100	100	200	200	300	300
Power density (kW/m^2)	0.8	0.8	2.5	2.5	5.0	5.0
DC bias (V)	100	300	100	300	100	300
Circular cells						
Freq. at DC (kHz)	99.34	95.03	199.20	193.86	299.19	294.44
Collapse volt. (V)	469.36	540.58	616.51	667.46	780.44	844.69
Opt. cavity depth (μm)	13.43	14.09	6.58	6.87	5.11	5.37
Max. static disp. at ATM (μm)	8.37	8.37	2.09	2.09	0.93	0.93
Max. static disp. at DC (μm)	8.42	8.84	2.12	2.34	0.95	1.07
Max. dynamic disp. (μm)	4.98	5.22	4.41	4.53	4.14	4.23
Annular cells						
Freq. at DC (kHz)	97.92	85.49	197.84	184.03	298.14	285.81
Collapse volt. (V)	269.66	375.61	367.13	457.54	480.66	562.66
Opt. cavity depth (μm)	10.35	11.50	0.81	5.40	3.68	4.06
Max. static disp. at ATM (μm)	6.58	6.58	1.66	1.66	0.74	0.74
Max. static disp. at DC (μm)	6.69	7.38	1.71	2.04	0.77	0.95
Max. dynamic disp. (μm)	3.56	4.07	3.09	3.34	2.91	3.04

Figure. 6.5.3 illustrates the calculated minimum AC voltages at different predefined power

density and DC biases. We note that given the same power density and DC biases, an annular cell only needs half the AC voltages of a circular cell. Moreover, for both cell types, with the decrease of AC voltage, an increasing higher DC bias is required to maintain the same output power density. As a result, a tradeoff has to be made between a lower AC voltage and a much higher DC bias. For example, if dielectric breakdown is the main concern, a high AC and low DC should be chosen. On the other hand, if the AC power is the concern, a low AC and a reasonably high DC can be used. Figure. 6.5.3 can also be utilized to find the minimum DC bias for a given AC excitation voltage and power density. Taking the 300-kHz annular cell for instance, at 20-V AC excitation voltage, the minimum DC bias for 5-kW/m^2 power density reads 100 V, which agrees with that of Fig. 6.5.2.

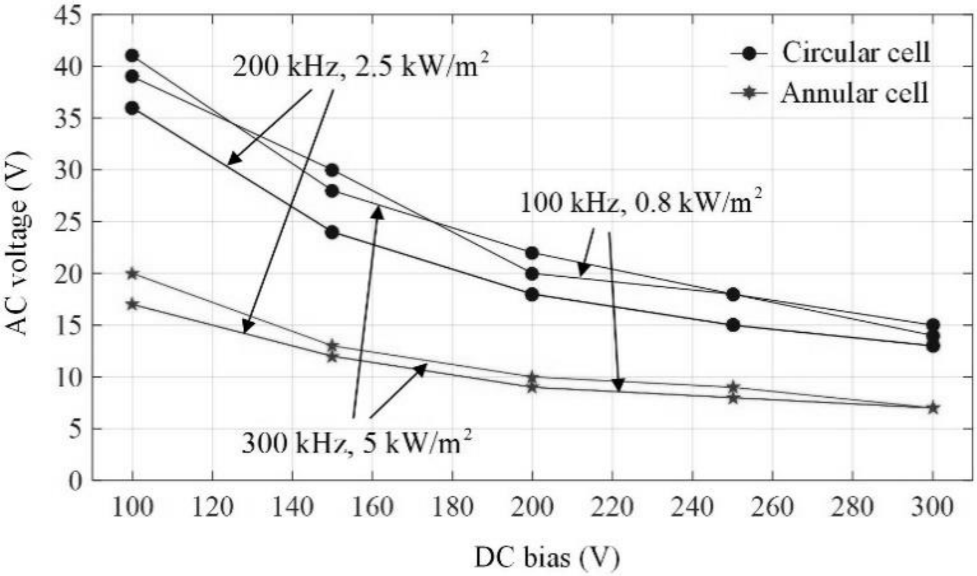

Figure. 6.5.3 Calculated minimum AC voltages required for different surface output power density.

Chapter 7 Air-coupled CMUT Array based on Concentric Annular Cell Geometry

In the previous three chapters, efforts were focused on the FEA, analytical modeling, optimization, and fabrication of a single annular CMUT cell. These fundamental studies demonstrated the feasibility of the annular cell design as well as provided important tools for analyzing and designing annular-cell CMUTs. Considering that the annular configuration allows multiple cells to be arranged in a concentric layout, which promises the highest fill factor [28], a concentric annular-cell array is promising for further enhancing the transmit power and offering depth focusing. In this chapter, a CMUT array consisting of nine concentric annular cells is presented. The lumped element model was adopted to design the cells and predict their performance. The CMUT was fabricated based on the wafer bonding technique [46]. A novel pillar-free etching process was developed to create the deep large-area cell cavities, and a fabrication process modified for enhancing the electroconductivity of the electrical leads in the isolation trenches is discussed. Each cell of the fabricated CMUT array was characterized for both the static and dynamic performances. The cross-talk and plate-cracking phenomenon of the fabricated CMUT were investigated, and relative suggestions are provided for design improvement.

7.1 Design

The proposed concentric annular-cell CMUT array was designed with a natural resonance frequency of 200 kHz, which was chosen as a tradeoff between being high enough to produce a reasonably narrow acoustic beam and sufficiently low to avoid excessive attenuation in air. The aperture size of the array was designed based on the chosen frequency (200 kHz) and the desired natural focal distance (z) using Eq (2.1.5)

$$a = \sqrt{\frac{zc}{f}}, \tag{7.1.1}$$

where a, f, and c denote the aperture radius, natural resonance frequency, and sound speed in air, respectively. Since acoustic focusing is performed within the near field, z should be large enough to allow a practical working distance and sufficiently small to avoid an oversized aperture. In this thesis, z was chosen as 6 cm, which results in an aperture radius of about 1 cm. This preliminarily designed aperture size will be later used to determine the number of cells contained in the array.

The top-view and cross-section schematics of the array are illustrated in Fig. 7.1.1. In the top view, the black dot at the center indicates the supporting post of Cell *1*, the grey annular areas represent the active plates, and the blank regions between neighbouring cells stand for the isolation trenches. From the cross-section view, the plate is a laminate structure consisting of a highly conductive silicon structural layer, an insulating layer made of wet thermal silicon dioxide (SiO_2), and a passivation layer made of plasma enhanced chemical vapor deposition (PECVD) SiO_2. A layer of wet thermal SiO_2 is designed in the post areas of the bottom wafer to increase the breakdown voltage of the device.

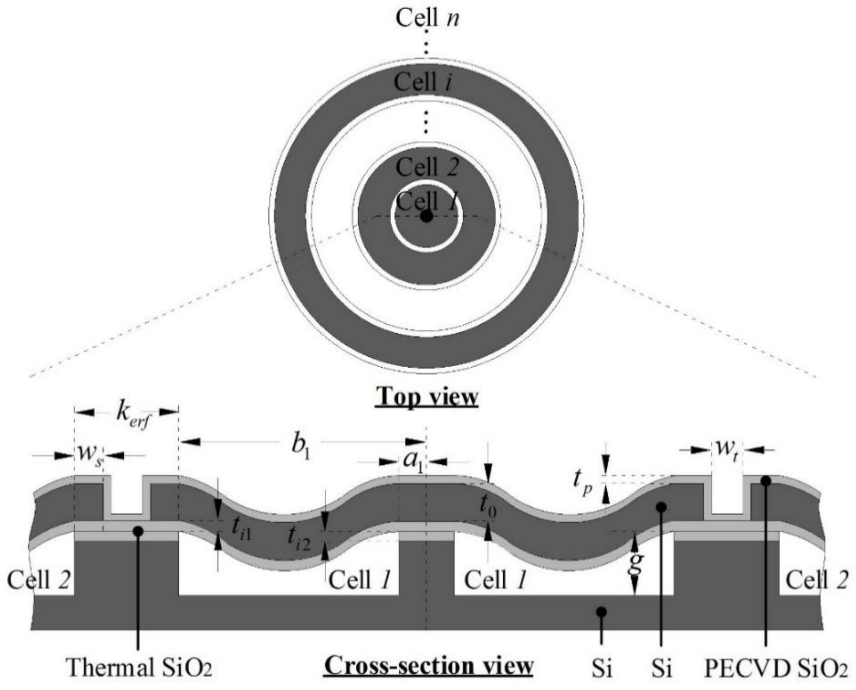

Figure. 7.1.1 Schematics of the concentric annular-cell CMUT array.

The key dimensions of the CMUT are the silicon layer thickness t_0, insulating layer thicknesses t_{i1} and t_{i2}, thickness of the passivation layer t_p, cavity depth g, cell inner radius a_i, and cell outer radius b_i. The widths of the plate supporting area and the isolation trench are defined as w_s and w_t, respectively. The cell-to-cell distance is defined as $k_{erf} = w_t + 2w_s$. Based on the availability of commercial silicon-on-insulator (SOI) wafers, the device layer was chosen to be 20 µm, which is thick enough to avoid non-linear effects of large deformation and sufficiently thin to deform at a large amplitude for a high output power. The wet thermal SiO_2 grown in our facility was measured with a dielectric strength of around 300 V/µm. The degraded dielectric strength (relative to the reported value of 950 V/µm [99]) is believed to result from two reasons: a temporary facility contamination and the large device area which likely contains more pinholes and particle contaminations. In this work, the CMUT was designed for a DC bias voltage of less than 500 V. Hence, the insulating layer was designed with a thickness of 1.9 µm, of which 0.5 µm was provided by the bottom wafer, and 1.4 µm was grown on the top wafer. The two insulating layers were different in thicknesses because they were grown in separate batches, which were shared with other wafers to save cost. Although the residual stress of the thermal SiO_2 is around 200 MPa, its contribution to the plate deformation is negligible. Taking the consumed silicon into consideration, the final thickness of the silicon structural layer can be calculated to be 19.35 µm. A passivation layer of 500 nm was chosen to ensure a good isolation between the electrical leads and the conductive plates. It was deposited using a mixed high/low-frequency system (Oxford PlasmaLab System 100 PECVD, Oxford Instruments plc) with a low film stress (-10 MPa to 15 MPa).

As developed in Chapter 5, the natural resonance frequency of the clamped laminate annular plate can be written as

$$\omega_0 = \sqrt{\frac{D}{m_0 b_i^{\,4}}}\left(\frac{478.1}{\tau^2 - 102.8\tau + 101.8}\right)^2, \tag{7.1.2}$$

where τ is the ratio of a_i to b_i, and D denotes the flexural rigidity of the plate. The plate mass is defined as $m_0 = \rho_0 t_0 + \rho_i t_{i1} + \rho_p t_p$, where ρ_0, ρ_i, and ρ_p stand for the densities of silicon, thermal SiO_2, and PECVD SiO_2, respectively. For the laminate plate, D can be calculated based on [98]

$$D = \frac{B_1 D_1 - C_1^2}{B_1},$$
$$B_1 = \frac{E_p t_p}{1-\mu_p^2} + \frac{E t_0}{1-\mu^2} + \frac{E_i t_{i1}}{1-\mu_i^2},$$
$$C_1 = \frac{E_p t_p^2}{2(1-\mu_p^2)} + \frac{E[(t_0+t_p)^2 - t_p^2]}{2(1-\mu^2)} + \frac{E_i[(t_p+t_0+t_i)^2 - (t_0+t_p)^2]}{2(1-\mu_i^2)}, \tag{7.1.3}$$
$$D_1 = \frac{E_p t_p^3}{3(1-\mu_p^2)} + \frac{E[(t_0+t_p)^3 - t_p^3]}{3(1-\mu^2)} + \frac{E_i[(t_p+t_0+t_i)^3 - (t_0+t_p)^3]}{3(1-\mu_i^2)},$$

where E_p, E, and E_i are the Young's Modulus of PECVD SiO_2, silicon, and thermal SiO_2, respectively, and μ_p, μ, and μ_i represent the corresponding Poisson's ratios of the three materials. The physical properties of the materials used in the design calculations are listed in Table. 7.1.1.

Table. 7.1.1 Physical properties of the plate materials.

Material	Si	Thermal SiO_2	PECVD SiO_2
Density (kg/m^3)	2330	2200	2300
Poisson's ratio	0.27	0.17	0.25
Young's Modulus (GPa)	169	70	85
Relative permittivity	N/A	3.9	N/A

Based on Eq (7.1.2), b_i can be derived to be

$$b_i = \frac{51a_i + cc + \sqrt{(102a_i + cc)^2 - 407.2a_i^2}}{101.8},$$
$$cc = 478.1\left[\frac{D}{\omega_0^2(\rho_0 t_0 + \rho_i t_i + \rho_p t_p)}\right]^{1/4}. \tag{7.1.4}$$

Given ω_0, t_0, and t_{i1}, a_i and b_i can be determined based on each other. In this study, the cells were designed in a sequence of *1* to *n* with the definition of a_1=150 µm, w_t=60 µm, and w_s=95 µm. These parameters were chosen to be small in order to achieve a relatively high fill factor. However, it should be mentioned that a_1 should also be sufficiently large to prevent excessive stress concentration at the center of the plate, w_s should be large enough to ensure structural strength for clamping the plate, and w_t should be reasonably large to avoid an overhigh aspect ratio of the isolation trenches. Extracting ω_0 from Eq (7.1.2) yields

$$\omega_0 = w_i(100.8 + \frac{w_i}{b_i})\sqrt{\frac{D}{(\rho_0 t_0 + \rho_i t_i + \rho_p t_p)}}, \quad (7.1.5)$$

where $w_i = b_i - a_i$ is the plate width of Cell *i*. Equation (7.1.5) indicates that ω_0 is a weak function of b_i and a strong function of w_i. Therefore, all the cells in the array should be designed with similar plate widths in order to achieve the same natural resonance frequency. According to the calculated results (Table. 7.1.2), the outer radius of Cell *9* is closest to the desired aperture radius of 1 cm, and hence the array was designed with nine cells. The fill factor is calculated to be 81%, which can be further improved by designing a smaller k_{erf}. For instance, decreasing k_{erf} from 250 µm to 150 µm will result in a fill factor of 88%. However, choosing k_{erf} should also take the fabrication feasibility and structural strength into consideration.

Table. 7.1.2 Radius dimensions of cells *1* to *9*.

Dimension	Cell *1*	Cell *2*	Cell *3*	Cell *4*	Cell *5*
a_i (µm)	150	1341.4	2537	3733.8	4931.4
b_i (µm)	1091.4	2287	3483.8	4681.4	5879.3
w_i (µm)	941.4	945.6	946.8	947.6	947.9
Dimension	Cell *6*	Cell *7*	Cell *8*	Cell *9*	
a_i (µm)	6129.3	7327.5	8525.9	9724.4	
b_i (µm)	7077.5	8275.9	9474.4	10673	
w_i (µm)	948.2	948.4	948.5	948.6	

According to Eq (5.2.3), the maximum static displacement of Cell *i* under atmospheric pressure P_{atm} has the form of

$$u_p = \frac{P_{atm} w_i^4}{384D}. \quad (7.1.6)$$

Based on Eq (7.1.6), since the nine cells have similar plate widths, their static displacements are rather consistent. The consistency of the static displacements is of significance because it allows the cells to be designed with the same cavity depth, which is more practical from the perspective of fabrication.

For the presented array, a cavity depth of 5.2 µm was designed with a predicted collapse voltage of 410 V. Based on the lumped model, the static and dynamic performance of the cells actuated by a 20-Vpp AC voltage at DC biases of 100 and 150 V are calculated and shown in Table. 7.1.3, where f_0 and f_{dc} represent the natural resonance frequency and frequency at the DC bias (V_{dc}), respectively. The collapse voltage, maximum static displacement at DC, maximum dynamic displacement at AC, root-mean-square (rms) dynamic displacement at AC, and output power density at the plate surface are denoted by V_c, u_{p_dc}, u_{p_ac}, u_{rms_ac}, and P_{ower}, respectively.

Table. 7.1.3 Calculated static and dynamic performance of Cells *1* to *9*.

Design	Cell *1*	Cell *2*	Cell *3*	Cell *4*	Cell *5*
u_p (µm)	1.65	1.68	1.69	1.69	1.69
V_c (V)	425	417	415	413	413
f_0 (kHz)	200.01	200.00	200.05	199.99	200.03
f_{dc} (kHz), V_{dc}=100 V	198.41	198.34	198.37	198.30	198.33
u_{p_dc} (µm), V_{dc}=100 V	1.69	1.72	1.73	1.73	1.74
u_{p_ac} (µm), V_{dc}=100 V	1.52	1.54	1.54	1.55	1.55
u_{rms_ac} (µm), V_{dc}=100 V	0.97	0.98	0.98	0.99	0.99
P_{ower} (kW/m^2), V_{dc}=100 V	0.60	0.62	0.62	0.62	0.62
f_{dc} (kHz), V_{dc}=150 V	196.26	196.10	196.11	196.02	196.04
u_{p_dc} (µm), V_{dc}=150 V	1.74	1.77	1.78	1.79	1.79
u_{p_ac} (µm), V_{dc}=150 V	2.35	2.39	2.39	2.40	2.40
u_{rms_ac} (µm), V_{dc}=150 V	1.50	1.52	1.52	1.53	1.53
P_{ower} (kW/m^2), V_{dc}=150 V	1.40	1.45	1.45	1.46	1.46

Design	Cell *6*	Cell *7*	Cell *8*	Cell *9*
u_p (µm)	1.70	1.70	1.70	1.70
V_c (V)	412	412	412	411
f_0 (kHz)	200.01	200.00	200.02	200.02
f_{dc} (kHz), V_{dc}=100 V	198.30	198.29	198.31	198.31
u_{p_dc} (µm), V_{dc}=100 V	1.74	1.74	1.74	1.74
u_{p_ac} (µm), V_{dc}=100 V	1.55	1.55	1.55	1.55
u_{rms_ac} (µm), V_{dc}=100 V	0.99	0.99	0.99	0.99
P_{ower} (kW/m^2), V_{dc}=100 V	0.62	0.62	0.62	0.62
f_{dc} (kHz), V_{dc}=150 V	196.01	196.00	196.01	196.00
u_{p_dc} (µm), V_{dc}=150 V	1.79	1.80	1.80	1.80
u_{p_ac} (µm), V_{dc}=150 V	2.41	2.41	2.41	2.41
u_{rms_ac} (µm), V_{dc}=150 V	1.54	1.54	1.54	1.54
P_{ower} (kW/m^2), V_{dc}=150 V	1.47	1.47	1.47	1.47

The average maximum static displacement under Patm was predicted to be 1.69 µm. The average resonance frequencies at 100 and 150-V DC biases were calculated to be 198.33 and

196.06 kHz, respectively. Therefore, the frequency shift, which results from the spring-softening effect, is about 2 kHz. The frequency spread among the nine cells at 100 and 150-V DC biases are 0.12 and 0.26 kHz, respectively. The inconsistency of the biased resonance frequencies can be reduced by designing the cells based on a predefined biased resonance frequency instead of the natural resonance frequency. The surface power densities were calculated based on the rms dynamic displacements to be 0.62 and 1.45 KW/m^2 at DC biases of 100 and 150 V, respectively. Generating a higher power requires a larger cavity depth and a higher DC bias and AC excitation voltage. The thickness and quality of the insulating layer determine the maximum voltage that the CMUT can stand before breakdown. On the other hand, a larger plate displacement may lead to non-linear elasticity [86][80]. To avoid the non-linear effects as well as increase the output power, the CMUT can be designed with a thicker plate, thicker insulating layer, and larger cavity depth.

7.2 Fabrication

A photograph of the fabricated CMUT array is shown in Fig. 7.2.1. Each cell in the array has two sets of top electrode leads and bonding pads. The bottom electrodes are located at the corners of the transducer.

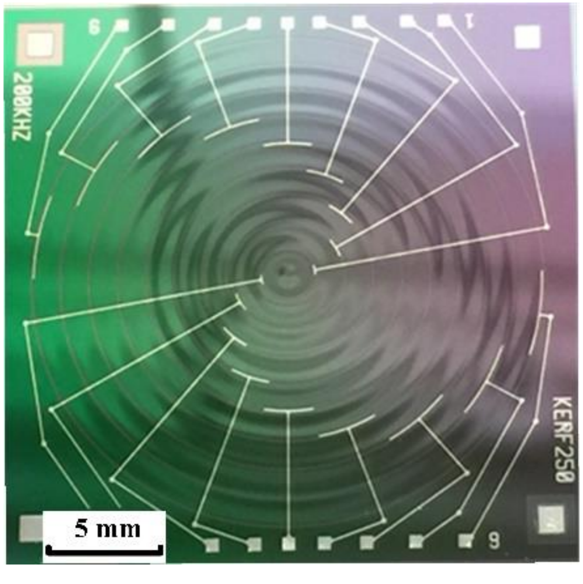

Figure. 7.2.1 A photograph of the fabricated CMUT array.

The fabrication process (Fig. 7.2.2) in this chapter was also developed based on the wafer bonding technique. It started with an SOI wafer as the top wafer and a silicon substrate as the bottom wafer. The SOI device layer, which serves as the CMUT plate, is made of 20-µm single-crystal silicon with orientation of <1 1 1> and a resistivity of 0.001 Ω·cm. The silicon substrate is 500 µm thick with a resistivity of 0.005 Ω·cm and orientation of <1 0 0>. At first, the top and bottom wafers were wet thermally grown with 1.4 and 0.5-µm SiO_2, respectively. Next, the bottom wafer was patterned with cavities, which were then etched into the silicon substrate using deep reactive ion etching (DRIE). Direct wafer bonding was performed in step 3. First, both wafers were cleaned with RCA-1 solution at 80 ˚C for 10 mins to achieve a contamination-free and hydrophilic surface. Then they were treated with oxygen plasma for 10 min to enhance the surface activity. The wafers were brought into contact with a 2500-kN compressive force right after the plasma treatment (AWB-04 aligner wafer bonder, Applied Microengineering Ltd). The direct-bonded pair was then annealed at 1100 ˚C for 2 hours to achieve a permanent covalent bonding. In step 4, a layer of polydimethylsiloxane (PDMS) (Sylgard 184, Dow Corning Inc) was cast on the bottom wafer to protect it from being attacked in the subsequent step. In step 5, buffered oxide etch (BOE) was used to expose the SOI handling silicon, which was subsequently etched away using 25% tetramethylammonium hydroxide (TMAH) solution at 80 ˚C. The wafer was then dipped into BOE again to remove the buried SiO_2 (BOX) layer to expose the silicon device layer. Finally, the PDMS film was peeled off with a sharp blade. In step 6, the isolation trenches and bottom electrode windows were etched out using inductively coupled plasma (ICP). In the next step, PECVD SiO_2 was deposited as the passivation layer. The top and bottom electrode areas were exposed using reactive ion etching (RIE) in step 8. In the final step, 200-nm aluminum electrodes were deposited using sputtering and patterned through the lift-off process. It should be mentioned that a thick photoresist (AZ4620, Electronic Materials plc) was used in steps 8 and 9, because the isolation trenches are 20 um deep and could not be entirely covered by the thin photoresist such as AZ3312 (Electronic Materials plc) using the spin coating method.

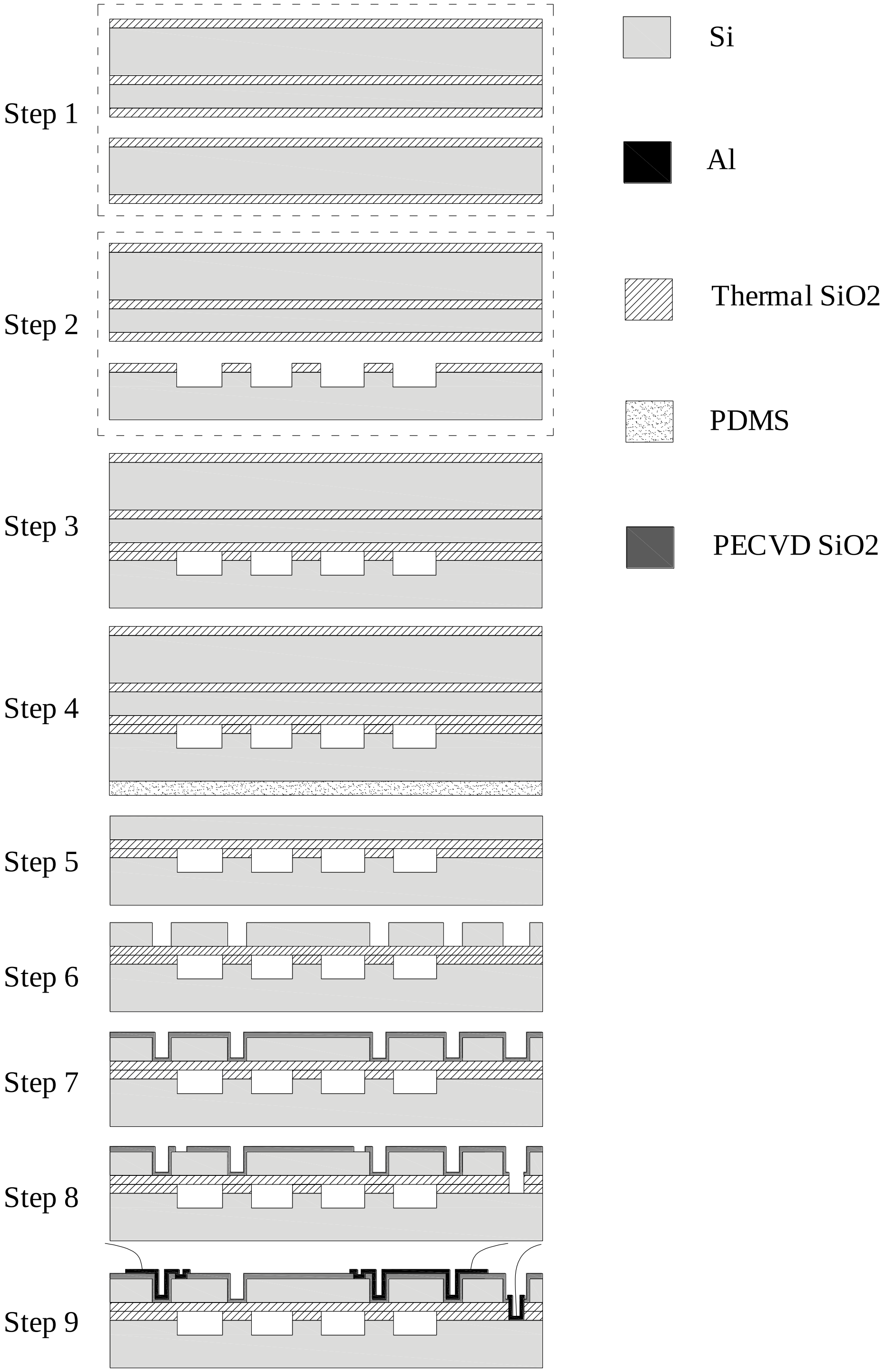

Figure. 7.2.2 Fabrication process of the CMUT array.

In developing the fabrication process, two significant challenges were encountered: etching the large-area cell cavities without silicon pillars and depositing the electrode leads with no virtual connections in the isolation trenches.

7.2.1 Fabrication of Pillar-free Cavities

Silicon pillars were created in the DRIE process, where the photoresist residue or particle contaminations acted as micro masks. Figure 7.2.3 shows a scanning electron microscope (SEM) image of a silicon pillar, which leads to a protrusion the plate. It is noted that the silicon pillar has a gradient sidewall on the right side. This was possibly due to the unevenness of the photoresist residue, the right part of which was completely consumed before the DRIE was finished. Silicon pillars in the cavities are detrimental to the CMUT performance as they obstruct the plate displacement and may cause plate cracking due to their sharp ends. In the earlier fabrication runs, the positive photoresist was used to pattern the cavities. Due to unavoidable contaminations, such as dust and photoresist residue on the transparent regions of the photomask, it was almost impossible to eliminate the silicon pillars. The same issue was also reported in [80], where the researchers managed to improve the photolithography quality by performing a second exposure after rotating the photomask by 180°. However, this approach requires the photomask to be redesigned and the two alignments to be perfectly matched. Moreover, a second exposure still cannot guarantee pillar-free cavities because the particles introduced in the photoresist spin coating and the photoresist bombarded off the wafer during DRIE can also induce silicon pillars. Since negative photoresist could define the cavities with the photomask opaque regions, which were robust to contamination, the author redesigned the mask and turned to using negative photoresist (AZ nLOF 2035, AZ Electronic Materials plc). Taking two random runs as an example, the number of particles in the cavity areas across the whole wafer after photolithography was found to reduce from 21 (positive photoresist) to 8 (negative photoresist). The remaining particles might be the dust introduced in the spin coating or the photoresist residue transferred from the mask. After the DRIE process, the number of silicon pillars present in the cavity areas was found to be 14. The additional 6 pillars are believed to result from the contaminations on the DRIE chamber wall or the photoresist particles bombarded off the sample. Even though the chamber can be cleaned and preconditioned, eliminating the photoresist particles is challenging because photoresist presents as the etching mask. As a result, the photolithography process was modified to using a metal mask.

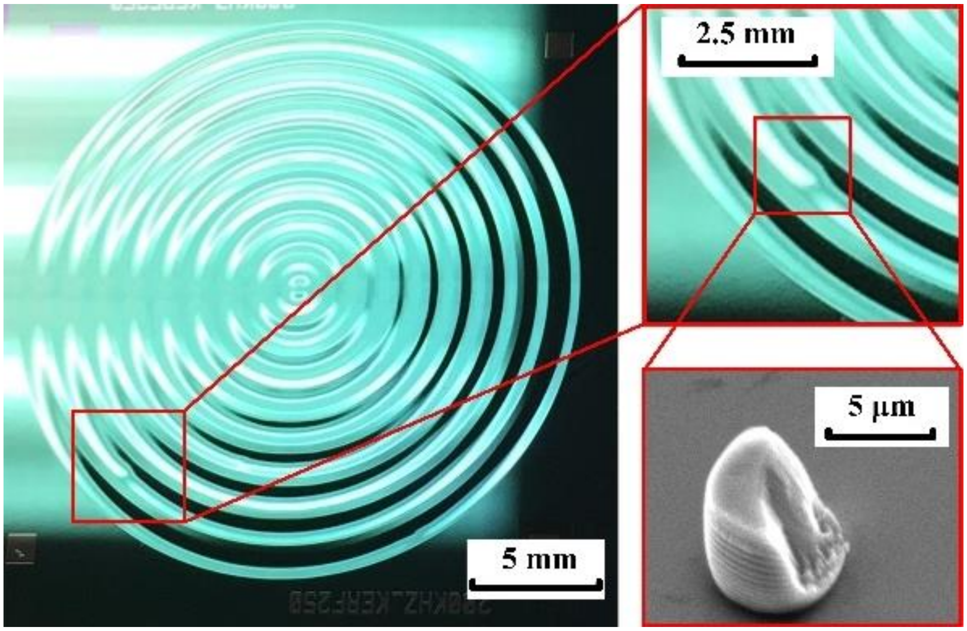

Figure 7.2.3 A silicon pillar found in the cavity.

The metal mask-based pillar-free large-area cavity fabrication process is illustrated in Fig. 7.2.4, where the particle contaminations are represented by the protrusions in the cavity. Firstly, a layer of 500-nm chromium was deposited on the bottom wafer through electron-beam evaporating. Secondly, the chromium layer was patterned with cavities using negative photoresist. In step 2-3, the exposed chromium was removed through wet etch leaving the particles in the cavity. Steps 2-4 and 2-5 were used to over etch the chromium underneath the particles such that the particles could be released. In step 2-6, the SiO_2 in the cavity areas was removed by BOE, and the photoresist was stripped off. In the final step, DRIE was used to etch the cavities with the chromium mask, which was removed afterwards. It should be mentioned that steps 2-4 and 2-5 can also cause the chromium at the cavity boundaries to be over etched. Nevertheless, since the width of the over-etched chromium is rather small compared to the width of the cavity, its impact on the CMUT performance is very small. On the other hand, if the chromium layer is not used, it would be challenging to achieve a pillar-free cavity by over etching the SiO_2. This is because the etching rate of SiO_2 in BOE is very slow, and the photoresist can be damaged after a period of time.

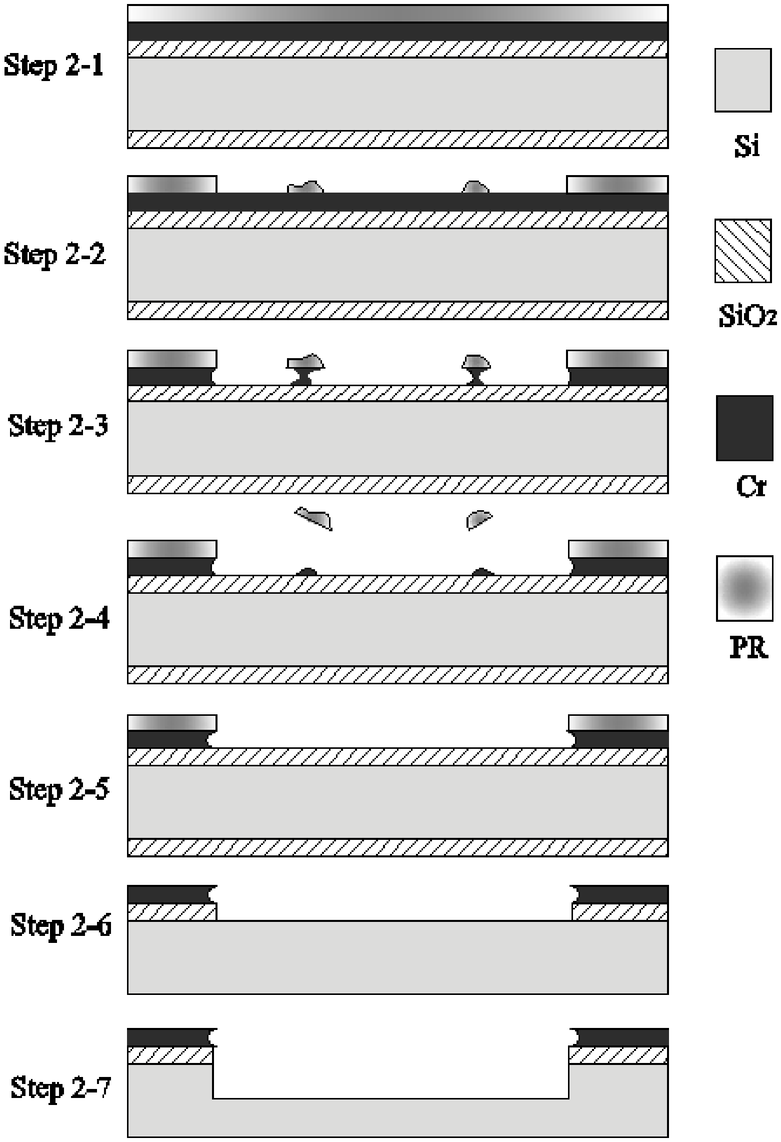

Figure 7.2.4 Metal mask-based pillar-free large-area cavity etching process.

7.2.2 ICP Etching of Isolation Trenches

Another fabrication challenge is depositing the electrode leads without virtual connections in the isolation trenches. In the early runs of this project, DRIE was used to create the isolation trenches, and 200-nm aluminum electrode leads were deposited through sputtering. The resistance between the two top electrode bonding pads of Cell *1* was measured to be around 700 Ω, which became infinitely high after the device was loaded with a DC bias and AC voltage. To identify the problem, we took SEM pictures of the trenches before and after loading the CMUTs. As shown in Fig. 7.2.5, virtual connections, which are indicated by the burning marks at the foot of the trench wall, can be found. The virtual connections can be attributed to two reasons: the steep trench walls and the notching effect caused by DRIE when SiO_2 is used as the etching stop layer [100].To overcome the virtual connection problem, we modified the trench etching process by using an ICP etching. The ICP recipe was developed on a RIE etcher (Phantom II Reactive-ion Etching system, Trion technology, FL), in Giga-to-Nanoelectronics Centre, University of Waterloo, as Table 7.2.1:

Table. 7.2.1 ICP etching recipe

Gas	Sulfur tetrafluoride (SF_6) / Tetrafluoromethane (CF_4)
Flow rate (SCCM)	50/100
Pressure (mTorr)	50
Power (W)	250
Etching rate (µm/min)	1.35 ~ 1.38

SEM images of the cross sections of the trenches fabricated through DRIE and the developed ICP etching are illustrated in Fig. 7.2.6. It shows that the slant angle of the trench wall was increased from 90º to 135º. As a result, better step coverage of the electrode leads was achieved and the resistance between the two bonding pads of Cell *1* was eventually measured to be less than 50 Ω.

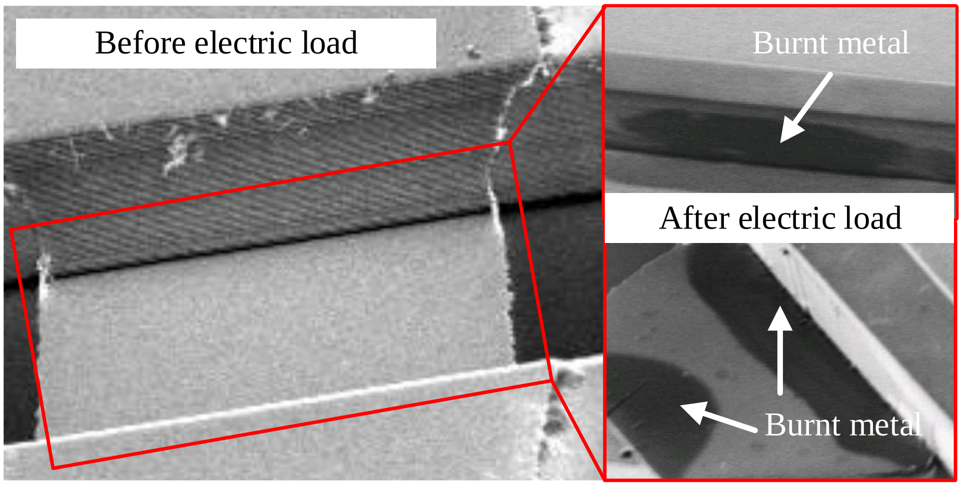

Figure. 7.2.5 SEM images of an electrode lead in the DRIE isolation trench.

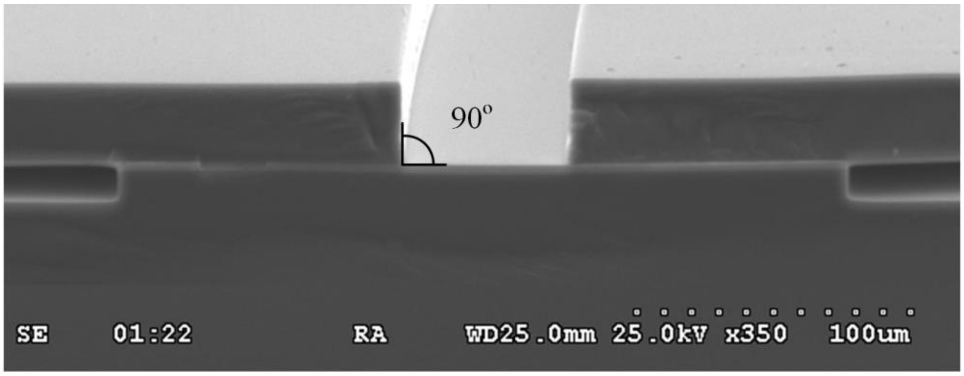

(a)

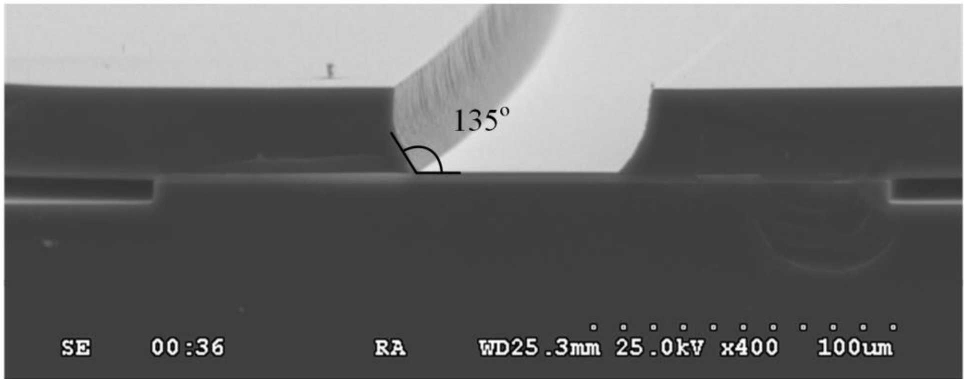

(b)

Figure. 7.2.6 SEM images of the isolation trenches fabricated by: (a) DRIE. (b) ICP.

7.3 Characterization and Discussion

7.3.1 Static Displacement

The plate static displacements along the radial direction were first characterized using a profilometer (Dektak 8 Stylus Profiler, Bruker Corp) (Fig. 7.3.1). As predicted in Section 7.1, the static displacements are rather consistent among the cells. The average maximum displacement was measured to be 1.72 μm, which is 0.3 μm larger than the predicted value. The isolation trench depth, which is also equal to the plate thickness, was measured to be 19.21 μm. The fact that the measured plate thickness is 0.14 μm smaller than the design value can partially explain the underestimation of the static displacement. Based on Fig. 7.3.1, the rms static displacement and the ratio of rms-to-maximum displacement (RRMD) can be calculated to be 1.10 μm and 0.64, which agree well with the results obtained in Chapters 4 and 5.

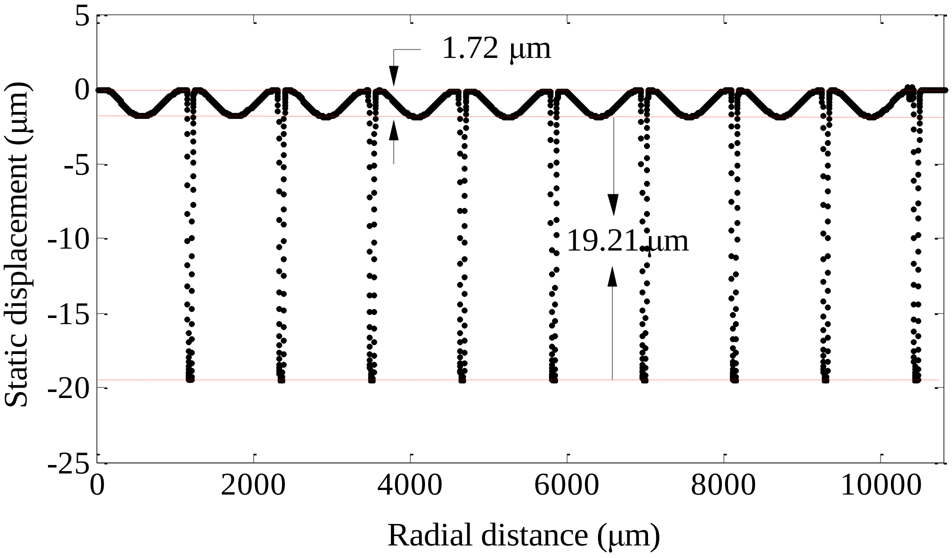

Figure. 7.3.1 Measured plate static displacements of Cells *1* to *9*.

7.3.2 Frequency response

The dynamic performance of the fabricated CMUT array was characterized using an LDV (OFV-5000, Polytec Inc). A DC power source (GPR-30H10D, Good Will Instrument Co., Ltd) was used to individually bias the CMUT cells at 100 V and 150 V, and a function generator (4040B, B&K Precision Corp) was used to actuate the biased CMUT cells with a 20-Vpp continuous-wave (CW) sinusoidal signal. The AC signal was monitored by an oscilloscope (DSO-X 3034A, Agilent Technologies Inc). The frequency response of the maximum dynamic displacement of each cell was measured at a sampling step of 200 Hz and shown in Fig. 7.3.2. The resonance frequencies at DC biases and the maximum dynamic displacements were extracted from Fig. 7.3.2 and summarized in Table. 7.3.1. Combining Tables. 7.3.1 and 7.1.3, it can be found that the measured resonance frequencies at DC biases of 100 and 150 V are lower than the predicted values by around 2 and 3 kHz, respectively. The measured maximum dynamic displacements are smaller than the predicted ones by approximately 20%. On one hand, the overestimated biased resonance frequency is a result of the overestimated plate thickness and the over-etched cavity widths. On the other hand, the fact that the material and structural damping was ignored in the design calculations may also lead to a decreased resonance frequency and dynamic displacement. Based on the measurement results, the average surface output power densities of the CMUT was calculated to be 0.40 and 0.96 kW/m^2

at DC biases of 100 and 150-V, respectively.

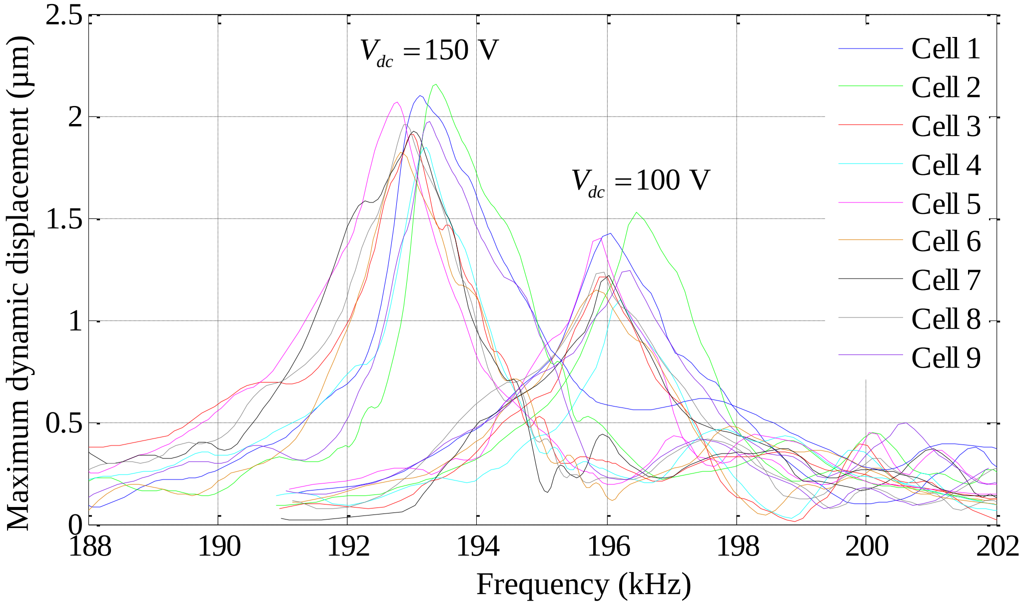

Figure. 7.3.2 Frequency responses at 20-Vpp AC and DC biases of 100 and 150 V.

Table. 7.3.1 Measured resonance frequencies, maximum dynamic displacements, and calculated surface power densities of Cells *1-9*.

Cell	V_{dc}=100 V			V_{dc}=150 V		
	f_{dc} (kHz)	u_{p_ac} (μm)	P_{ower} (kW/m^2)	f_{dc} (kHz)	u_{p_ac} (μm)	P_{ower} (kW/m^2)
1	196.0	1.42	0.51	193.1	2.10	1.08
2	196.5	1.53	0.42	193.4	2.16	1.15
3	196.0	1.21	0.37	193.0	1.91	0.90
4	196.2	1.10	0.31	193.2	1.84	0.83
5	195.9	1.40	0.50	192.8	2.07	1.05
6	195.8	1.15	0.33	192.8	1.82	0.81
7	195.9	1.22	0.38	193.0	1.92	0.90
8	195.9	1.23	0.38	192.9	1.96	0.94
9	196.3	1.24	0.39	193.3	1.97	0.96

7.3.3 Cross-talk

A multi-point scan of each activated cell and its neighbouring cells was performed to evaluate the cross-talk between neighbouring cells (Fig. 7.3.3). The scan was conducted at 100-V DC bias and 20-Vpp AC voltage at a frequency of 196.1 kHz. The particular AC frequency was chosen because it was the average resonance frequency, where the nine cells responded with relatively consistent amplitudes. Since the maximum scan area of the laser is 3 × 3 mm, only a portion of the aperture was covered. Figure. 7.3.3 reveals that significant cross-talk existed on Cell *1* when Cell *2* was activated. One explanation is that Cell *1* has a resonance frequency close to 196.1 kHz and therefore responded with a high amplitude. On the other hand, the cross-talk on Cell *2* was much smaller when Cell *1* was activated. This is possibly due to the acoustic interference effect that the vibration of Cell *2* coupled into the support posts, propagated through the substrate, and focused at the center area. The maximum cross-talk displacement of Cell *1* was measured to be 0.6 µm, -13 dB of the vibration amplitude of Cell *2*. Since acoustic coupling in air is generally weak due to the low air impedance, the observed cross-talk is believed to mainly result from the acoustic coupling in the substrate. Therefore, the cross-talk can be reduced by increasing the widths of the isolation trenches and the supporting posts of the cells.

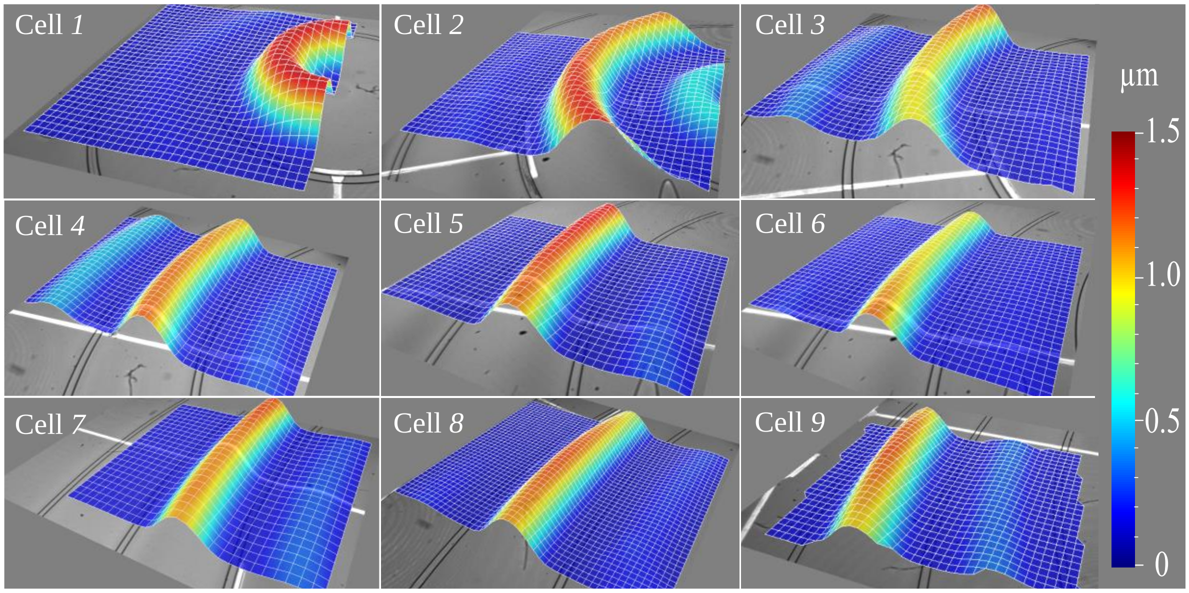

Figure 7.3.3 Multi-point scan of each activated cell and its neighbouring cells.

Figure. 7.3.3 also indicates non-uniformity of plate vibration, which is more significant on the cells with larger radii. This can be explained by the fact that the variations of plate thicknesses and cavity depths are more significant across a larger area. The cavity depths were characterized with a variation of 1.7% across the whole device area (2 × 2 cm), and the plate thickness has a variation of 2.5% across the 4-inch wafer area according to the SOI specification. However, since a burst signal, which consists of a single frequency component, is normally used to actuate an air-coupled CMUT, the plates will still vibrate at the fundamental model. This was confirmed by the fact that no node was found on the entire plates during the LDV measurement. To improve the vibration uniformity, an SOI wafer with a higher device layer uniformity can be used as the top wafer. To decrease the variation of the cavity depths, an SOI wafer can be employed as the bottom wafer, such that the BOX layer can be used as the stopping layer for the cavity etching, and the cavity depth can be strictly controlled by the thickness of the device layer. Another advantage of using an SOI wafer as the bottom wafer is that it can provide a very high breakdown voltage [81][101].

7.3.4 Plate Cracking

A problem of plate cracking (Fig. 7.3.4) was encountered when biasing the CMUT at 150 V and increasing the AC excitation voltage from 20 to 32 Vpp using a signal amplifier (Model 9400, Tabor Electronics Ltd). According to the LDV measurement, the maximum plate displacement reached the maximum value of 3.51 µm when the AC excitation voltage was increased to 30 Vpp. The plate cracked as we further increased the AC voltage to over 32 Vpp. This means that the vibrating plate made contact with the cavity bottom when the cracking happened. The strike between the plate and cavity is believed to be the main reason for the cracking. However, there are few literatures on the failure of CMUT plates, the mechanism of the plate cracking requires further investigations. Nevertheless, since an annular CMUT plate suffers a higher stress concentration at the boundaries due to its smaller circumference-to-area ratio and larger RAMD compared with a circular plate, a thicker plate can be used to increase the failure strength at the plate boundaries so as to prevent the plate from cracking.

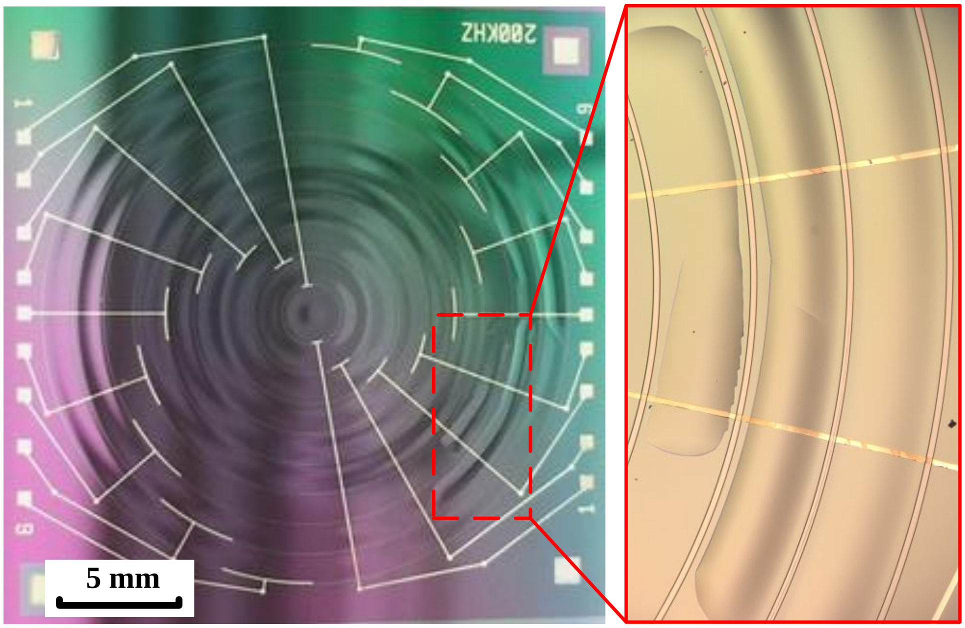

Figure. 7.3.4 Optical images of the cracked plates.

Chapter 8 Summary and Future Work

8.1 Summary

In an attempt to improve the transmit efficiency of current air-coupled CMUTs, a novel CMUT cell design based on annular geometry was proposed in Chapter 3. The simulated results for the annular cell show a 58% ~ 76% RAMD improvement relative to a conventional circular one. Due to the RAMD improvement, the annular CMUT's the transmit sensitivity, in Pa/V, and the output power intensity, in W/m^2, are simulated to be 48.4% and 127.3% higher than that of a circular one. 94.5-kHz single-cell annular CMUTs were fabricated using the wafer bonding technique. Since the design has a millimeter-level cavity dimension, a high-quality lithography process is required to avoid photoresist residual in the cavity area. Otherwise, silicon pillars will form during the following DRIE cavity etching step. In the end, a negative photoresist was used to pattern the cavity because even if the mask had contaminations in the cavity area (opaque on the mask), the photoresist under the area would not be affected. In addition, achieving a uniform electric field between the electrodes requires a smooth cavity bottom surface and a high cavity aspect ratio. For this purpose, DRIE with a slow etching rate and short etch/deposit cycle was used.

A RMS output pressure of 338.27-Pa was calculated at the CMUT surface based on the measured dynamic displacement via a vibrometer at 170-V DC bias and 20-Vpp AC excitation. Considering that the CMUT is only biased at 34% of the pull-in voltage (498 V), the output pressure is promising. Currently, the DC bias is limited at 170 V due to a relatively low breakdown voltage of the insulating layer. This is largely due to a temporary contamination problem associated with the oxide furnace in the cleanroom. A thicker and better-quality insulating layer can address this issue and increase the output pressure. For example, if the DC bias is increased from 34% to 75% of the pull-in voltage, the rms output pressure is simulated to be 878.84 Pa which leads to a 160% improvement.

The experiment results agreed with the simulation results in the maximum dynamic displacement while the center frequency and the -3-dB FBW are underestimated in the simulation. Perhaps the mismatch can be attributed to the support loss which was ignored in the finite element model. When the plate vibrates, a portion of the in-plane energy is coupled into the support substrate at the clamped edges. Since an annular plate has two separate clamped edges, the support loss will be more significant than that of a circular plate.

In some cases, the efficacy of an ultrasonic transducer is strictly measured by the transmit efficiency of the transducer relative to the aperture size. While the efficiency may be improved for a given vibrating plate area, a single annular cell does indeed have a larger overall aperture (active plate area). In other words, the outer radius of an annular cell may still be larger than that of a circular cell. Nonetheless, the annular shape allows cells of different sizes to be patterned into a concentric array. Since each annular cell is continuous in the circumferential direction, the fill factor of the layout is larger compared to that of an annular layout made of circular cells. In another embodiment, the annular cell design would fit well with devices that require a hollow center.

In Chapter 5, an analytical model was developed to facilitate a better understanding as well as provide a reliable design technique of the air-coupled annular CMUTs. Explicit expressions of the resonance frequency, modal vector, and static displacement of a clamped annular plate under uniform pressure were developed based on the plate theory and curve fitting method. Using these expressions, a lumped element model based on the mass-spring-damper system was proposed for analyzing annular-cell air-coupled CMUTs. The proposed lumped model was verified by both simulation and experiments on a fabricated device. The fabricated device shared the same fabrication processes with that in Chapter 4 but with a full set of masks. The verification results of the static displacement at atmospheric pressure and DC bias, pull-in voltage, frequency and transient response demonstrate that the analytical model is able to provide comparable accuracy of a FEA model and will save significant computation time.

In chapter 6, three optimization schemes are proposed for designing air-coupled CMUT cells based on the principle that the maximum plate displacement is equal to the cavity depth, Scheme I assumes fixed DC bias and AC excitation voltage, at which the cavity depth is optimized to maximize the output RMS power density at the plate surface. Given the power density, Schemes II and III optimize the cavity depth to minimize the requirements on DC bias and AC excitation voltage, respectively. A design optimization flow chart was developed based on the lumped models to facilitate analytical optimization. Using the wafer bonding technique, circular and annular CMUT cells of 97 kHz were fabricated to verify the optimization principle. The measured results agree well with the calculated ones in both static and dynamic aspects.

Based on the optimization flow chart, the circular and annular cells with natural frequencies between 100 and 300 kHz were analytically optimized. The calculated results of Scheme I demonstrate that an annular cell can generate double the power density of a circular cell at the plate surface. According to the results of Schemes II and III, an annular cell only requires half the DC bias and AC excitation voltage of a circular cell to generate the same power density. Considering the improved transmit efficiency of annular cells, we are exploring concentric annular arrays, where individually-addressed annular cells are arranged in a concentric layout, to generate high-intensity focused ultrasound along the depth direction.

In Chapter 7, considering that the annular configuration allows multiple cells to be arranged in a concentric layout, which promises the highest fill factor [19], a concentric annular-cell array is proposed to further enhance the transmit power and offer depth focusing. The proposed array consists of nine cells, which are separated by isolation trenches. The lumped element model demonstrated in Chapter 5 was adopted to design the cells and predict their performance. The CMUT was fabricated based on the wafer bonding technique [21]. A novel pillar-free etching process was developed to create the deep large-area cell cavities. A fabrication process modified for enhancing the electroconductivity of the electrical leads in the isolation trenches is described. The fabricated CMUT was characterized for both the static and dynamic performance. The measured static displacements and frequency responses of the nine cells showed good consistency and agreed well with the predicted values. The maximum amplitude of the cross-talk vibration was found at the center cell and measured to be 0.6 µm. A wider isolation trench can be designed to reduce the cross-talk. The plate-cracking phenomenon was studied and attributed to the strike between the plate and cavity. We suggested that a thicker plate be adopted to increase the failure strength in order to prevent the cracking problem. The CMUT produced a surface power density of 0.96 kW/m2 at DC bias of 150 V and AC excitation voltage of 20 Vpp. To achieve a higher output power, one can design the CMUT with a deeper cavity, thicker plate, and thicker insulating layer and operate it at a higher electric power.

8.2 Future Work

In the short term, efforts should be concentrated on three aspects. First, as stated in Chapter 5, the support loss is suspected to play a role in the damping mechanism of the annular plate. Therefore, characterization of the support loss in a vacuum chamber can help improve the accuracy of the analytical model. Secondly, thick silicon plates instead of thin ones were used throughout this thesis. This is due to the fact that the deflection of a thick plate is small compared to its thickness and can avoid the large deflection effects due to the static displacement under the atmospheric pressure. Even though the same principle can be followed in the future, a comprehensive analytical model which covers the non-linear phenomenon of a large-deformed plate can make the design more flexible. Thirdly, more studies should be performed to improve the frequency consistency and plate deformation uniformity among the cells and investigating the cross-talk and plate-cracking mechanisms to allow for a better array design.

In the long term, a dedicated beamforming circuit board, which has a high-power capability, needs to be constructed. The board should be able to generate an AC bust signal with a high amplitude, for example 60 Vpp, to allow the optimal operation of an annular CMUT array. In addition, the acoustic field and the transmit waveforms of the annular array need to be characterized using a commercial calibrated microphone. Furthermore, even though this study is dedicated to developing CMUTs for transmitting ultrasound, Chapter 4 has demonstrated that the design can also be used for receiving ultrasound. However, using the same design of a transmit CMUT for receiving ultrasound is not efficient. This is because a transmit CMUT is intendedly designed with a large cavity depth, which leads to a low capacitance and sensitivity. As a result, the receive CMUTs should be separately designed with a small cavity depth. However, it should be noted that, to achieve a consistent resonance frequency, the radius dimensions of the receive CMUT need to be recalculated since it has a higher spring softening level compared to that of the transmit CMUT.

Bibliography

[1] T. L. Szabo, *Diagnostic ultrasound imaging: inside out*: Academic Press, 2004.

[2] J. Blitz and G. Simpson, *Ultrasonic methods of non-destructive testing* vol. 2: Springer Science & Business Media, 1996.

[3] J. E. Kennedy, “High-intensity focused ultrasound in the treatment of solid tumours,” *Nature reviews cancer,* vol. 5, pp. 321-327, 2005.

[4] J. E. Kennedy, G. R. Ter Haar, and D. Cranston, “High intensity focused ultrasound: surgery of the future?,” *The British journal of radiology,* vol. 79, no. 909, pp. 590-599, 2014.

[5] N. J. Friberg and C. A. Boulos, “Ultrasonic vehicle positioning apparatus and method,” U.S. Patent No (5208586), 1993.

[6] L. C. Lynnworth, *Ultrasonic measurements for process control: theory, techniques, applications*: Academic press, 2013.

[7] V. Magori, “Ultrasonic sensors in air,” in *1994 IEEE International Ultrasonics Symposium,* vol. 3, pp. 471-481, 1994.

[8] T. Dahl, J. L. Ealo, H. J. Bang, S. Holm, and P. Khuri-Yakub, “Applications of airborne ultrasound in human–computer interaction,” *Ultrasonics,* vol. 54, no. 7, pp. 1912-1921, 2014.

[9] J. Cheng and L. J. Bond, “Assessment of ultrasonic NDT methods for high speed rail inspection,” in *AIP Conference Proceedings,* 2015, vol. 1650, no. 1, pp. 605-614.

[10] W. A. Grandia and C. M. Fortunko, “NDE applications of air-coupled ultrasonic transducers,” in *1995 IEEE international Ultrasonics Symposium,* pp. 697-709, 1995.

[11] L. Jakevičius and A. Demčenko, “Ultrasound attenuation dependence on air temperature in closed chambers,” *Ultragarsas (Ultrasound),* vol. 63, no. 1, pp. 18-22, 2008.

[12] E. Blomme, D. Bulcaen, and F. Declercq, “Air-coupled ultrasonic NDE: experiments in the frequency range 750 kHz-2 MHz,” *NDT & E International*, vol. 35, no. 7, pp. 417-426, 2002.

[13] P. Muralt, N. Ledermann, J. Paborowski, A. Barzegar, S. Gentil, B. Belgacem, S. Petitgrand, A. Bosseboeuf , and N. Setter, “Piezoelectric micromachined ultrasonic transducers based on PZT thin films,” *Ultrasonics, Ferroelectrics, and Frequency Control, IEEE Transactions on,* vol. 52, no. 12, pp. 2276-2288, 2005.

[14] D. W. Schindel, D. A. Hutchins, L. Zou, and M. Sayer, “The design and characterization of micromachined air-coupled capacitance transducers,” *IEEE Transactions on Ultrasonics, Ferroelectrics, and Frequency Control,* vol. 42, no. 1, pp. 42-50, 1995.

[15] X. Jin, I. Ladabaum, and B. T. Khuri-Yakub, “The microfabrication of capacitive ultrasonic transducers,” *Journal of Microelectromechanical Systems,* vol. 7, no. 3, pp. 295-302, 1998.

[16] X. Jin, I. Ladabaum, F. L. Degertekin, S. Calmes, and B. T. Khuri-Yakub, “Fabrication and characterization of surface micromachined capacitive ultrasonic immersion transducers,” *Journal of Microelectromechanical Systems,* vol. 8, o. 1, pp. 100-114, 1999.

[17] A. S. Ergun, G. G. Yaralioglu, and B. T. Khuri-Yakub, “Capacitive micromachined ultrasonic transducers: Theory and technology,” *Journal of Aerospace Engineering,* vol. 16, no. 2, pp. 76-84, 2013.

[18] Y. Huang, E. O. Hæggstrom, X. Zhuang, A. S. Ergun, and B. T. Khuri-Yakub, “Optimized membrane configuration improves CMUT performance,” in *2004 IEEE International Ultrasonics Symposium*, vol. 3, pp. 505-508, 2004.

[19] Y. Huang, X. Zhuang, E. Hggstrom, A. S. Ergun, C.-H. Cheng, and B. T. Khuri-Yakub, “Capacitive micromachined ultrasonic transducers with piston-shaped membranes: Fabrication and experimental characterization,” *IEEE Transactions on Ultrasonics, Ferroelectrics, and Frequency Control,* vol. 56, no. 1, pp. 136-145, 2009.

[20] T. A. Emadi and D. A. Buchanan, “Design and fabrication of a novel MEMS capacitive transducer with multiple moving membrane, M3- CMUT,” *IEEE Transaction on*

Electron Devices, vol. 61, no. 3, pp. 890-896, 2014.

[21] A. Unlugedik, A. S. Tasdelen, A. Atalar, and H. Koymen, "Designing transmitting CMUT cells for airborne applications," *IEEE Transactions on Ultrasonics, Ferroelectrics, and Frequency Control*, vol. 61, no. 11, pp. 1899-1910, 2014.

[22] F. Y. Yamaner, S. Olcum, H. K. Oguz, A. Bozkurt, H. Koymen, and A. Atalar, "High-power CMUTs: design and experimental verification," *IEEE Transactions on Ultrasonics, Ferroelectrics, and Frequency Control*, vol. 59, no. 6, pp. 1276-1284, 2012.

[23] I. O. Wygant, M. Kupnik, J. C. Windsor, W. M. Wright, M. S. Wochner, G. G. Yaralioglu, M. F. Hamilton, and B. T. Khuri-Yakub, "50 kHz capacitive micromachined ultrasonic transducers for generation of highly directional sound with parametric arrays," *IEEE Transactions on Ultrasonics, Ferroelectrics, and Frequency Control*, vol. 56, no. 1, pp. 193-203, 2009.

[24] X. Wang, Y. Fan, W. C. Tian, H. J. Kwon, S. Kennerly, G. Glaydon, and A. May, "Development of air-coupled ultrasound transducers for nondestructive evaluation," in *2008 IEEE International Conference on Micro Electro Mechanical Systems*, pp. 932-935, 2008.

[25] K. K. Park and B. T. Khuri-Yakub, "3-D airborne ultrasound synthetic aperture imaging based on capacitive micromachined ultrasonic transducers," *Ultrasonics*, vol. 53, no. 7, pp. 1355-1362, 2013.

[26] M. Kupnik, S. Vaithilingam, K. Torashima, I. O. Wygant, and B. T. Khuri-Yakub, "CMUT fabrication based on a thick buried oxide layer," *2010 IEEE International Ultrasonics Symposium*, pp. 547-550.

[27] S. Na, A. I. H. Chen, L. L. P. Wong, Z. Li, M. Macecek, and J. T. W. Yeow, "Capacitive micromachined ultrasonic transducers based on annular cell geometry for air-coupled applications," *Ultrasonics*, vol. 71, pp. 152-160, 2016.

[28] S. Na, L. L. P. Wong, A. I. H. Chen, Z. Li, M. Macecek, and J. T. W. Yeow, "Lumped element modeling of air-coupled capacitive micromachined ultrasonic transducers with annular cell geometry," *Ultrasonics*, vol. 76, pp. 19-27, 2017.

[29] S. Na, L. L. P. Wong, A. I. H. Chen, Z. Li, M. Macecek, and J. T. W. Yeow, "A CMUT

array based on annular cell geometry for air-coupled applications," in 2016 IEEE International Ultrasonics Symposium, pp. 1-4, 2016.

[30] E. Blomme, D. Bulcaen, and F. Declercq, "Recent observations with air-coupled NDE in the frequency range of 650 kHz to 1.2 MHz," *Ultrasonics*, vol. 40, no. 1, pp. 153-157, 2002.

[31] T. E. G. Alvarez-Arenas, "Acoustic impedance matching of piezoelectric transducers to the air," *IEEE Transactions on Ultrasonics, Ferroelectrics, and Frequency Control*, vol. 51, no. 5, pp. 624-633, 2004.

[32] R. E. Newnham, L. Bowen, K. Klicker, and L. Cross, "Composite piezoelectric transducers," *Materials & Design*, vol. 2, no. 2, pp. 93-106, 1980.

[33] W. A. Smith, "The role of piezocomposites in ultrasonic transducers," in *1989 IEEE International Ultrasonics Symposium*, pp. 755-766, 1989.

[34] M. Castaings, P. Cawley, R. Farlow, and G. Hayward, "Single sided inspection of composite materials using air coupled ultrasound," *Journal of Nondestructive Evaluation*, vol. 17, no. 1, pp. 37-45, 1998.

[35] D. K. Hsu, "Nondestructive testing using air-borne ultrasound," *Ultrasonics*, vol. 44, pp. e1019-e1024, 2006

[36] M. Haller and B. T. Khuri-Yakub, "A surface micromachined electrostatic ultrasonic air transducer," *IEEE Transactions on Ultrasonics, Ferroelectrics, and Frequency Control*, vol. 43, no. 1, pp. 1-6, 1996.

[37] G. Caliano, A. Caronti, A. Savoia, C. Longo, M. Pappalardo, E. Cianci, and V. Foglietti, "Capacitive micromachined ultrasonic transducer (cMUT) made by a novel 'reverse fabrication process'," in *2005 IEEE International Ultrasonics Symposium*, pp. 479-82, 2005.

[38] A. Logan and J. T. W. Yeow, "Fabricating capacitive micromachined ultrasonic transducers with a novel silicon-nitride-based wafer bonding process," *IEEE Transactions on Ultrasonics, Ferroelectrics, and Frequency Control*, vol. 56, no. 5, pp. 1074-1084, 2009.

[39] A. Stoffel, A. Kovacs, W. Kronast, and B. Muller, “LPCVD against PECVD for micromechanical applications,” *Journal of Micromechanics and Microengineering*, vol. 6, no. 1, pp. 1-13, 1996.

[40] H. T. Soh, I. Ladabaum, A. Atalar, C. F. Quate, and B. T. Khuri-Yakub, “Silicon micromachined ultrasonic immersion transducers,” *Applied Physics Letters*, vol. 69, no. 24, pp. 3674-3676, 1996.

[41] B. T. Khuri-Yakub, C.-H. Cheng, F.-L. Degertekin, S. Ergun, S. Hansen, X.-C. Jin, and O. Oralkan, “Silicon micromachined ultrasonic transducers,” *Japanese Journal of Applied Physics*, vol. 39, no. 1, pp. 2883, 2000.

[42] E. Cianci, L. Visigalli, V. Foglietti, G. Caliano, and M. Pappalardo, “Improvements towards a reliable fabrication process for cMUT,” *Microelectronic Engineering*, vol. 67-68, pp. 602-608, 2003.

[43] O. Ahrens, A. Buhrdorf, D. Hohlfeld, L. Tebje, and J. Binder, “Fabrication of gap-optimized CMUT,” *IEEE Transactions on Ultrasonics, Ferroelectrics, and Frequency Control*, vol. 49, no. 9, pp. 1321-1329, 2002.

[44] B. Belgacem, D. Alquier, P. Muralt, J. Baborowski, S. Lucas, and R. Jerisian, “Optimization of the fabrication of sealed capacitive transducers using surface micromachining,” *Journal of Micromechanics and Microengineering*, vol. 14, no. 2, pp. 299-304, 2003.

[45] A. Erguri, Y. Huang, X. Zhuang, O. Oralkan, G. G. Yarahoglu, and B. T. Khuri-Yakub, “Capacitive micromachined ultrasonic transducers: fabrication technology,” *IEEE Transactions on Ultrasonics, Ferroelectrics, and Frequency Control*, vol. 52, no. 12, pp. 2242-2258, 2005.

[46] Y. Huang, E. Hæggstrom, M. H. Badi, and B. Khuri-Yakub, “Fabricating capacitive micromachined ultrasonic transducers with wafer-bonding technology,” *Journal of Microelectromechanical Systems*, vol. 12, no. 2, pp. 128-137, 2003.

[47] P. Ramm, J. J. -Q. Lu, and M. M. Taklo, *Handbook of Wafer Bonding*: John Wiley & Sons, 2012.

[48] A. Bakhtazad, R. Manwar, and S. Chowdhury, “Fabrication and characterization of

sealed cavities realized by adhesive wafer bonding with dry etched Cyclotene™," *Microsystem Technologies*, vol. 21, no. 11, pp. 2435-2442, 2015.

[49] Li Z, Chen A I H, Wong L L P, S. Na, and J. T. W. Yeow, "Fabrication of polymer-based wafer-bonded capacitive micromachined ultrasonic transducers," *2015 IEEE International Ultrasonics Symposium*, pp. 1-4, 2015.

[50] Li Z, Chen A I H, Wong L L P, S. Na, J. Sun, and J. T. W. Yeow, "Fabrication of capacitive micromachined ultrasonic transducers based on adhesive wafer bonding technique," *Journal of Micromechanics and Microengineering*, vol. 26, no. 11, pp. 1-11, 2016.

[51] F. Y. Yamaner, X. Zhang, and O. Oralkan, "A three-mask process for fabricating vacuum-sealed capacitive micromachined ultrasonic transducers using anodic bonding," *IEEE Transactions on Ultrasonics, Ferroelectrics, and Frequency Control*, vol. 62, no. 5, pp. 972-982, 2015.

[52] A. S. Logan, L. L. P. Wong, and J. T. W. Yeow, "2-D CMUT wafer bonded imaging arrays with a row-column addressing scheme," in *2009 IEEE International Ultrasonics Symposium*, pp. 984-987, 2009.

[53] A. S. Logan, L. L. P. Wong, A. I. H. Chen, and J. T. W. Yeow, "A 32 x 32 element row-column addressed capacitive micromachined ultrasonic transducer," *IEEE Transactions on Ultrasonics, Ferroelectrics, and Frequency Control*, vol. 58, no. 6, pp. 1266-1271, 2011.

[54] A. S. Logan, L. L. P. Wong, and J. T. W. Yeow, "A 1-D capacitive micromachined ultrasonic transducer imaging array fabricated with a silicon-nitride-based fusion process," *IEEE/ASME Transactions on Mechatronics*, vol. 16, no. 5, pp. 861-865, 2011.

[55] A. I. H. Chen, L. L. P. Wong, Z. Li, S. Na, and J. T. W. Yeow. "Practical CMUT Fabrication With a Nitride-to-Oxide-Based Wafer Bonding Process," *Journal of Microelectromechanical Systems*, vol. pp, no. 99, pp. 1-8, 2017.

[56] R. Legtenberg, H. A. C. Tilmans, J. Elders, and M. Elwenspoek, "Stiction of surface micromachined structures after rinsing and drying: model and investigation of adhesion mechanisms," *Sensors and actuators A: Physical*, vol. 43, no. 1, pp. 230-238, 1994.

[57] N. Tas, T. Sonnenberg, H. Jansen, R. Legtenberg, and M. Elwenspoek, “Stiction in surface micromachining,” *Journal of Micromechanics and Microengineering,* vol. 6, no. 4, pp. 385-397, 1996.

[58] B. T. Khuri-Yakub, O. Oralkan, and M. Kupnik, “Next-gen ultrasound,” *IEEE SpEctrum,* vol. 46, no. 5, pp. 44-54, 2009.

[59] I. Ladabaum, X. Jin, and B. Khuri-Yakub, “Air coupled through transmission of aluminum and other recent results using MUTs,” in *1997 IEEE International Ultrasonics Symposium,* pp. 983-986, 1997.

[60] D. A. Hutchins, J. S. McIntosh, A. Neild, D. R. Billson, and R. A. Noble, “Radiated fields of capacitive micromachined ultrasonic transducers in air,” *The Journal of the Acoustical Society of America,* vol. 114, no. 3, pp. 1435-1449, 2003.

[61] X. Wang, Y. Fan, W. -C. Tian, H. -J. Kwon, S. Kennedy, G. Claydon, and A. May, “Development of air-coupled ultrasound transducers for nondestructive evaluation,” in *2008 IEEE International Conference on Micro Electro Mechanical Systems*, pp. 932-935, 2008.

[62] K. K. Park, H. J. Lee, G. G. Yaralioglu, A. S. Ergun, O. Oralkan, M. Kupnik, C. F. Quate, B. T. Khuri-Yakub, T. Braun, J. -P. Ramseyer, H. P. Lang, M. Hegner, Ch. Gerber, and J. K. Gimzewski, “Capacitive micromachined ultrasonic transducers for chemical detection in nitrogen,” *Applied Physics Letters*, vol. 91, no. 9, pp. 91-93, 2007.

[63] K. K. Park, H. J. Lee, M. Kupnik, O. Oralkan, J. –P. Ramseyer, H. P. Lang, M. Hengner, C. Gerber, and B. T. Khuri-Yakub, “Capacitive micromachined ultrasonic transducer (CMUT) as a chemical sensor for DMMP detection,” *Sensors and Actuators B: Chemical*, vol. 160, no. 1, pp. 1120-1127, 2011.

[64] H. J. Lee, K. K. Park, M. Kupnik, O. Oralkan, and B. T. Khuri-Yakub, “Chemical vapor detection using a capacitive micromachined ultrasonic transducer” *Analytical chemistry*, vol. 83, no. 24, pp. 9314-9320, 2011.

[65] M. -C. Ho, M. Kupnik, K. K. Park, K. Eckhoff, and B. T. Khuri-Yakub, “Wide pressure range operation of air-coupled CMUTs,” in *2012 International Ultrasonics Symposium*, pp. 93-96, 2012.

[66] M. -C. Ho, K. K. Park, K. Eckhoff, M. Kupnik, and B. T. Khuri-Yakub, “Air-coupled CMUTs operating at ambient pressures ranging from 1 to 20 atm,” in *2013 International Ultrasonics Symposium*, pp. 1412-1415, 2013.

[67] M. Meloche and S. Chowdhury, “Design of a MEMS discretized hyperbolic paraboloid geometry ultrasonic sensor microarray,” *IEEE Transactions on Ultrasonics, Ferroelectrics, and Frequency Control*, vol. 55, no. 6, pp. 1363-1372, 2008.

[68] I. O. Wygant, M. Kupnik, and B. T. Khuri-Yakub, “Analytically Calculating Membrane Displacement and the Equivalent Circuit Model of a Circular CMUT Cell,” in *2008 IEEE International Ultrasonics Symposium*, pp. 2111-2114, 2008.

[69] A. W. Leissa, *Vibration of Plates*: Washington, D. C.: NASA, 1969.

[70] D. T. Porter, “Self-and Mutual-Radiation Impedance and Beam Patterns for Flexural Disks in a Rigid Plane,” *The Journal of the Acoustical Society of America*, vol. 36, no. 6, pp. 1154-1161, 1964.

[71] S. Adler, P. Johnson, and I. O. Wygant, “Low frequency CMUT with vent holes,” U.S. Patent (8455963), 2013.

[72] N. Apte, K. K. Park, A. Nikoozadeh, and B. K. Khuri-Yakub, “Bandwidth and sensitivity optimization in CMUTs for airborne applications” in *2014 IEEE International Ultrasonics Symposium*, pp. 166-169, 2014.

[73] W. Zhang and K. Turner, "Frequency dependent fluid damping of micro/nano flexural resonators: Experiment, model and analysis," *Sensors and Actuators A: Physical,* vol. 134, pp. 594-599, 2007.

[74] Z. Hao, A. Erbil, and F. Ayazi, “An analytical model for support loss in micromachined beam resonators with in-plane flexural vibrations,” *Sensors and Actuators A: Physical*, vol. 109, pp. 156-164, 2003.

[75] R. Lifshitz and M. L. Roukes, “Thermoelastic damping in micro-and nanomechanical systems,” *Physical review B,* vol. 61, no. 18, pp. 5600, 2000.

[76] D. McGuigan, C. Lam, R. Gram, A. Hoffman, D. Douglass, and H. Gutche, “Measurements of the mechanical Q of single-crystal silicon at low temperatures,”

Journal of Low Temperature Physics, vol. 30, no. 5, pp. 621-629, 1978.

[77] K. K. Park, H. J. Lee, P. Crisman, M. Kupnik, O. Oralkan, and B. T. Khuri-Yakub, “Optimum design of circular CMUT membranes for high quality factor in air,” in *2008 IEEE International Ultrasonics Symposium*, pp. 504-507, 2008.

[78] A. Bozkurt, I. Ladabaum, A. Atalar, and B. T. Khuri-Yakub, “Theory and analysis of electrode size optimization for capacitive microfabricated ultrasonic transducers,” *IEEE Transactions on Ultrasonics, Ferroelectrics, and Frequency Control*, vol. 46, no. 6, pp. 1364-1374, 1999.

[79] W. P. Mason, *Electromechanical transducers and wave filters*: D. Van Nostrand Co., 1948.

[80] I. O. Wygant, M. Kupnik, J. C. Windsor, W. M. Wright, M. S. Wochner, G. G. Yaralioglu, M. F. Hamilton, and B. T. Khuri-Yakub, “50 kHz capacitive micromachined ultrasonic transducers for generation of highly directional sound with parametric arrays,” *IEEE Transactions on Ultrasonics, Ferroelectrics, and Frequency Control*, vol. 56, no. 1, pp. 193-203, 2009.

[81] K. K. Park and B. T. Khuri-Yakub, “3-D airborne ultrasound synthetic aperture imaging based on capacitive micromachined ultrasonic transducers,” *Ultrasonics*, vol. 53, no. 7, pp. 1355-1362, 2013.

[82] M. Kupnik, M. -C. Ho, S. Vaithilingam, and B. T. Khuri-Yakub, “CMUTs for air coupled ultrasound with improved bandwidth,” in *2011 IEEE International Ultrasonics Symposium*, pp. 592-595, 2011.

[83] A. Unlugedik, A. Atalar, and H. Koymen, “Designing an efficient wide bandwidth single cell CMUT for airborne applications using nonlinear effects,” in *2013 IEEE International Ultrasonics Symposium*, pp. 1416-1419, 2013.

[84] K. K. Park, H. J. Lee, P. Crisman, M. Kupnik, O. Oralkan, and B. T. Khuri-Yakub, “Optimum design of circular CMUT membranes for high quality factor in air,” in *2008 IEEE International Ultrasonics Symposium*, pp. 504-507, 2008.

[85] A. Nikoozadeh and B. T. Khuri-Yakub, “CMUT with substrate-embedded springs for non-flexural plate movement,” in *2010 IEEE International Ultrasonics Symposium*, pp.

1510-1513, 2010.

[86] A. Unlugedik, A. Tasdelen, A. Atalar, and H. Koymen, “Designing transmitting CMUT cells for airborne applications,” *IEEE Transactions on Ultrasonics, Ferroelectrics, and Frequency Control*, vol. 61, no. 11, pp. 1899-1910, 2014.

[87] F. Y. Yamaner, S. Olcum, H. K. Oguz, A. Bozkurt, H. Koymen, and A. Atalar, “High-power CMUTs: design and experimental verification,” *IEEE Transactions on Ultrasonics, Ferroelectrics, and Frequency Control*, vol. 59, no. 6, pp. 1276-1284, 2012.

[88] O. Oralkan, B. Bayram, G. G. Yaralioglu, A. S. Ergun, M. Kupnik, D. T. Yeh, I. O. Wygant, and B. T. Khuri-Yakub, “Experimental characterization of collapse-mode CMUT operation,” *IEEE Transactions on Ultrasonics, Ferroelectrics, and Frequency Control*, vol. 53, no. 8, pp. 1513-1523, 2006.

[89] I. O. Wygant, M. Kupnik, and B. T. Khuri-Yakub, “CMUT design equations for optimizing noise figure and source pressure,” in *2009 IEEE International Ultrasonics Symposium*, pp. 1-4, 2009.

[90] B. A. Boukamp, “A nonlinear least squares fit procedure for analysis of immittance data of electrochemical systems,” *Solid State Ionics*, vol. 20, no. 1 , pp. 31-44, 1986.

[91] M. Onoe, “Contour vibrations of isotropic circular plates,” *Journal of the Acoustical Society of America*, 28 (1956) 1158-1162.

[92] M. Abramowitz and I. A. Stegun, *Handbook of mathematical functions: with formulas, graphs, and mathematical tables*: Courier Corporation, 1964.

[93] N. W. McLachlan, *Bessel functions for engineers*: Oxford University Press, 1934.

[94] S. P. Timoshenko and S. Woinowsky-Krieger, *Theory of plates and shells*: McGraw-hill, 1959.

[95] R. R. Craig and A. J. Kurdila, *Fundamentals of structural dynamics*: John Wiley & Sons, 2006.

[96] M. Kupnik, I. O. Wygant, and B. T. Khuri-Yakub, “Finite element analysis of stress stiffening effects in CMUTs,” in *2008 IEEE International Ultrasonics Symposium*, pp. 487-490, 2008.

[97] K. K. Park, H. Lee, M. Kupnik, and B. T. Khuri-Yakub, "Fabrication of capacitive micromachined ultrasonic transducers via local oxidation and direct wafer bonding," *Journal of Microelectromechanical Systems,* vol. 20, no. 1, pp. 95-103, 2011.

[98] K. S. Pister, “Flexural vibration of thin laminated plates,” *Journal of the Acoustical Society of America*, vol. 31, no. 2, pp. 233-234, 1959.

[99] N. Klein and H. Gafni, “The maximum dielectric strength of thin silicon oxide films,” *IEEE Transactions on Ultrasonics, Ferroelectrics, and Frequency Control*, vol. 13, no. 2, pp. 281-289, 1966.

[100] G. S. Hwang and K. P. Giapis, “On the origin of the notching effect during etching in uniform high density plasmas,” *Journal of Vacuum Science & Technology B, Nanotechnology and Microelectronics: Materials, Processing, Measurement, and Phenomena*, vol. 15, no. 1, pp. 70-87, 1998.

[101] P. Zhang, G. Fitzpatrick, T. Harrison, W. A. Moussa, and R. J. Zemp, “Double-SOI wafer-bonded CMUTs with improved electrical safety and minimal roughness of dielectric and electrode surfaces,” *Journal of Microelectromechanical Systems*, vol. 21, no. 3, pp. 668-680, 2012.